A Robust and Tunable Mitotic Oscillator in Artificial Cells

by

Ye Guan

A dissertation submitted in partial fulfilment
of the requirements for the degree of
Doctor of Philosophy
(Chemistry)
In the University of Michigan
2018

Doctoral Committee:

Assistant Professor Qiong Yang, Co-Chair
Professor Robert Kennedy, Co-Chair
Assistant Professor Allen Liu
Professor Nils Walter
Professor Ji Zhu

Ye Guan

yeguan@umich.edu

ORCID ID: 0000-0002-9427-7603

All Rights Reserved

© Ye Guan 2018

Dedication

To my family
for making me brave and strong

Acknowledgements

There are many great people that have been there along this long journey and I am honored to express my sincere appreciations.

First, I want to thank my dad and mom. I wouldn't be here without my parents' unconditional love and support. They encouraged me to pursue my dream and I know it was a difficult decision for them because of the long distance between us.

I would like to thank my husband, Haotian. I am so grateful that he is here with me all the way along. He moved from Philadelphia to Detroit and started his Ph.D. career here because of me. His support and encouragement walk me through all those difficult and frustrating times. I will remember those sleepless nights and busy weekends working together with him. Thank you for being there no matter what decisions I have made. I can never accomplish my Ph.D. degree without his support. I also want to thank my parents-in-law. Their selfless love and trust make me warm and brave.

I would like to express my sincere gratitude to my advisor, Dr. Qiong Yang, for taking me as her first Ph.D. student and persistent help throughout my graduate study. This dissertation cannot be completed without her tremendous support. I really appreciate that she gives me an opportunity to see a world of science that I was never exposed to before.

I want to thank my other thesis committee members, Dr. Robert Kennedy, Dr. Allen Liu, Dr. Nils Walter, and Dr. Ji Zhu for their time and efforts on this dissertation. Their scientific

insights and helpful suggestions are valuable for my research study. I would especially like to thank Allen for providing technical support on establishing my *in vitro* cell-free system.

I also appreciate the financial support from the National Science Foundation (Early CAREER Grant #1553031), the National Institutes of Health (MIRA #GM119688), and a Sloan Research Fellowship.

I've had the great fortune to know my friends Dr. Xiaoyang Wan and Dr. Meng Zhang during my graduate study. Xiaoyang helps me a lot, and shared his knowledge of molecular biology with me. Meng is also helpful and taught me how to express and purify proteins. Their support and encouragements are very important for my graduate life.

Finally, I am thankful to work with all Yang Lab members and collaborators, especially Zhengda Li, Xuwen Liu, Patrick Barnes, Shiyuan Wang, Minjun Jin, Lap Man Lee, Kenneth Ho and Jeremy Chang. The time going through this process and solving problems together is memorable to me.

Table of Contents

List of Figures

List of Tables

Abstract

This dissertation aims to develop a droplet-based artificial cell system using cell-free extracts of *Xenopus laevis* eggs and understand mitotic oscillations with the proposed system. Single-cell analysis is pivotal to deciphering complex phenomena such as cellular heterogeneity, bistable switches, and oscillations, where a population ensemble cannot represent the individual behaviors. Despite having unique advantages of manipulation and characterization of biochemical networks, bulk cell-free systems lack the essential single-cell information to understand out-of-steady-state dynamics including cell cycles.

In this dissertation, we present a novel artificial single-cell system for the study of mitotic dynamics by encapsulating *Xenopus* egg extracts in water-in-oil micro-emulsions. The artificial cells are different from real cells, *i.e.*, their surface is formed by surfactant oil instead of the cell membrane. These "cells", adjustable in sizes and periods, encapsulate cycling cytoplasmic extracts that can sustain mitotic oscillations for over 30 cycles. The artificial cells function in forms from the simplest cytoplasmic-only oscillators to the more complicated ones involving demembranated sperm chromatin that can reconstitute downstream mitotic events. The dynamic activities of cell cycle clock can be detected by fluorescent reporters such as cyclin B1-YFP and securin-mCherry. This innate flexibility makes it key to studying cell cycle clock tunability and stochasticity. Our experimental results indicate that the mitotic oscillators generated by our system are effectively tunable in frequency with cyclin B1 mRNAs and the dynamic behavior of single droplet oscillators is size-dependent.

We also establish a stochastic model that highlights energy supply as an essential regulator of cell cycles. Moreover, the model explains experimental observations including the increase of baseline and amplitude of cyclin B1 time course. This dissertation study demonstrates a simple, powerful, and likely generalizable strategy of integrating single-cell approaches into conventional *in vitro* systems to study complex clock functions.

CHAPTER I Introduction

The design and construction of synthetic circuits to perform robust self-sustained oscillations in both live cells[1-7] and cell-free systems[8-11] has led to much excitement, but remains challenging. Compared to *in vivo* systems, circuits reconstituted *in vitro* contain a minimal set of well-defined recombinant molecules whose stoichiometry and interactions are manipulatable, and are thus more amenable to systematic design, quantitative analysis, and model predictions. These advantages have enabled fundamental understanding of not only *de novo* designed oscillators based on genetic networks[10] and organic chemical reactions[11], but also natural oscillators such as circadian clocks[8,12] and cell cycles, which are otherwise difficult to dissect in intact organisms. There is great interest in engineering genetic circuits to simulate diverse synthetic oscillators, such as circadian clocks and cell cycle clocks. This dissertation presents a novel platform to reproduce *in vitro* mitotic oscillators that is applicable to the study of cell cycle clock.

1.1 Synthetic oscillator

Synthetic oscillators provide important insight into design principles for biological oscillators. One defining goal of synthetic biology has been to construct gene-regulatory networks based on the "design criterion" proposed by computational modeling[3,13-17] to develop a deep understanding of biological design principles underlying the regulatory mechanism. In living cells, the interactions between biomolecules can form biochemical circuits and carry out various

essential functions including amplification, integration and information storage[18]. To investigate the regulation mechanisms of these biochemical circuits, Elowitz and Leibler[1] built a periodic oscillating network in *Escherichia coli* by proper design and construction of a synthetic network using existing biological components. The engineered oscillator opened a new path to the engineering of cellular behaviors and a better understanding of intracellular networks. More recently, Stricker et al. proposed another synthetic oscillator in *Escherichia coli*, which is fast, robust and tunable with oscillation periods[19]. The oscillator has been used to study how the robustness of these clocks is varied by the interaction noise between biological components and the stochasticity of their gene expression.

The synthetic network is a powerful tool to study the biological pathways and has potential applications in genomics, gene and cell therapy, and nanotechnology[14]. However, one weakness of these synthetic networks is that they reside in living cells and the dynamic behaviors of the synthetic oscillators cannot be well characterized due to the complex environment of growing and dividing cells. To overcome this obstacle, cell-free systems have been used to construct synthetic oscillators[20,21].

In this dissertation, we focus on mitotic oscillators, one of the most widely studied synthetic oscillators. It is important to understand the functions of mitotic oscillators. During the past few decades, people have made great efforts to finding therapeutic methods to inhibit cell cycle clocks and limit the growth of tumor cells[22,23]. These therapeutic methods include inhibiting mitosis by targeting microtubules and mitotic kinases, and inhibiting Cdk1 to impair the entry into cell cycle[23-26]. To investigate better therapeutic strategies to control tumor cell growth, it is crucial to understand the design principles and tunability of cell cycle clocks.

1.2 Molecular networks that drive the early embryonic cell cycles

The cell cycle clock is driven by an autonomous biochemical oscillator and the core of the oscillator is a negative feedback loop that includes the cyclin B-cyclin dependent kinase 1 (Cdk1) and anaphase-promoting complex (APC/C) (Figure 1.1). Here, cyclin B is a mitotic cyclin[27], Cdk1 is a protein functioning as a serine/threonine kinase, and APC/C is an E3 ubiquitin ligase targeting cell cycle proteins for degradation[28]. Cyclin B proteins bind to Cdk1, forming cyclin B-Cdk1 complex. This Cdk1 system has interlinked double-positive and double-negative feedback loops, involving the protein kinases Wee1 and Myt1, and the phosphatases Cdc25. Hereby, both Wee1 and Myt1 are protein kinases that inhibit Cdk1 by phosphorylating it on two sites, Tyr15 and Thr14[29]. Cdc25 refers to cell division cycle 25, a phosphatase that activates Cdk1 by dephosphorylating inhibitory residues on Cdk1[30]. Cyclin B-Cdk1 activates its activating phosphatase Cdk25 and forms a double-positive feedback loop. Meanwhile, activated cyclin B-Cdk1 inhibits inhibitory kinases Wee1 and Myt1, forming a double-negative feedback loop. The double-negative feedback loop functions equivalently to a double-positive feedback loop[31]. The double-positive and double-negative feedback loops collectively function as a bistable trigger[32,33]. Compromising this bistable trigger suppresses cell cycle oscillations, indicating that positive feedback can accelerate cell cycle clock[34]. The E3 ubiquitin ligase APC/C is also activated by active cyclin B-Cdk1 complex, but the mechanism is still not well understood[35]. Active APC/C polyubiquitylates the mitotic cyclin, tagging them for degradation by the proteasome. Therefore, cyclin B-Cdk1 complex is inactivated by active APC/C, forming a negative feedback loop. In summary, activation of Cdk1 drives the cell cycle into mitosis, while the activation of APC/C drives the cell back out of mitosis[36].

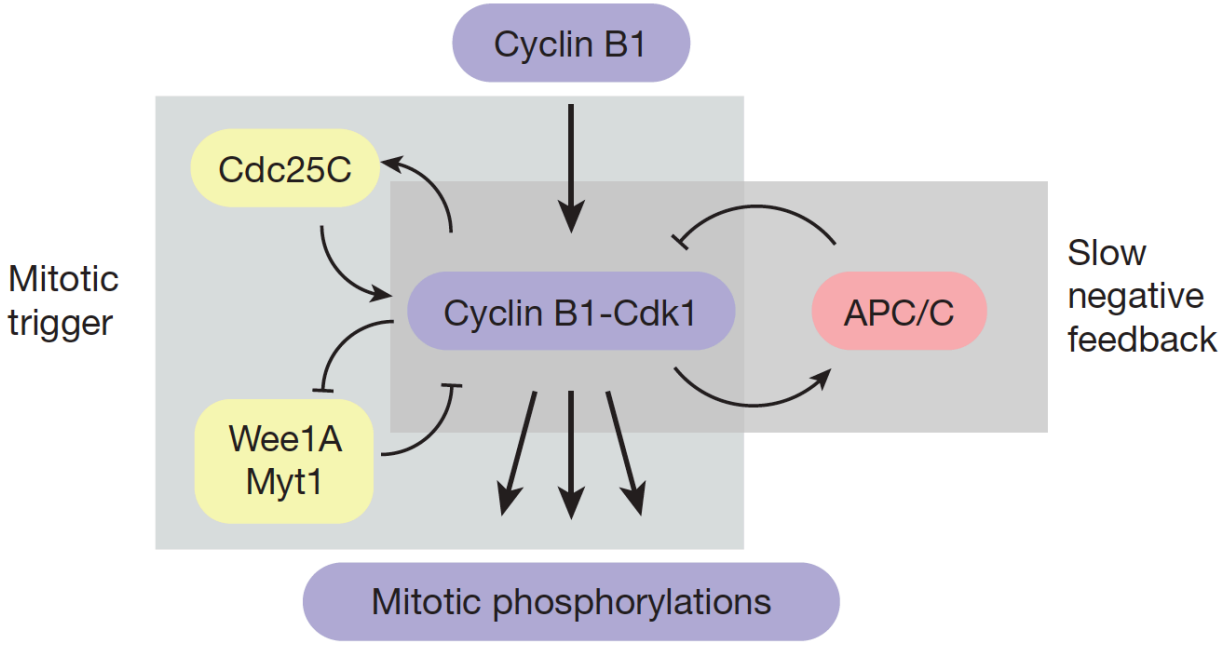

Figure 1.1 Schematic view of the cell cycle circuit centered on cyclin B1-Cdk1 complex[37]. Cyclin B-Cdk1 complex activates its own activator, phosphatase Cdc25, forming a positive feedback loop, and inhibits its own inhibitor, kinase Wee1, forming a double-negative feedback loop. Additionally, cyclin B-Cdk1 activates the E3 ubiquitin ligase APC/C, which targets securin and cyclin B for degradation and completes a core negative feedback loop.

Cytoplasmic extracts predominantly from *Xenopus* eggs[38] have made major contributions to the initial discovery and characterization of the central cell-cycle regulators including the protein complex cyclin B1-Cdk1[39-41] and the anaphase-promoting complex or cyclosome (APC/C) [42], as well as downstream mitotic events of spindle assembly and chromosome segregation [43]. Moreover, detailed dissections of the regulatory circuits in these extracts revealed the architecture of interlinked positive and negative feedbacks[33,34,37,44-50]. Such interlinked feedback loops are also found in many other biological oscillators[12,51-53], suggesting its importance to essential clock functions such as robustness and tunability[31]. Yang et al. pointed out that the negative feedback loop forming by cyclin B-Cdk1 and APC/C functions as a time-delayed and ultrasensitive switch in the *Xenopus laevis* embryonic mitotic oscillator[46]. Computational modeling demonstrates how

such a time-delayed, digital switch generates robust and periodic cell cycle oscillations. These studies stimulated major interests in characterization of clock functions at the single cell level, for which an experimental platform is still lacking. We will discuss cell-free systems that have great potentials for the study of cell cycle clock functions in the following section.

1.3 Cell-free systems

A cell-free system is an *in vitro* tool used to study biochemical reactions that happen within cells while it minimizes the complex interactions in a whole cell[54]. Cellular components can be isolated by ultracentrifugation to study the molecular machinery in a simplified reaction environment[55]. Previous studies have used eukaryotic and prokaryotic cells to create cell-free systems[56]. Prokaryotic cell-free systems such as *E. coli* extracts[57-61] and archaeal cell extracts[62-64] are widely used for large-scale synthesis, industrial production of antibody-drug conjugates, and incorporation of non-canonical amino acids[59-61]. The prokaryotic cell extracts are cost-efficient and have high protein yield. However, these extracts have limited post-translational modifications and no endogenous membrane structures for membrane protein synthesis[56]. There are various well-developed eukaryotic cell-free systems like protozoan extract[65-68], yeast extract[54,69-73], wheat germ extract[59,74-76], insect cell extract[77-79], *Xenopus laevis* extract[37,43,80-82], and mammalian cell extract[83-85]. Eukaryotic cell-free systems have increased in popularity because there is growing interest in human and mammalian proteins and the post-translational modifications[86,87], and they can be applied to study protein-protein interactions[88-90]. Cell cycle dynamic events that happen within cells can be simulated in the extracts of eggs or oocytes *in vitro*. Cell-free systems to study cell cycle clock have been well established in the eggs or oocytes of *Xenopus laevis*[37,91], and

Drosophila melanogaster [92,93]. We will discuss *Drosophila* extract and *Xenopus laevis* extract, which are the two widely used cell-free systems for study of cell cycle clock.

1.3.1 *Drosophila* extract system

Telley et al. developed a protocol for preparing extracts from individual *Drosophila* syncytial embryos that can reconstitute repeated mitotic nuclear divisions[94]. Individual preblastoderm embryos at a well-defined developmental stage were used to generate single *Drosophila* embryo extracts. The generated extracts support repeated nuclear cycling with typical *in vivo* characteristics [93] and currently represent the only experimental *ex vivo* system with this property.

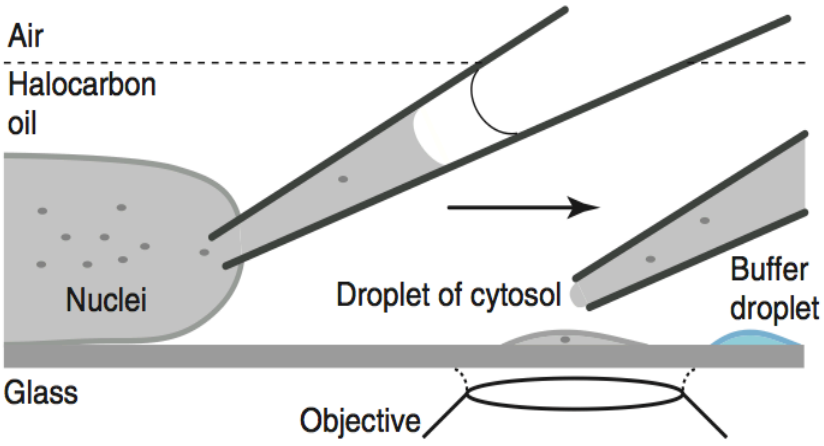

Figure 1.2 Schematic representation of the extraction procedure[94]. A fraction of the cytoplasm and nuclei is sucked into the pipette and ejected as droplets on the glass surface.

This extract overcomes the difficulty of imaging early nuclear divisions, because they can be observed in volumes that are much smaller than the entire embryo. Another advantage is that genetic manipulations are easily performed using well-established methods of *Drosophila*

genetics[95]. This assay enables a unique combination of genetic, biochemical, optical and mechanical manipulations of the mitotic machinery as shown in Figure 1.2. The single *Drosophila* embryo extract has been demonstrated to be a powerful tool for studying the transitions of the cell division machinery in the absence of a cell membrane. *Drosophila* extracts have been applied to the confocal fluorescence microscopy imaging of repeated nuclear divisions and of the distribution of nuclei within the cytoplasmic space, and encapsulation of dividing nuclei in micro-chambers to probe spatial constrains[94].

However, we did not use *Drosophila* extracts for this dissertation study because the egg volume of *Drosophila* is much smaller compared to *Xenopus* eggs. Furthermore, there is no well-developed protocol yet for nuclear-free *Drosophila* cytoplasm, which is not suitable for the study of cell cycle clock dynamics without reconstitution of downstream mitotic events.

1.3.2 *Xenopus laevis* extract system

Another well-established *in vitro* system for the study of cell cycle clock is *Xenopus laevis* extract system. Cytoplasmic extracts prepared from *Xenopus laevis* eggs keep most of the biological properties and represent one of the most predominant models of cell cycle studies[38,43]. Cell components may vary in different batches of *Xenopus laevis* extracts, which may affect cell cycle clocks. To avoid batch variance, we analyzed experimental results from the same batch of extracts. *Xenopus laevis* extract system stands out for the biochemical study of cell cycles given the large volume of oocytes and capability of reconstituting rapid checkpoint-free mitotic events[38,43]. This system allows initial discovery and mechanistic characterization of essential cell-cycle regulators like maturation-promoting factor (MPF) as well as downstream mitotic processes including spindle assembly and chromosome segregation[33,34,38,39,43,47,48,93,94,96,97].

Formation of the mitotic spindle, which serves to segregate sister chromatids during cell division, is a highly complex process and understanding its mechanisms has been a major focus in cell biology for many years. Hannak et al. provided three types of protocols[43] as shown in Figure 1.3 to prepare metaphase-arrested extracts and *in vitro* assays to examine the following pathways of spindle assembly: 1) adding sperm nuclei to meiotic extracts to support half-spindles and bipolar spindle formations; 2) adding sperm nuclei to extracts that proceed through interphase and assemble spindles that undergo anaphase and chromosome segregation; and 3) forming spindle around chromatin-coated beads. The main contribution of their work is to provide assays to use *Xenopous laevis* egg extract system to study mitotic spindle assembly. Although cytoplasmic extract from the eggs of *Xenopus* has become a standard for microscopy-based analysis of spindle assembly and microtubule dynamics[43], repeated cycles of nuclear division and spindle assembly and disassembly reactions have not been reported. We will discuss how to optimize *Xenopus laevis* cycling extract system and make it capable of reconstituting multiple mitotic oscillations for further study of the dynamics of cell cycle clock in Chapter II.

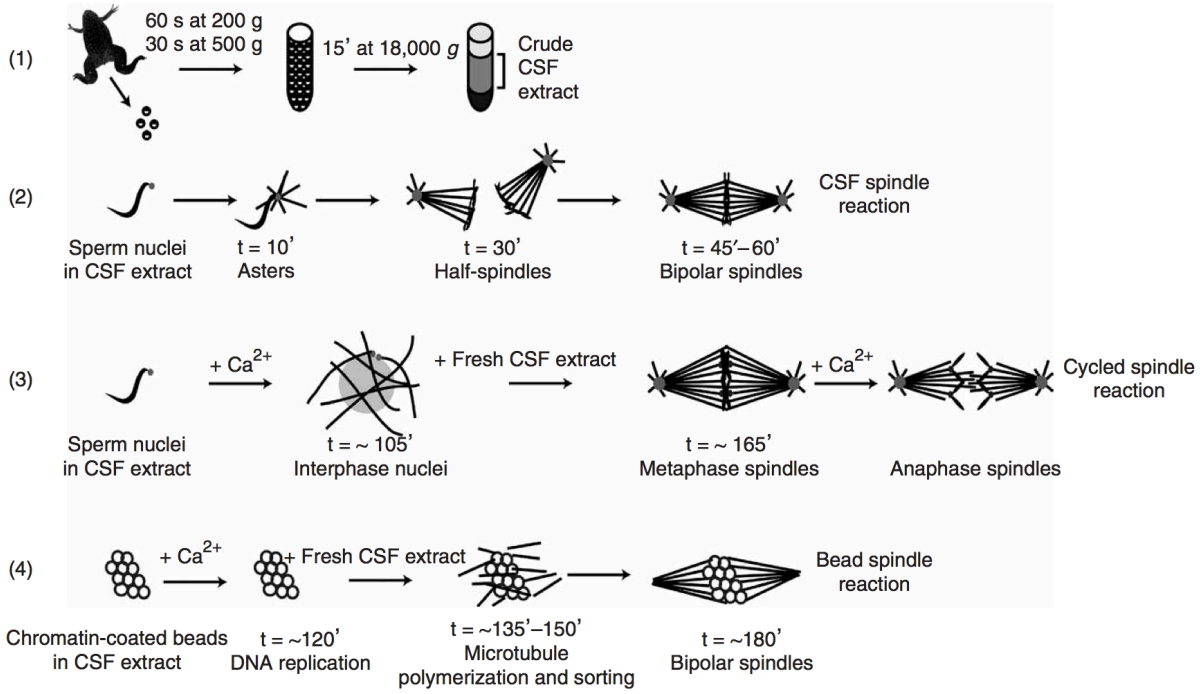

Figure 1.3 Schematic representation of CSF extract preparation and spindle-assembly reactions[43]. (1) Eggs are packed and crushed. (2) CSF reaction. (3) Cycled spindle reaction and anaphase chromosome segregation. (4) Bead spindle reaction.

1.4 *In vitro* compartmentalization of cell cycle oscillators

The *Xenopus laevis* egg extracts have been used for the studies of the regulation of cell cycle clock[34,37,46,91] based on bulk measurements. However, conventional bulk reaction assays have a major disadvantage that real cell dimensions cannot be mimicked. Moreover, bulk measurements of dynamic events are inefficient due to limited number of oscillations. For instance, Pomerening et al. presented up to three *in vitro* oscillations using cycling *Xenopus* extracts in 2005[34] and Chang et al. increased the number of cycles to six by loading bulk cycling extracts into one-dimensional Teflon coated tubes in 2013[37]. The number of detected oscillations is still limited, which may be caused by the averaging effect in bulk reaction environment. Moreover, the dynamic

measurement of single cells is missing because bulk measurement may not reflect the truth of localized oscillations at different sites.

Recently, cell-free micro-reactors to study cell cycles have been built by creating cell-like compartments *in vitro*. Good et al. developed a system to encapsulate cytostatic factor-arrested (CSF)[38,98] *Xenopus laevis* cytoplasmic extracts into a size-defined cell-like compartments and elucidate how spindle size is modulated by the volume of cytoplasmic[99]. *Xenopus* extracts were compartmentalized in cell-like droplets by using microfluidic systems as shown in Figure 1.4A. Their main conclusion is that the length and width of metaphase spindle become smaller when droplet dimension decreases (Figure 1.4B). This high-throughput approach provides a platform to generate cell-like and isolated droplets. However, this *in vitro* system is not proper for the study of cell cycle dynamic events because CSF cytoplasmic *Xenopus laevis* extracts were encapsulated in droplets. CSF extracts are arrested at metaphase of meiosis II by the action of cytostatic factor[38], unless the extracts are supplied with calcium to inactivate CSF. The CSF extracts can be used for spindle assembly and chromosome replication[100] studies but are not proper for dynamic study of long-term oscillations.

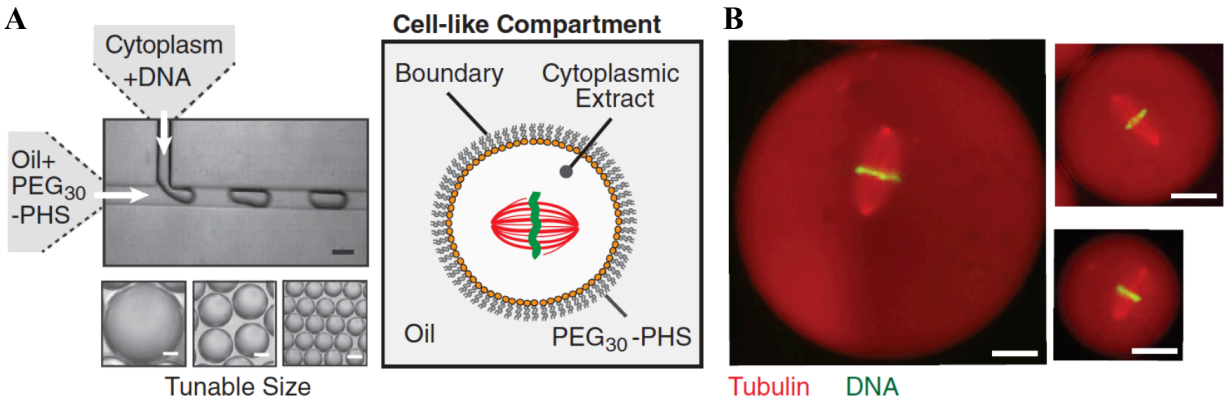

Figure 1.4 *In vitro* compartmentalization of mitotic spindles[81]. A. *In vitro* system to create microdroplets, encapsulated with *Xenopus laevis* egg extracts that are capable of mitotic spindle assembly. B. Mitotic spindles scale with droplet dimensions. The scale bars are 20 µm.

To study cell cycle clocks, it is necessary to develop a cell-like and high-throughput tool that simultaneously allows visualization and detection of individual artificial cell behaviors. Such tools can facilitate deep understanding of complex developmental processes[101]. This dissertation study focuses on the development of high-throughput *in vitro* system to generate cell cycle oscillators and demonstrating its application to the study of cell cycle clock. We will discuss the development of artificial cell system including how to establish an artificial cell system and design fluorescent reporters to detect the activity of cell cycle clock in Chapter II. We will demonstrate that our system is tunable and can be applied to the tunability study of cell cycle clock by quantitative data analysis in Chapter III. In Chapter IV, a stochastic model will be established to analyze the energy dependence of dynamic behaviors of artificial cells. Chapter II, Chapter III and Chapter IV have been submitted for peer review.

CHAPTER II Development of Artificial Cell System to Reconstitute Mitotic Events

2.1 Introduction

Both *in vivo* and *in vitro* methods including experimental animals, dissected tissue and cell cultures have been used to study human diseases and complex system biological questions[102]. *In vitro* and *in vivo* experiments have their own advantages and disadvantages. Specifically, *in vivo* testing is more reliable and precise than *in vitro* testing[103], but it has drawbacks such as it is expensive and time-consuming. Furthermore, existing *in vivo* models are often difficult to probe complex developmental processes[104-106]. Meanwhile, *in vitro* experiments have fewer restrictions than *in vivo* experiments because *in vivo* deals with live animals or tissues while *in vitro* does not. Moreover*, in vitro* systems reduce the complexity of the reaction environment and it is easy to perform biochemical manipulations. Even though it is extremely difficult for *in vitro* systems to reproduce dynamic behaviors of living cells *in vitro*, it is more time-efficient once assays are well developed.

In 1989, Murray and Kirschner proposed an *in vitro* system to study cell cycle clock, of which the extracts can perform two cell cycles[107]. The cytoplasmic extracts prepared from activated *Xenopus laevis* eggs are called cycling extracts, which have been proven powerful to study cell cycle regulations[38]. Cycling extracts have also been widely applied to mimic and investigate diverse cell cycle events such as chromosome morphology changes, nuclear envelope

breakdown and reformation[107,108], DNA replication[109,110], spindle assembly and microtubule dynamics[111,112], and the budding and fusion of carrier vesicles involved in membrane transport[80,113]. However, for most *in vitro* reconstitutions using *Xenopus* cycling extracts, oscillations are generated in well-mixed bulk solutions and exhibit only three to six cycles before damping out[34,114], making it difficult to study cell cycle dynamics. Additionally, these bulk reactions lack the similarity to the actual cell dimensions and the ability to mimic the spatial organization achieved by functional compartmentalization in real cells.

Therefore, an *in vitro* compartmentalized and well-controlled biochemical reaction system is significant to study dynamics of molecular systems and biochemical oscillators[115-120]. To study cell cycle dynamics with real cell dimensions, we developed an artificial mitotic oscillation system by encapsulating reaction mixtures containing freshly prepared cycling *Xenopus* egg cytoplasm[38] in cell-like micro-emulsions of varying sizes, with radii ranging from 20 μm to 500 μm. The droplets were loaded on a Teflon-coated chamber and recorded using long-term time-lapse fluorescence microscopy. These droplet-based cells have undamped self-sustained oscillations for days, offering significant gains in the high-throughput and long-term tracking of dynamic activities, which outperform the current existing *in vivo* and *in vitro* systems.

Fluorescent reporters have become a precise and noninvasive method for real-time tracking of oscillator activities in living cells[121,122] and *in vitro* systems[97,99]. To track mitotic oscillations, we developed multiple reporters to label different cell components and encapsulated reporters into droplets to detect the activities of cell cycles. The developed fluorescent reporters indicate the interphase and mitosis cell-cycle phases in the proposed artificial cell system. The time courses of fluorescence intensity of each droplet were analyzed to obtain information of period, amplitude, number of cycles and droplet size, etc. The continuous output of fluorescence signal from reporters

allowed us to measure the cell cycle dynamic events and explore the relationship between the cell divisions quantitatively.

2.2 Materials and methods

2.2.1 Artificial cell system development

2.2.1.1 Cycling *Xenopus* extracts preparation

We optimized Murray's protocol[38] for the cycling *Xenopus* extract preparation, including 1) egg activation method: eggs were activated with calcium ionophore A23187 (200 ng/μL) rather than electric shock; 2) egg crushing method: we used snap-cap LDPE tubes instead of Eppendorf tubes; 3) extract separation method: instead of isolating cytoplasm by syringes, which may decrease extract activity because of shear force, we cut the tubes to get extracts; 4) buffer removal: to preserve extract activity, we avoided the use of silicone oil Versilube F-50 during the buffer removal step.

Three mature female *Xenopus laevis* were injected with 66 IU pregnant mare serum gonadotropin (PMSG) ten days before laying eggs. These *Xenopus* frogs were injected with 500 IU human chorionic gonadotropin (HCG) to induce egg laying 18 hours before the preparation of cycling extracts. Before the extract preparation, frogs were held with back against hand palm to settle them down. The dorsal side was massaged and gentle pressure was applied to induce egg laying within 5 minutes. Eggs were squeezed into 100 mL petri dishes containing 0.2 X MMR buffer and inspected under an Olympus SZ61 Stereo Microscope. The batches of eggs that had unclear boundaries between animal and vegetal poles, irregular white spots on top of animal poles, or the eggs had strings were discarded. These frogs were not used for egg laying again until three months later.

The batch of eggs presenting a homogeneous population of oocytes with a clearly differentiated animal and vegetal poles was chosen and transferred into a 500 mL beaker. Excess 0.2X MMR buffer was poured out and 250 mL of 2 g / 100 mL cysteine (pH=7.7) in 1X extract buffer was added to eggs gently. The eggs were shaken vigorously by hand and the jelly coats of eggs were removed over three washes with cysteine buffer for three minutes. Eggs were then washed with 1L 0.2X MMR solution over four washes. Meanwhile, eggs that turned white were discarded using a plastic transfer pipette. The MMR buffer was then poured out and eggs were supplied with 200 mL 0.1 µg/mL calcium ionophore A23187 solution in 0.2X MMR buffer for activation. A wide opening side of glass pipette was used to stir the eggs gently for three minutes and calcium ionophore solution was then removed. Activation efficiency was checked after eggs settled down at the bottom of the beaker. For those well-activated eggs, we can observe a contraction of animal pole toward the white spot on the top of eggs, resulting in 25% of the animal pole and 75% of the vegetal pole. Most of the healthy eggs rotated with their animal poles up and vegetal poles down. The overall activation efficiency can be estimated from the percentage of eggs with vegetal side down.

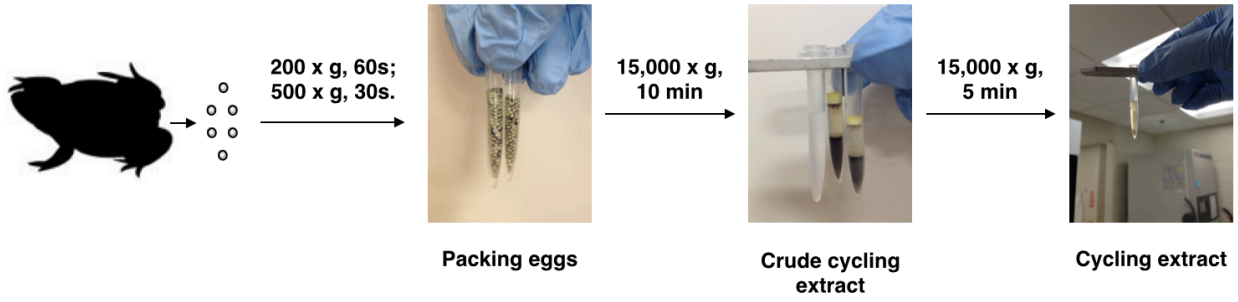

Figure 2.1 *Xenopus* extract preparation. *Xenopus* eggs were freshly collected from a female frog. The collected eggs were packed through low-speed centrifugation and crushed by high-speed centrifugation.

The activated eggs were then washed twice with 50 mL of 1X extract buffer supplemented with protease inhibitors (10μg/mL of leupeptin, pepstatin, and chymostatin). Eggs were carefully transferred to a 0.4 mL snap-cap E&K tube and then packed using Fisher Scientific accuSpin Micro 17R Microcentrifuge, at 200 x g for 60 seconds, and then 600 x g for 30 seconds. To reduce the dilution of extracts, extra buffer on the top of eggs was removed using a glass Pasteur pipette and the tube was tilted to help remove buffer as much as possible. Eggs were crushed at 15,000 x g for ten minutes at 4 °C in Beckman Microfuge E. Tubes were cut to get the cycling extracts in the middle layer. The crude cytoplasm was expelled into new ultracentrifuge tubes, and supplemented with protease inhibitors. It was then spun at 15,000 x g at 4° C for five minutes.

2.2.1.2 Droplet generation and imaging

Freshly prepared extracts were kept on ice while being supplied with demembranated sperm chromatin (250 per μL of extract), 10 μM GFP-NLS, 10 ng/μL securin-mCherry mRNAs, and cyclin B1-YFP mRNAs (ranging from 0 to 10 ng/μL). The extracts were mixed with 2% Perfluoropolyether-poly (ethylene glycol) (PFPE-PEG) surfactant oil to generate droplets.

The microfluidic technique is commonly used for size-controllable formation of droplets[81,123-125]. However, microfluidic devices have a low throughput for the generation of droplets with various sizes, and they are not suitable for real-time imaging of *in vitro* oscillations. Considering these drawbacks, we applied a simple vortexing method[117] to create droplets with a broad cell size distribution to study the effect of molecule partition into various volumes on the dynamic behaviors of cell-like droplet micro-reactors. Specifically, we used Fisher Scientific Vortex Mixer to mix 20 μL cycling extracts supplied with multiple biochemical molecules and 200 μL 2% PFPE-PEG surfactant oil at a speed of level ten for three seconds (Figure 2.2). By

adjusting the vibration speed and ratio between aqueous and oil phase, we can obtain droplets of various sizes, ranging from 20 µm to 500 µm. In summary, our system is a high-throughput system to generate thousands of droplets with various cell sizes within three seconds. It has a great potential to study the effect of compartmentalization into small volumes on cell cycle oscillation behaviors.

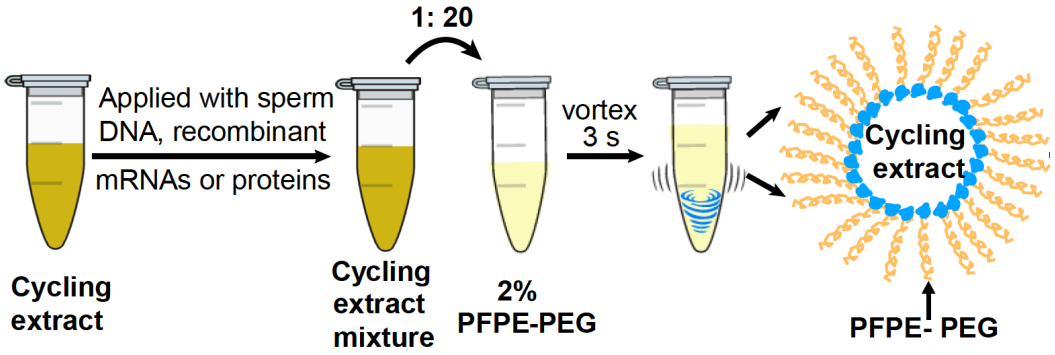

Figure 2.2 Cycling *Xenopus* extracts were supplemented with various combinations of recombinant proteins, mRNAs, and demembranated sperm DNAs, which were encapsulated in 2% PFPE-PEG oil micro-emulsions.

Based on the previous study[37], *in vitro* cell cycle oscillators can reconstitute up to six cell cycles, which are not suitable for the study of cell cycle dynamic process. To preserve the extract activity of artificial cells and detect dynamic events of multiple cell cycles (more than ten cycles), three different sample loading methods were tested. More detailed description of each method is listed as below.

Method 1) 3D glass chamber sealed with epoxy

We loaded micro droplets encapsulated with demembranated sperm DNA, GFP-NLS proteins, and securin-mCherry mRNAs into three-dimensional glass chambers assembled by glass microscope slide, cover slip, and double-sided tapes. Figure 2.3 shows the detailed process of how to assemble the glass chambers. Droplets were flowed into these glass chambers and chambers were then sealed with epoxy to prevent evaporation of surfactant oil and fusion of droplets during the overnight imaging on a fluorescence microscope.

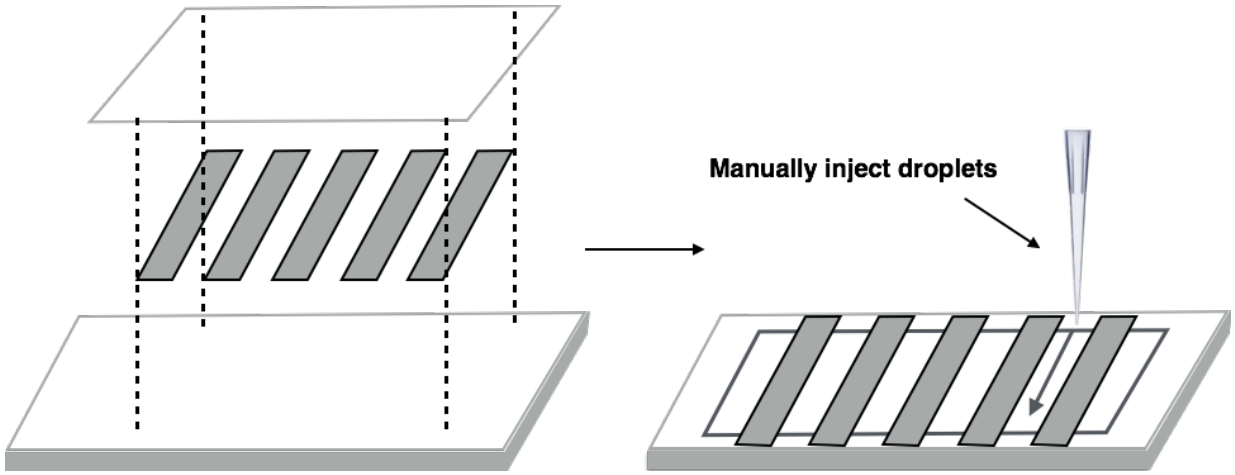

Figure 2.3 Cover slip, double sided tapes and glass microscope slide were assembled to make multiple three-dimensional sample loading chambers.

Method 2) 1D Teflon tubes immersed in mineral oil

Chang and Ferrell[97] proposed to load extracts into one-dimensional Cole-Parmer Teflon tubes which were submerged in mineral oil. Teflon coating provides a hydrophobic environment which stabilizes droplets and the mineral oil allows air permeation. Inspired by their loading method, our artificial cells were loaded into one-dimensional Teflon coated tubes. Teflon tubes

were cut into sections with length of 4 mm and then imaged by a time-lapse epifluorescence microscope.

Method 3) 3D Teflon-coated glass chambers immersed in mineral oil

To develop a high-throughput system and generate artificial cells with real cell dimensions, we optimized our three-dimensional glass chamber loading method by coating with Teflon and immersing into mineral oil instead of sealing with epoxy. VitroCom miniature hollow glass tubes with height of 100 µm were cut into pieces with length of 4 mm. A heating block was heated to 95C° in a Fisher Scientific Isotemp Digital Incubator and then it was placed into a Bel-art F42025-0000 Polycarbonate Vacuum Desiccator with white polypropylene bottom. To stabilize droplets and create a hydrophobic environment, a 1.5 mL Eppendorf tube containing 30 µL Trichloro (1H,1H,2H,2H-perfluorooctyl) silane were placed in the heating block. The cut glass tubes were kept in the vacuum desiccator for overnight incubation.

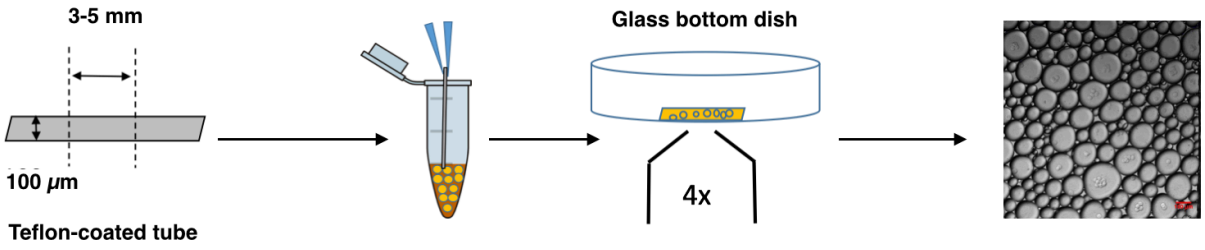

Figure 2.4 Droplets were loaded into a Teflon-coated tube and then imaged on a fluorescence microscope. The scale bar is 100 µm.

Droplets were then loaded into Teflon-coated tubes (Figure 2.4). Imaging of droplets was conducted on an Olympus FV1200 confocal microscope under MATL mode (multiple area time lapse) and an Olympus IX83 microscope equipped with a motorized x-y stage. Time-lapse images

were recorded in the bright field and multiple fluorescence channels every six to nine minutes for up to four days.

2.2.2 Development of reporters for cell cycle clock detection

We developed multiple fluorescent reporters for the detection of cell cycle dynamics and subsequent quantitative analysis. The constructed cyclin B1-YFP and securin-mCherry reporters provide direct measurement of cyclin B1 and APC/C activities, respectively. Demembranated *Xenopus Laevis* sperm chromatin[43,97,99,126,127] and purified green fluorescent protein (GFP)-nuclear localization signal (NLS) protein are added to the extracts as reporters of nuclear morphology[97]. With Hoechst dye, chromosome condensation and separation process can be tracked and studied[128-132].

2.2.2.1 Securin-mCherry and cyclin B1-YFP mRNAs

Securin, which is a substrate protein of anaphase-promoting complex (APC/C) can be used to monitor APC/C activities in real time[96,133-135]. To capture the activity of APC/C, we designed a fluorescent plasmid securin-mCherry and then transcribed securin-mCherry DNA into mRNA which was added to our cell-free system. The new plasmid was constructed using Gibson Assembly method[136-139], which is an isothermal reaction to assemble DNA molecules with overlapping regions through a 5' exonuclease, a DNA polymerase, and a DNA ligase. More specifically, three fragments including a backbone, securin, and mCherry were prepared through polymerase chain reaction (PCR) and gel purification[140,141]. The concentrations of fragments were measured through Nano Drop. 100 ng of backbones with securin and mCherry inserts were

combined at an equal molecular ratio, and deionized water was added to adjust the total volume of reaction to 5 µL.

6 mL of 5X isothermal assembly reaction buffer was prepared with 3 mL 1M Tris-HCl (pH=7.5), 300 µL 1M $MgCl_2$, 600 µL 10 mM dNTP, 300 µL 1M DTT, 1.5 g PEG-8000, and 20 mg NAD[136]. The combined fragments were added to 15 µL 1X isothermal assembly reaction aliquot. The PCR reaction tube was incubated at 50 °C for 15 minutes. Agarose gel electrophoresis was performed to verify the binding efficiency of these fragments. The constructed plasmid was then purified and 1 µL of the Gibson Assembly product was transformed into *E. coli* cells[142]. The constructed securin-mCherry plasmid map is shown in Figure 2.5.

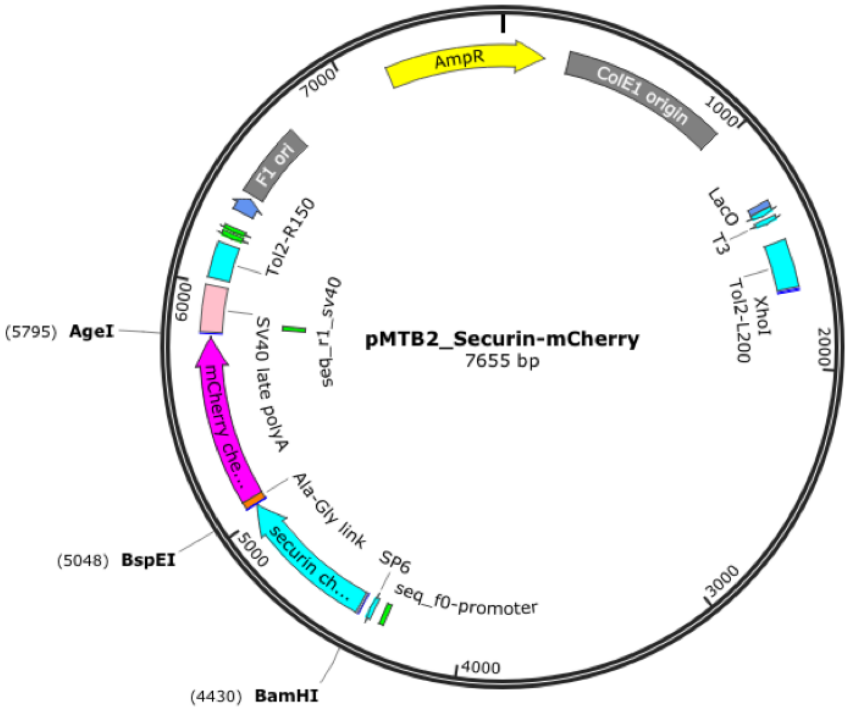

Figure 2.5 The plasmid map of securin-mCherry. The securin-mCherry construct has a pMTB2 backbone that is resistant to ampicillin. There is a BamHI enzyme digestion site before securin, a BspEI site between securin and mCherry sequences, and an AgeI after mCherry sequence.

The fluorescent proteins expressed from cyclin B1-YFP mRNAs can be used to detect the real-time expression and degradation of cyclin B. The cyclin B1-YFP constructs we used were provided by Ferrell's lab. The plasmids of cyclin B1-YFP were purified using the QIAprep Spin Miniprep Kit. The cyclin B1-YFP and securin-mCherry plasmids were then transcribed into mRNAs using mMESSAGE mMACHINE™ SP6 Transcription Kit.

2.2.2.2 Demembranated *Xenopus laevis* sperm DNA

Chromosome DNA is required to reconstitute mitotic events including chromosome condensation and decondensation. To prepare demembranated sperm DNA, *Xenopus laevis* testes were dissected from a male *Xenopus* frog[143,144] and rinsed three times in cold 1X MMR solution (0.5 M NaCl, 0.2 M KCl, 0.1 M $MgCl_2$, 0.2 M $CaCl_2$, 0.1 M Hepes, 0.05 M EDTA). Excess blood and fat were removed from the testes and then washed twice in cold nuclear preparation buffer (2 M sucrose, 1 M pH=7.4 Hepes, 0.5 M pH=8.0 EDTA, 10 mM sperdidine trihydrochloride, 4 mM spermine tetrahydrochloride). Nuclear preparation buffer (NPB) was removed and testes were cut into pieces using sharp dissecting scissors. The testes were then added into 8 mL cold NPB for further breakdown. Nylon mesh fabrics were used to filter the testes. The collected sperms were spun down at 3000 rpm for ten minutes at 4 °C.

The sperm cells were supplied with 1 mL NPB and 50 μL of 10 mg/mL lysolecithin and incubated at room temperature for demembranation. The demembranated sperms were then washed with cold NPB and BSA solution for three times. The density of sperm DNAs was measured with a hemocytometer and the final concentration is 6.18×10^6 cells/mL. The sperm DNAs were then frozen in 5 μL aliquots in liquid nitrogen and stored at -80 °C.

2.2.2.3 GFP-NLS protein

For the extracts at interphase, the sperm chromatin forms nuclei and the nuclear envelope is reformed with nuclear pores[145] that import the GFP-NLS protein, which express bright green fluorescence signal. As the cell cycle progresses and the extract enters mitosis, the nuclear envelopes break down and GFP-NLS quickly disperses[97,146-150]. Subsequently, green fluorescence signal from GFP-NLS protein will disappear. Thus, the GFP-NLS enables the indication of nuclear envelope breakdown and reformation[151].

To obtain GFP-NLS proteins, the GST-tagged GFP-NLS plasmids were transformed into *E. coli* competent cells (BL21, DE3)[97]. The cells were first incubated without antibiotics for one hour and then spread on a LB agarose plate with ampicillin. The plate was incubated at 37 °C for 14 to 18 hours to grow cells in single colonies, which were picked and inoculated into 4 mL LB media with ampicillin. The cells were shaken at 37 °C for 12 hours before inoculation into YT media (16g Bacto-tryptone, 10g Bacto-yeast extract, 5g NaCl) with ampicillin. The YT media was then heated to 37 °C and shaken for 2 hours to increase cell density.

Cell optical density (OD) was measured every 30 minutes and 0.1 mM IPTG was added into cells to induce GFP-NLS protein expression once the OD value reached 0.1. The cells were then shaken at 18 °C overnight with aeration to reduce cell growth rate while allows better protein expression and synthesis. The cells were spun down at 15,000 rpm under 4 °C for five minutes. The cells were then resuspended in 1 mL PBS buffer (supplied with 20 µL 50 ng/mL lysozyme, 2.5 µL 0.2 M PMSF, 0.33 µL 10 mg/mL mixer of protease inhibitors, and 0.2 µL 0.5 M EDTA) and incubated at 4°C for 20 minutes.

To break down cells and release expressed GFP-NLS proteins, we sonicated cells on ice with close monitoring of the temperature of cells. The broken cells were then removed by

centrifugation. To extract and purify GFP-NLS proteins, GE Healthcare Glutathione Sepharose 4B beads were used to combine proteins. The beads were then washed with PBS buffer and incubated for four hours at 4 °C with inversion. The beads were spun down and supplemented with wash solution (25 mM pH=7.5 Tris base, 500 mM NaCl, and 5 mM DTT), and then incubated in elution buffer (50 mM pH=8.8 Tris-HCl, 20 mM reduced glutathione, and 5 mM DTT) with rotation at 4 °C. The concentration of collected proteins was measured by running a Coomassie blue gel. The proteins were then further eluted using PD-10 columns through buffer exchange.

2.2.2.4 H2B-eBFP plasmid

DAPI and Hoechst are two widely used nuclear and chromosome counterstains. DAPI emits blue fluorescence and binds to the adenine-thymine (A-T) regions of chromosome DNA[152,153], forming a stable complex which fluoresces 20 times brighter than DAPI alone without binding to DNA. Similarly, Hoechst is a cell-permeable DNA stain that also emits blue fluorescence. Hoechst binds into the minor groove of DNA and gives distinct fluorescence emission spectra[152,154]. Due to the toxicity of DAPI, it is mainly used for fixed cell samples. To test if DAPI is applicable to our system, extracts in the left tube were supplied with DAPI while the other two tubes were not. We also used Hoechst dye to stain chromosome DNA. However, the number of cycles is still quite limited. The experimental results will be discussed in Section 2.3.

To reduce the toxicity induced by the fluorescent reporters of chromosome morphology, we reconstructed H2B-eBFP plasmid with His-tag for future protein purification purpose. Hereby, H2B histones are basic nuclear proteins that are involved in the nucleosome structures. A forward primer with coding sequence of His-tag was designed and PCR was performed to insert the His-tag sequence into our H2B-eBFP plasmid (Figure 2.6).

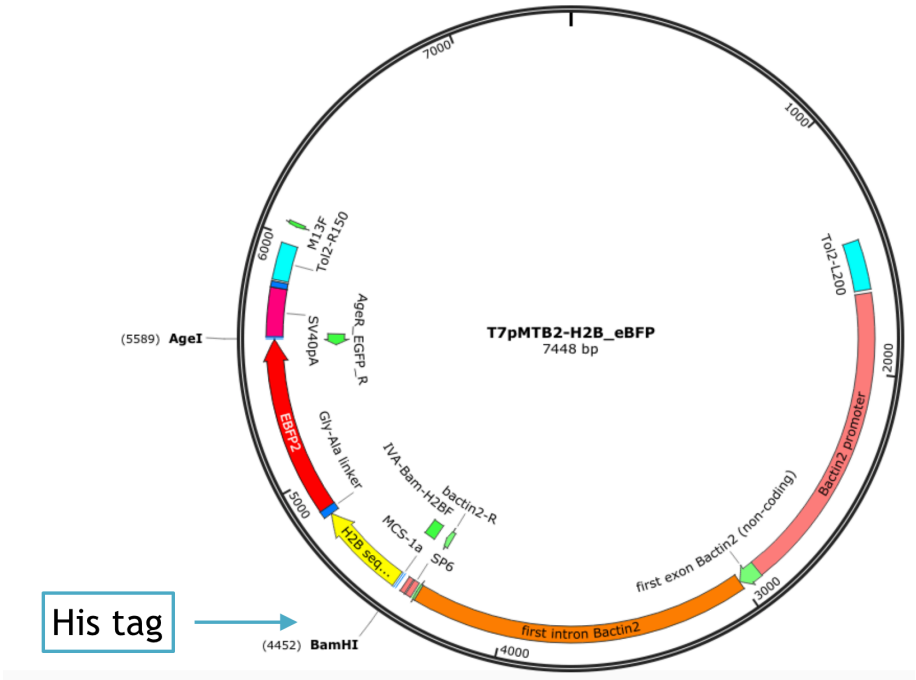

Figure 2.6 Construct of His-tagged H2B-eBFP plasmid.

2.3 Results and discussion

2.3.1 Comparison of three loading methods

The activities of extracts of three loading methods were different. For loading method 1, there was no droplet with ten oscillations or more using the glass chamber loading method. This observation is consistent based on the four replicates on different batches of *Xenopus* extracts. The droplet with most oscillations of method 1 over the four replicates is shown in Figure 2.7 and Figure 2.8. Even though the mitotic events can be successfully reconstituted, only five oscillations were observed in the example droplet. Figure 2.8 indicates that the securin-mCherry mRNA expression was slow and there was only one oscillation from the fluorescence signal. Therefore,

the activities of extracts were not well preserved compared to the oscillation behavior in Chang and Ferrell's work[97], which may due to the hydrophilicity of glass tubes, making droplets unstable, and oxygen depletion caused by epoxy sealing.

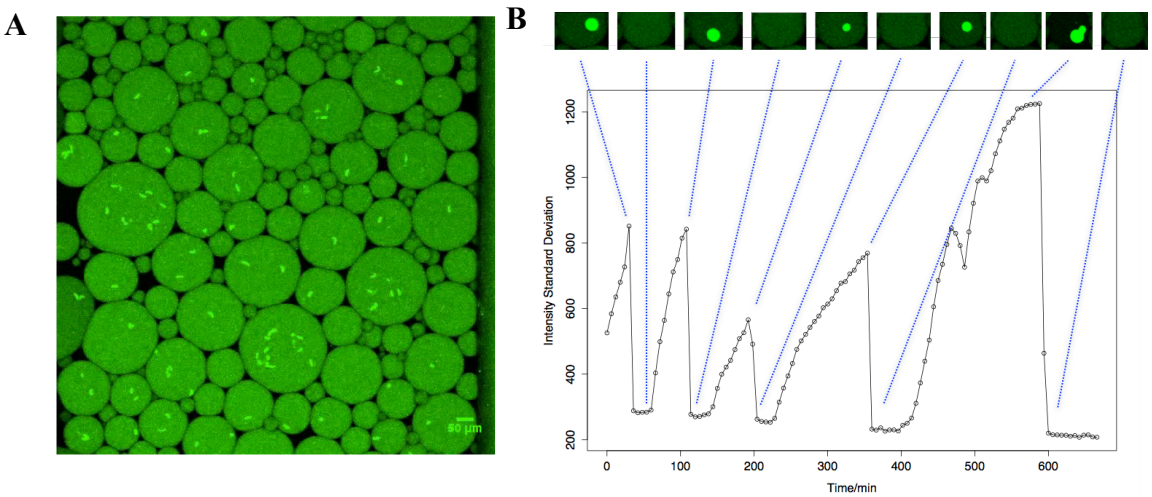

Figure 2.7 Nuclear envelope reformations and breakdowns in droplets. A. Cycling *Xenopus* extracts were supplemented with demembraned sperm DNAs and GFP-NLS proteins, which were encapsulated in 2% PFPE-PEG oil micro-emulsions. The scale bar is 50 µm. B. Cell cycle periods were indicated by the process of nuclear envelope breakdowns and reformations.

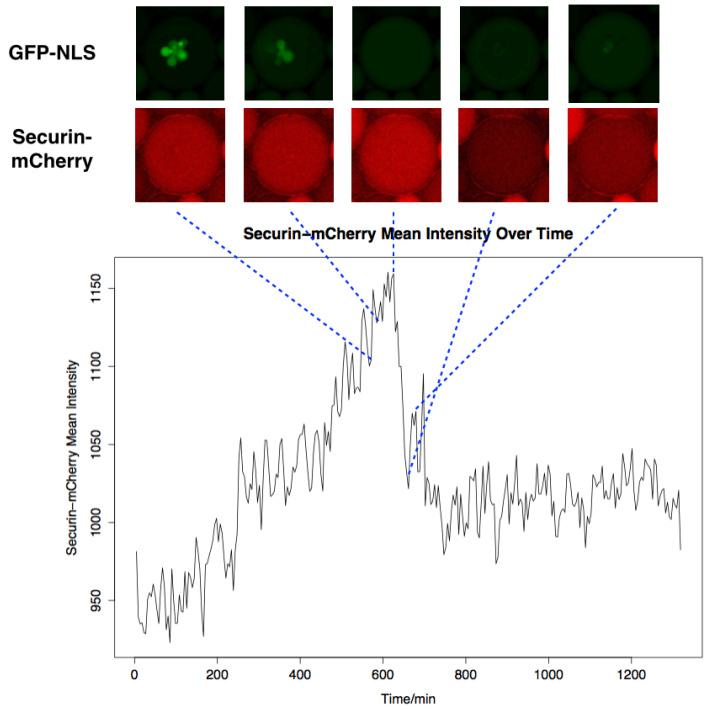

Figure 2.8 Nuclear envelopes were reformed in droplets and only one oscillation was observed from the fluorescence signal of expressed securin-mCherry proteins in the example droplet.

Compared to loading method 1, securin-mCherry mRNAs were successfully expressed into proteins using method 2 (Figure 2.9), while droplets loaded into 3-dimensional glass chambers had much lower level of mRNA expression (Figure 2.8). Figure 2.10 shows that droplets had seven to eleven oscillations as indicated in the securin-mCherry channel. The results shown in Figure 2.9 and 2.10 are reproducible in four replicates. As discussed above, droplets loaded into one-dimensional Teflon tubes (method 2) have more oscillations compared to the ones loaded into three-dimensional glass chambers that are sealed with epoxy (method 1). We can conclude that one-dimensional Teflon tubes can better preserve extract activity.

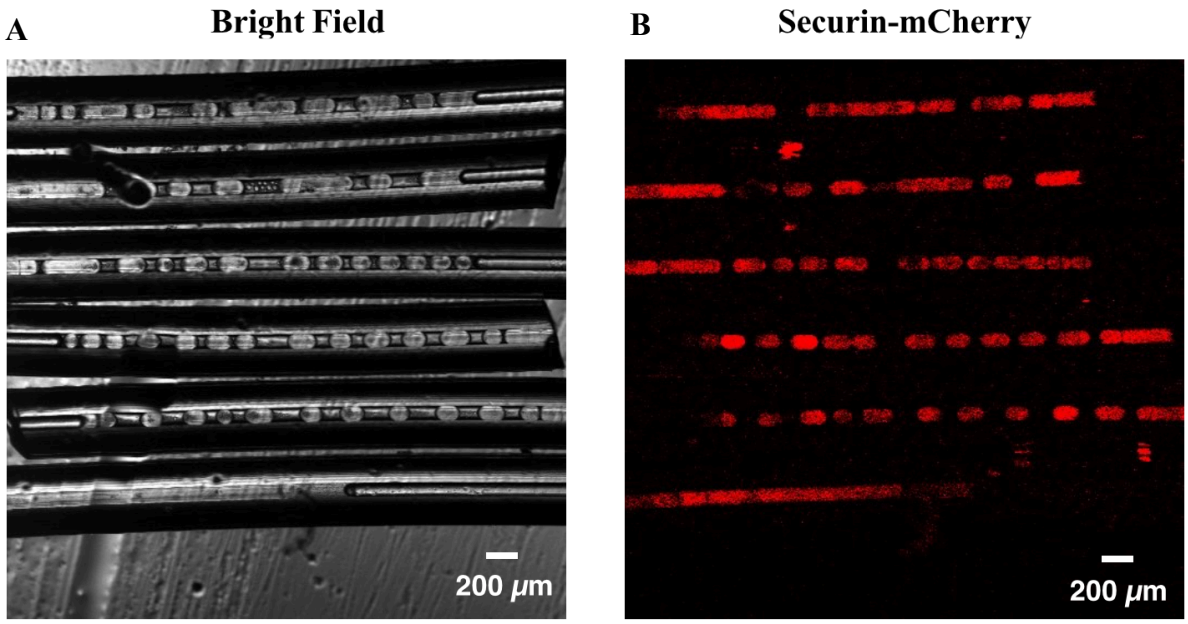

Figure 2.9 Extract activity of droplets loaded in 1D Teflon tubes that were immersed in mineral oil. Cycling *Xenopus* extracts were supplemented with securin-mCherry mRNAs, which were encapsulated in 2% PFPE-PEG oil micro-emulsions. A. Droplet images under the bright field. B. Securin-mCherry fluorescence signal expression in multiple droplets.

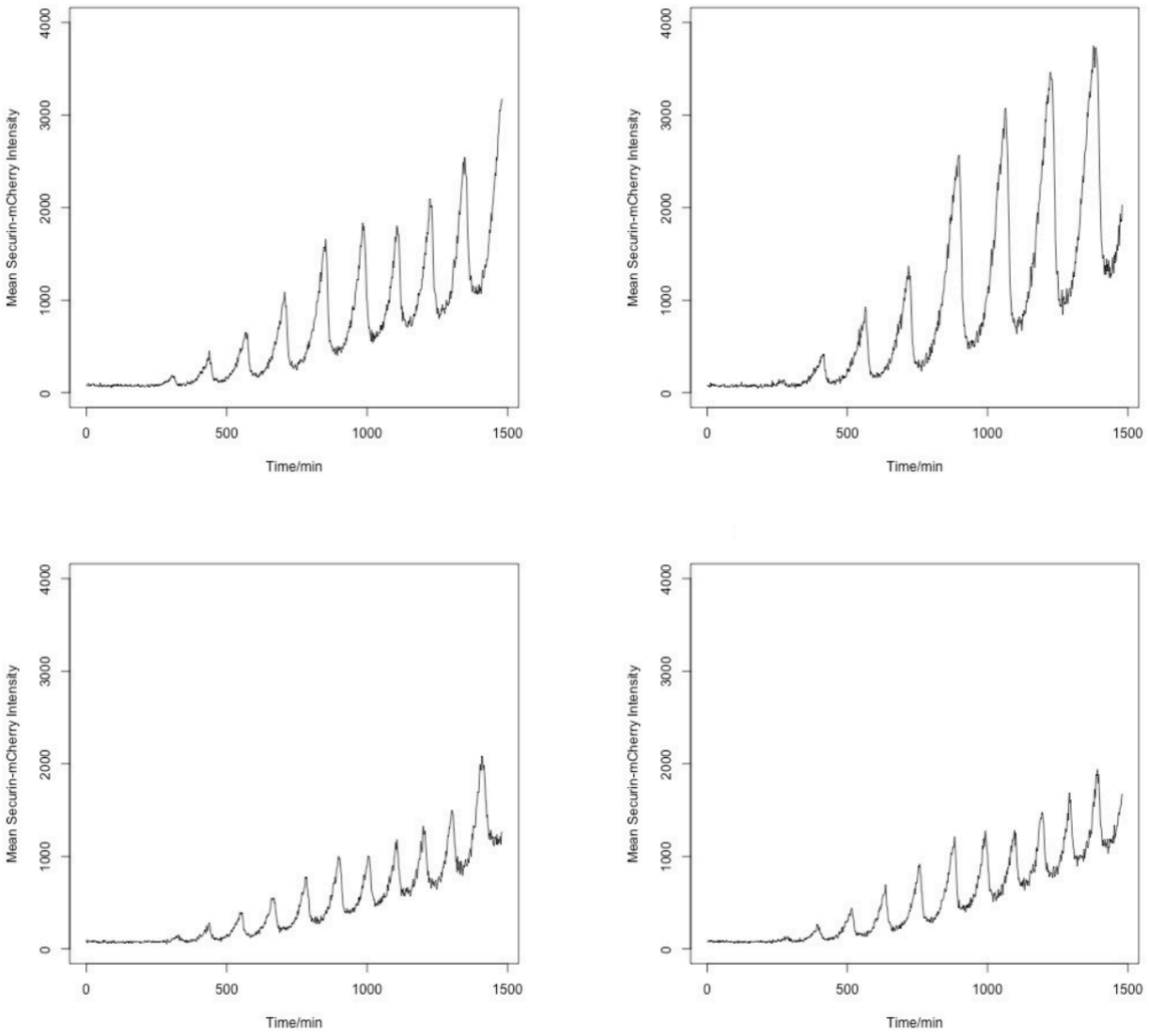

Figure 2.10 The cell cycle oscillations were measured through securin-mCherry channel in four different example droplets. The oscillations had increasing baseline and amplitude.

However, the one-dimensional Teflon coated tubes are not suitable for our system because the optical transparency of Teflon decreases as the film thickness increases, making it more difficult for imaging and image analysis. Moreover, the loading capacity of Teflon tubes is limited, resulting in a low throughput of droplets for further analysis. Although droplets loaded into the

one-dimensional Teflon tubes performed multiple cycles, the droplets were squeezed into elongated shape, which do not represent the real cell dimension and shape. Thus, method 2 is not reliable to mimic the real cell cycle oscillations.

For loading method 3, the droplet with most mitotic oscillations had 32 undamped oscillations over more than 100 hours, as indicated by Figure 2.11. More detailed statistical analysis is shown in Figure 2.12B, indicating that minimal number of cycles is three while the maximum is 32. The number of cycles for droplets within 1st quartile and 3rd quartile ranges from 12 to 20. Generating a population of droplets that have more than ten oscillations is validated in three replicates. The *in vitro* oscillation activity is significantly improved compared to the above two loading methods. The activity of cell cycle oscillators in our system also outperforms the previous studies[34,97]. Therefore, the three-dimensional glass chambers coated with Teflon is a proper loading method that can preserve extract oscillation ability for a long period. We used this method to load droplets for our artificial cell system.

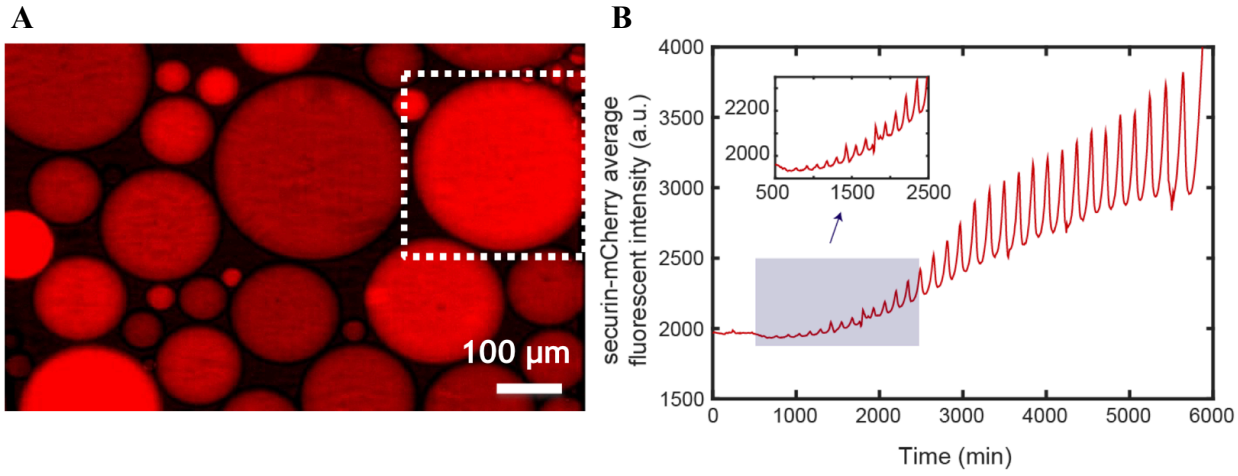

Figure 2.11 The fluorescent image and time course of securin-mCherry. A. The fluorescent image of securin-mCherry in droplets. The scale bar is 100 μm. One example (inside the white dotted framed square) is selected for time course analysis in B. B. The time course of securin-mCherry fluorescence intensity of the selected droplet, indicating 32 undamped oscillations over a course of 100 hours.

2.3.2 Detection of cell cycle events by fluorescent reporters

To test the functionality of securin-mCherry and cyclin B1-YFP mRNAs, we mixed them with cycling *Xenopus* extracts and encapsulated into droplets. As shown in Figure 2.12A, the securin-mCherry and cyclin B1-YFP mRNAs were expressed into functional fluorescent proteins successfully. The number of cycles for droplets with different concentrations of cyclin B1-YFP is shown in Figure 2.12B. For the first group without cyclin B1-YFP, the median oscillation number is 17 and the maximum is 32. The 1st quartile and 3rd quartile of cycle number are 12 and 20, respectively. It indicates that the activities of extracts were well preserved and the number of oscillations was significantly improved compared to previous studies. More details about image processing and statistical analysis will be discussed in Chapter III.

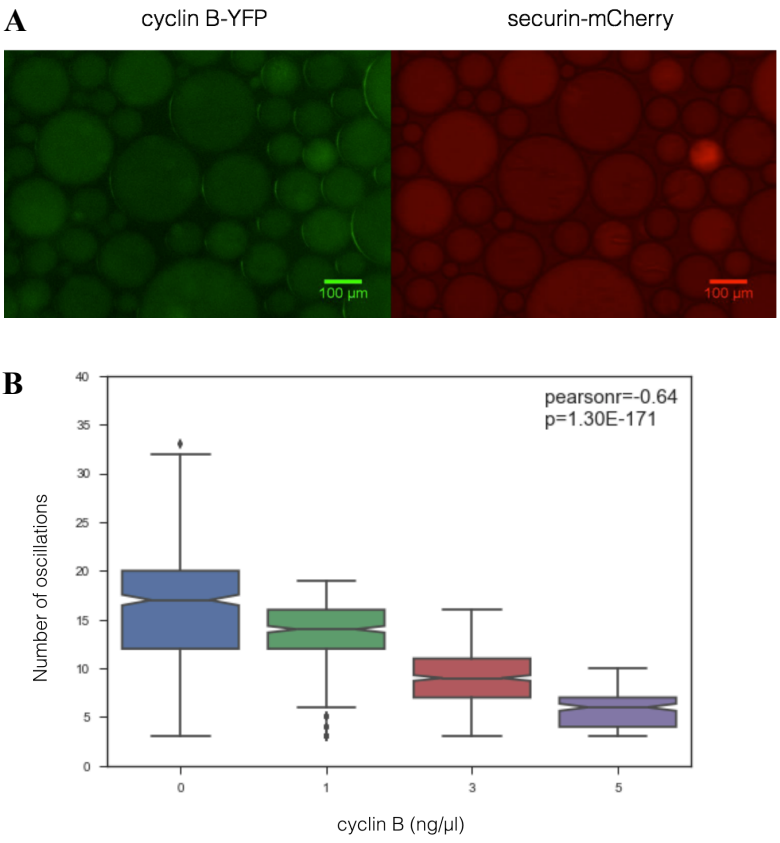

Figure 2.12 A. Fluorescent images of cyclin B1-YFP and securin-mCherry in droplets. B. Number of cycles for droplets with various concentrations of cyclin B1-YFP mRNAs.

The mitotic downstream events including nuclear morphology changes and nuclear envelope breakdowns and reformations were detected by GFP-NLS proteins and Hoechst dye. As shown in the Figure 2.13 A, our expressed and purified GFP-NLS proteins were functional and capable of indicating nuclear envelope formation. Figure 2.13 B shows that demembranated sperm chromatin and Hoechst dye can be used for nuclear envelope reformation and detecting cell cycle clock behaviors.

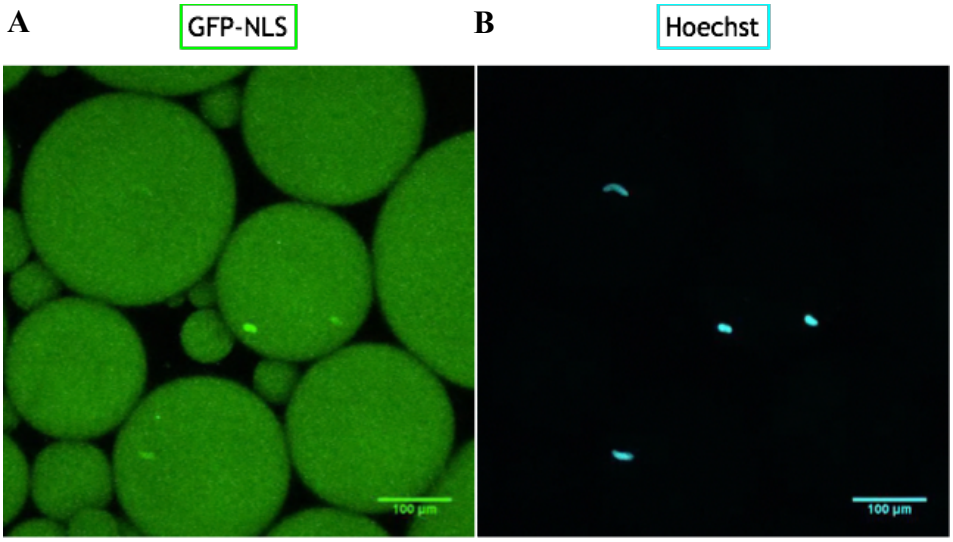

Figure 2.13 Detection of chromosome and nuclear envelope. A. The nuclear envelope breakdowns and reformations were detected by GFP-NLS protein. B. The morphology changes of chromosome were indicated by Hoechst dye.

To test the toxicity of DAPI, the cycling extracts in the left tube were supplied with DAPI while the others were not (Figure 2.14). The extracts in the left tube died out after 180 minutes while the extracts in the other tubes were still oscillating. Complete nuclear envelopes were actively reformed in the middle tube, indicating extracts entered interphase. Meanwhile, the nuclear envelopes broke down and the extracts entered mitosis in the right tube after 180 minutes.

Thus, DAPI cannot be used for tacking dynamic changes of chromosome morphology in our cycling extract system.

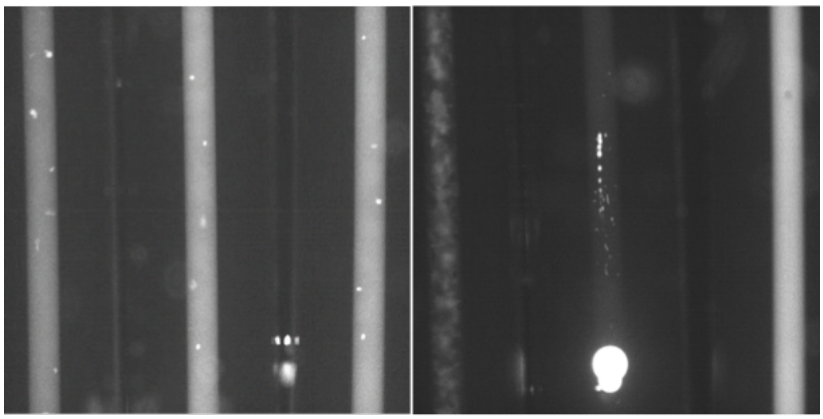

Figure 2.14 Fluorescent images of GFP-NLS channel. Extracts supplied with GFP-NLS protein and demembranated sperm DNA were loaded in one-dimensional Teflon tubes. The extracts in the left tube were supplied with DAPI while the others were not. The shown images were taken at 0 min and 180 min, respectively.

We then designed H2B-eBFP plasmids to detect morphology of DNA with reduced toxicity. Constructed plasmids were successfully obtained under various PCR annealing temperatures. As shown in Figure 2.15, the yield of products was highest under 70 ℃. Our future research plan is to express and purify H2B-eBFP proteins from our designed plasmids. The purified proteins can be applied in our artificial cell system for the detection of nuclear morphology. H2B-eBFP fusion proteins incorporate into nucleosomes and do not affect cell cycle progression. Moreover, its fluorescence color is blue, which is compatible to simultaneous fluorescence imaging for multiple cell cycle events.

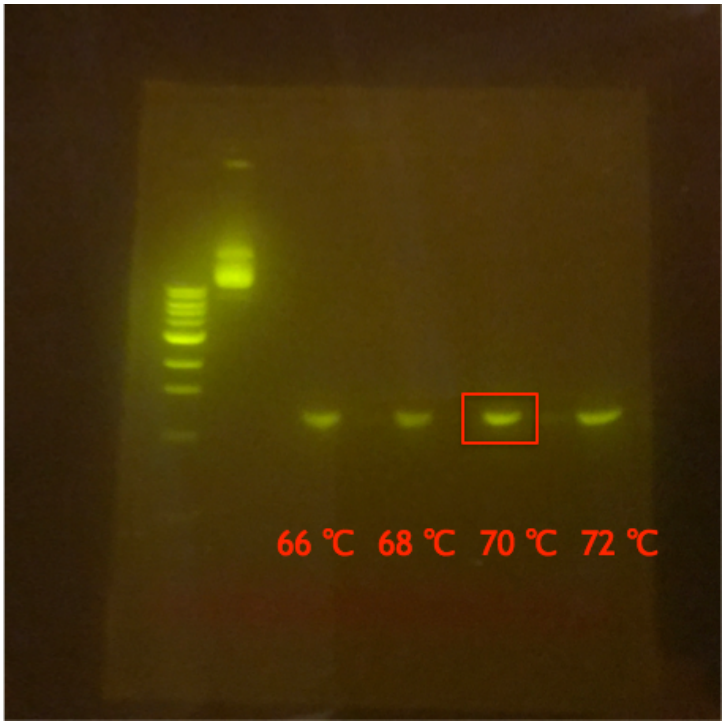

Figure 2.15 The gel image of reconstructed H2B-eBFP plasmids under four different PCR annealing temperatures (66 °C, 68 °C, 70 °C, 72 °C).

2.3.3 Reconstitution of mitotic events

To examine the oscillation ability of our mitotic system, we added demembranated sperm chromatin, purified green fluorescent protein-nuclear localization signal (GFP-NLS), securin-mCherry mRNA and Hoechst 33342 dyes to the cytoplasmic extracts. Our experimental results shown in Figure 2.16 demonstrate an artificial mitotic cell which is capable of reconstructing at least three mitotic processes in parallel that alternate between interphase and mitosis. The results above are reproducible in three replicates. The autonomous alternation of distinct cell-cycle phases is driven by a self-sustained oscillator, the activity of which is indicated by the periodic degradation of an anaphase substrate of APC/C, securin-mCherry. In interphase, the presence of sperm

chromosomal DNA, labeled by Hoechst, initiated the self-assembly of a nucleus, upon which GFP-NLS proteins are imported through the reassembled nuclear pores[155]. The spatial distributions of Hoechst and GFP-NLS thus coincide for an interphase nucleus. As the artificial cell enters mitosis, the chromosome condenses, resulting a tighter distribution of Hoechst, while the nuclear envelope breaks down and GFP-NLS proteins quickly disperse into a uniform distribution in the whole droplet.

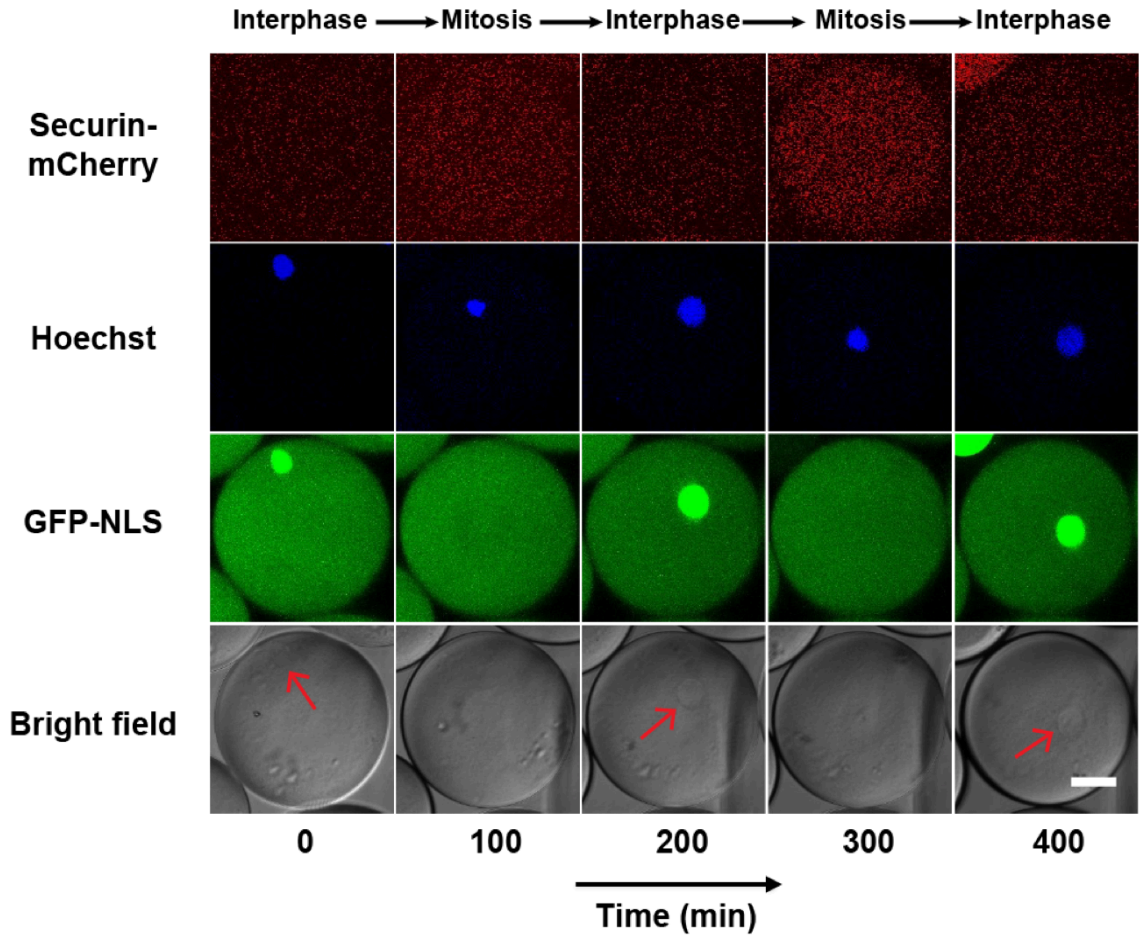

Figure 2.16 The detection of cell cycles using fluorescent reporters. Snapshots of a droplet were taken periodically both in fluorescence channels (top three rows) and the bright field (the last row). The cyclic progression of the cell cycle clock and its downstream mitotic processes are simultaneously tracked by multiple fluorescent reporters. The clock regulator APC/C activity is reported by its substrate securin-mCherry, chromosomal morphology changes by the Hoechst stains, and nuclear envelope breakdowns and reformations by GFP-NLS. Nuclear envelopes (highlighted by red arrows) are also detectable in the bright field images, matching the localization of GFP-NLS indicated nuclei. The scale bar is 30 μm.

The time courses for these mitotic processes were analyzed (Figure 2.17), indicating that the chromosome condensations and nuclear envelop breakdowns happened before the securin degradation in each cycle. These experimental results are validated by three replicates, showing that our droplet system successfully reconstitutes mitotic oscillators that can reliably drive the periodic progression of downstream events as what occurs *in vivo*.

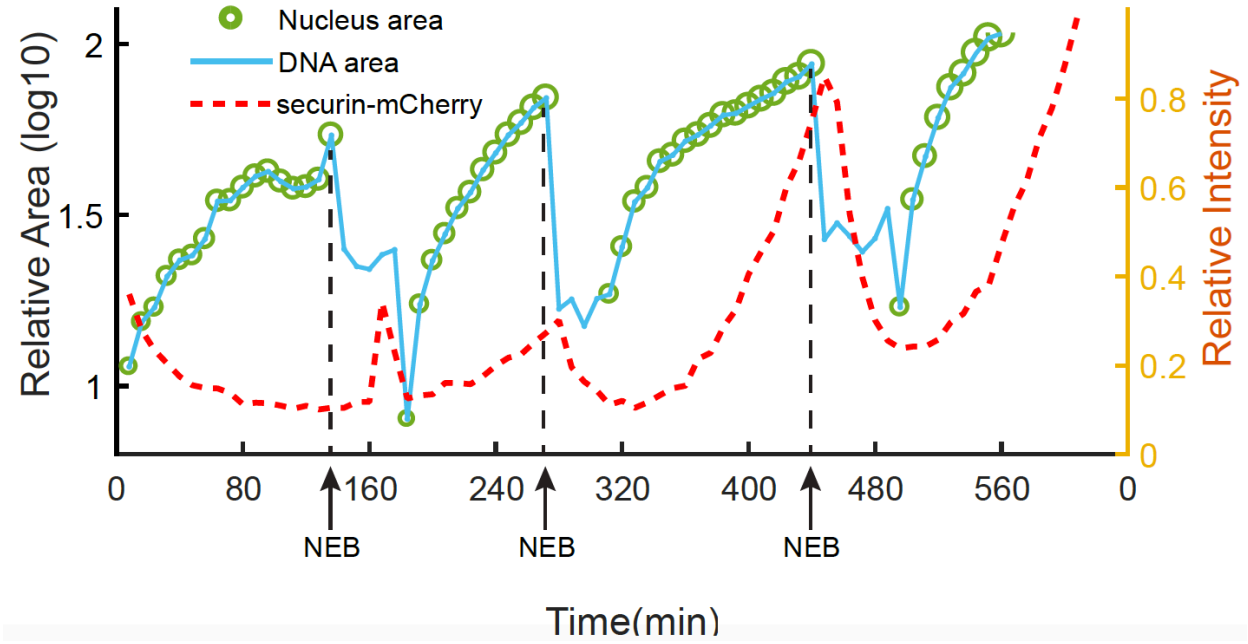

Figure 2.17 Multi-channel measurements for the droplet shown in Figure 2.16. The nucleus area (green circle) is calculated from the area of the nuclear envelope indicated by GFP-NLS, noting that the areas of the green circles are also scaled with the real areas calculated for the nuclei. The DNA area curve (blue line) shows the chromosome area identified by Hoechst 33342 dye. The chromosome condensation happens almost at the same time as the nuclear envelope breaks down (black dashed line). The red dashed line represents the intensity of securin-mCherry over time, suggesting that degradation of the APC/C substrate happens after nuclear envelope breakdown (NEB) consistently at each cycle.

In this section, we presented a high-throughput system that has a great potential for the study of tunability of the cell cycle clock. The preparation of cycling *Xenopus* extracts was

optimized to improve the oscillation ability of our mitotic oscillators. After comparing three loading methods, we proposed an approach to load droplets using three-dimensional glass chambers coated with Teflon. Moreover, our system enables simultaneous detections and measurements of multiple fluorescent reporters. To avoid any interference from the complicated nuclear dynamics, we reconstituted a minimal mitotic cycle system without sperm chromatin, which formed no nuclei. This simple and cytoplasmic-only oscillator produces undamped and self-sustained oscillations up to 32 cycles, significantly better than many existing synthetic oscillators. The results presented in this dissertation are reproducible in multiple replicates as discussed in different sections. Each replicate was conducted using different batches of *Xenopus* eggs to test the same experimental conditions.

2.4 Conclusion

Cell-free extracts have been powerful tools for the quantitative study of cell cycle processes including spindle assembly, chromosome segregation, and biochemical activities of essential cell-cycle regulators[38,43]. With the advantage of easy biochemical manipulations, extracts can be used to address mechanistic and biochemical questions that are difficult to assess using living cells. The *Xenopus laevis* egg extract is widely used to study the cell cycle *in vitro* such as nucleus formation and spindle assembly. The most significant advantages of *Xenopus laevis* eggs are the large volume of the oocytes and fast and synchronized cell cycles[38], which provide a concentrated cytoplasm for us to perform biochemical manipulations and reconstitute cellular events.

The cell cycle is driven by a protein circuit which is centered on Cdk1 and APC. Biochemical clocks can be measured by various fluorescent reporters as we discussed in this chapter including cyclin B1-YFP and securin-mCherry mRNAs. Demembranated *Xenopus* sperm

DNA and GFP-NLS can reveal the chromosome morphology, and indicate the nuclear envelope breakdown and reformation process. The signal of these reporters can be detected by fluorescence microscopes, from which we can quantitatively characterize cell cycle clock behaviors and study cell cycle regulations. We then applied these cell cycle clock reporters to our designed droplet system.

Robust and reliable spatial organization of the 3D environment in embryos is difficult to achieve[105,106]. Hereby, we described a highly interdisciplinary and novel strategy to reconstitute subcellular events with natural or synthetic components. By combining the cycling *Xenopus laevis* extract system in artificial cells with high-resolution fluorescence imaging, we proposed an approach to reconstituting the self-assembly process in mitotic oscillations and revealing the dynamic events in cell cycle clocks. This artificial cell system generates artificial cells at multi-scales and allows visualization and analysis of individual artificial cell behaviors. Our approach can reconstitute mitotic events and reproduce up to 32 undamped self-sustained cell cycles. Furthermore, we can study cell cycle dynamic events such as the tunability of oscillators using this artificial cell system.

CHAPTER III Applying the Artificial Cell System to the Study of Tunability of Cell Cycles

3.1 Introduction

Tunability widely exists in biological clocks and it is important for oscillators such cardiac impulses[156], neural spikes[157,158], and cell cycle oscillators[159,160]. However, previous studies on cell cycle tunability heavily rely on computational work and there is no experimental system to analyze tunability yet. An experimental system that is tunable and compatible for easy biochemical manipulation is of great importance to the field of system biology. Hereby, we will demonstrate that our artificial cell system developed in Chapter II can be applied for the study of tunability of cell cycles.

The *Xenopus laevis* extract has been one of the most widely used model systems to study the regulation and tunability of cell cycle oscillators[49,80,91,97,111,161]. The cell cycle clock is a protein circuit that is centered on the cyclin B-Cdk1 complex. If Cdk1 is active, Cdc25 will be activated, forming a double-positive feedback loop between Cdc25 and Cdk1. Meanwhile active Cdk1 inhibits its own inhibitor Wee1, forming a double-negative feedback loop[47,48,96]. Previous studies have shown that the double-positive and double-negative feedback loops constitute a bistable trigger[33,161], which is critical for the tunability and robustness of cell cycle oscillators[34,159].

Our droplet-based artificial cell system has a great potential to study mitotic oscillations. By tuning the input level of cyclin B1 mRNA and droplet size, our artificial oscillators are tunable as the oscillation period can be modulated. A/B testing[162,163] is a two-sample hypothesis testing

method to compare two versions of a single variable by testing a subject's response. A/B testing was applied in our experimental design: the control experiments were launched to assess the impact of multiple factors, *i.e.*, the dynamics of cell cycle clocks were simultaneously measured on the same batch of cycling *Xenopus* extracts with and without cyclin B1 mRNAs or demembranated sperm chromatin. Cell cycle behaviors were quantitatively measured by image processing and statistical analysis.

Hypothesis tests[164-168] were conducted to verify our experimental observations of the tenability of cell cycle clocks. If the p-value is lower than predefined significance level (usually 5%), then the null hypothesis is rejected[165,167,169-171], *vice versa*. Moreover, linear regression was applied to perform predictive data analysis[172,173]. A linear relationship between oscillator period and other predictors such as droplet radius, cyclin B1 mRNA was established to quantitatively predict oscillator behaviors.

3.2 Materials and methods

3.2.1 Experimental section

Cycling *Xenopus* extracts were freshly prepared as described in Section 2.2.1.1. The cycling extracts were collected in a 1.5 mL Eppendorf tube and kept on ice while supplied with 10 ng/μL recombinant mRNAs of securin-mCherry and cyclin B1-YFP (ranging from 0 to 10 ng/μL). Extracts were gently mixed and then supplemented with surfactant oil 2% PFPE-PEG to generate droplets. Detailed experimental methods of droplet generation and imaging were illustrated in Section 2.2.1.2. Droplets were segmented and tracked using Imaris 8.1.2. We analyzed droplets without demembranated sperm chromatin because nuclear breakdowns and formations induced by

sperm chromatin consume energy and may affect the dynamic behaviors of mitotic oscillators. The energy effect on cell cycle clocks will be further discussed in Chapter IV.

3.2.2 Artificial cell segmentation and tracking using Imaris

We used Imaris to analyze the droplet videos. Droplets were segmented and tracked under the bright field channel. After each frame was segmented, the segments were tracked between adjacent frames using the autoregressive motion algorithm. Some tracks were wrongly generated because the intensity of the bright field in the gaps between droplets was comparable to the intensity in a droplet. These tracks were removed manually. Statistics involving useful information for each track over time were exported from Imaris, including mean intensities of the channels, the standard deviations of the intensities of the channels, and the area of droplets. The volume of a droplet was calculated using the formula proposed by a previous study[99].

3.2.3 Noise removal and peak/trough selection

The mean intensity was noisy and made it difficult for subsequent analysis. The whole imaging area had similar levels of fluctuation for each frame, which was caused by instrument error. Thus, we subtracted background intensity from the measured intensity of our droplets for each time frame to eliminate the noise.

For period calculation, a peak/trough finding algorithm provided by Matlab 2014b was used to automatically detect peaks and troughs over the signal of mean intensity for cyclin B1-YFP and securin-mCherry. To make sure the behaviors of oscillators were accurately detected, we went through each droplet and made manual corrections.

3.3 Results and discussion

3.3.1 Image analysis

The oscillations indicated by securin-mCherry before and after noise removal is shown in Figure 3.1. Peaks and troughs became more pronounced after removing noise, especially for the first two oscillations, indicating that noise removal can help extract valuable statistical information for further analysis.

An example of a good peak/trough selection is shown in Figure 3.2. The sharp peak that reaches an intensity above 180 was due to a piece of debris with bright fluorescence, and the true peak, which is the bump slightly to the right, was manually selected. To guarantee the accuracy of our subsequent analysis, we did manual corrections to find out the right peak and trough positions. An example of the corrected result is shown in Figure 3.2.

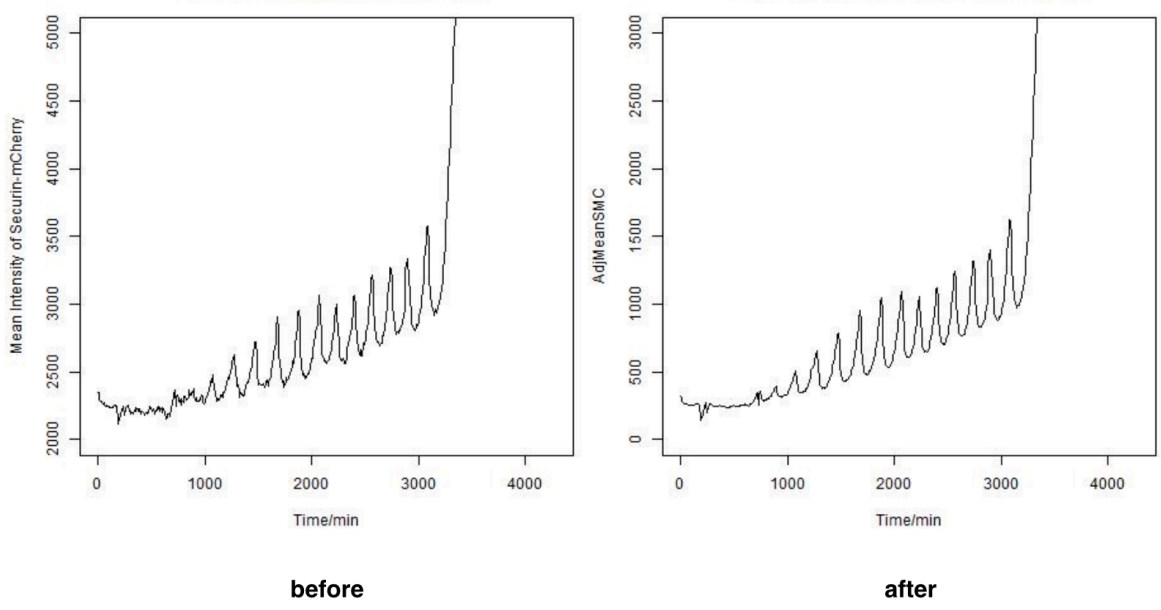

Figure 3.1 Cell cycles measured by securin-mCherry fluorescence signal. The left panel is the oscillation curve of segmentation and tracking before background noise removal. The right panel indicates the oscillation curve after noise removal.

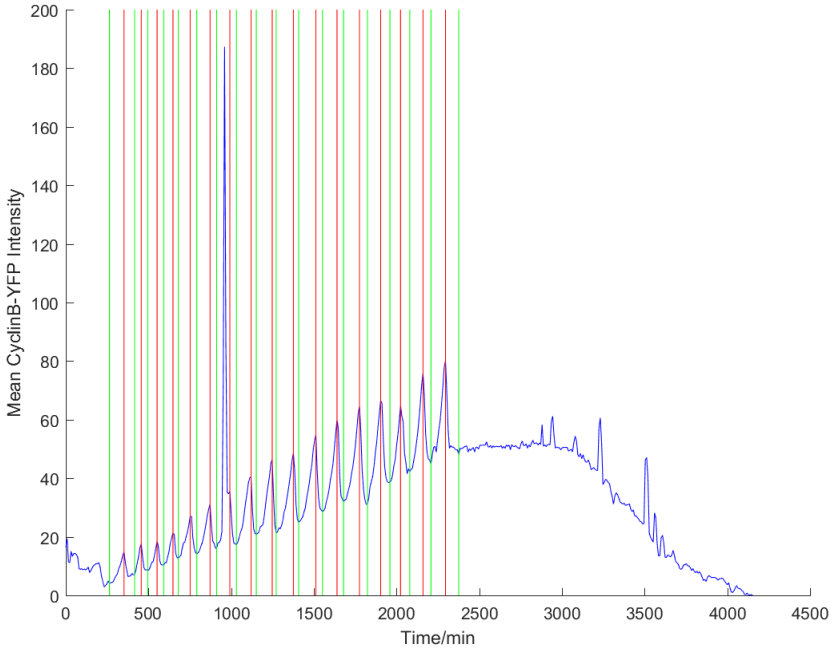

Figure 3.2 Peak and trough selection after manual correction.

3.3.2 Statistical analysis of the droplet size and cyclin B effects on oscillators

To modulate the speed of the oscillations, we supplied the system with various concentrations of cyclin B1-YFP mRNAs, which function both as a reporter of APC/C activity and an activator of Cdk1. As shown in the Figure 3.3, cyclin B1-YFP and securin-mCherry mRNAs exhibit highly correlated signals from three replicates, suggesting that both are reliable reporters for the oscillator activity.

Temporal study of cyclin B and securin is critical to understand the requirement of the onset of anaphase[174,175]. We measured both fluorescence time courses of cyclin B1 and securin as shown in Figure 3.3. The plot shows the quantitative analysis of the temporal dependence of securin-mCherry and cyclin B1-YFP oscillations. Their fluorescence time courses demonstrate that the degradations of securin and cyclin B1 are very similar to each other. Although their

temporal dependence is not the focus of this dissertation study, our system can be extended for this study in the future.

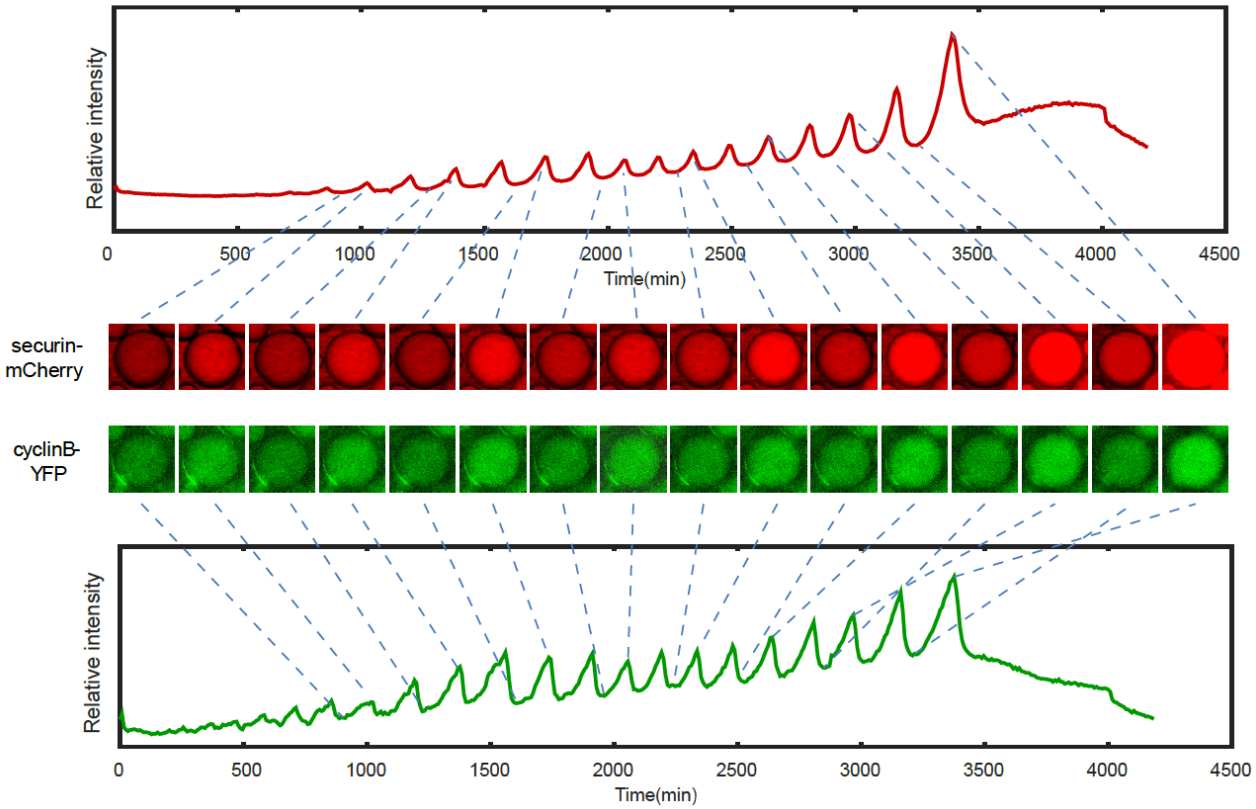

Figure 3.3 The cell cycle measurements by securin-mCherry and cyclin B1-YFP. The simultaneous measurements of fluorescence intensities of securin-mCherry (upper) and cyclin B1-YFP (lower) within the same droplet, show sustained oscillations for 58 hours. The series of mCherry and YFP images correspond to selected peaks and troughs in the time courses of fluorescence intensities. The two channels have coincident peaks and troughs for all cycles, suggesting that they both are reliable reporters for the cell cycle oscillators.

3.3.2.1 The behavior of the single droplet oscillator is size-dependent

This proposed cell-free system provides high flexibility in analyzing droplets with radii ranging from 20 μm to 500 μm, enabling characterization of size-dependent behaviors of cell cycles. At the scale of a cell, stochastic partitioning of key biomolecules with low concentrations may introduce variability in the initial conditions for oscillators, resulting in diverse dynamical behaviors. Although the stochastic phenomenon has been studied extensively in genetic expressions, studying an out-of-steady-state system is still challenging in living organisms due to the low throughput and complications from cell growth, divisions, and other complex cellular environments. These limitations can be overcome by reconstituting cell-scale *in vitro* oscillators in the absence of cell growth and divisions. Parallel tracking of droplets also enables data generation for statistical analysis. As shown in Figure 3.4, the colored areas represent droplets ranging from 25 percentiles to 75 percentiles. The equivalent diameter is defined as the cubic root of the volume of a droplet. Figures 3.4A shows that smaller droplets (equivalent radius < 50 μm) lead to slower oscillations and a larger variance of the periods, consistent with the size effect reported on an *in vitro* transcriptional oscillator [117]. As displayed in Figure 3.4B, droplets with larger equivalent diameter have more oscillations and increased variance of the number of cycles. The results are reproducible in three replicates. Size dependence of mitotic oscillations will be further discussed in Section 3.3.3.

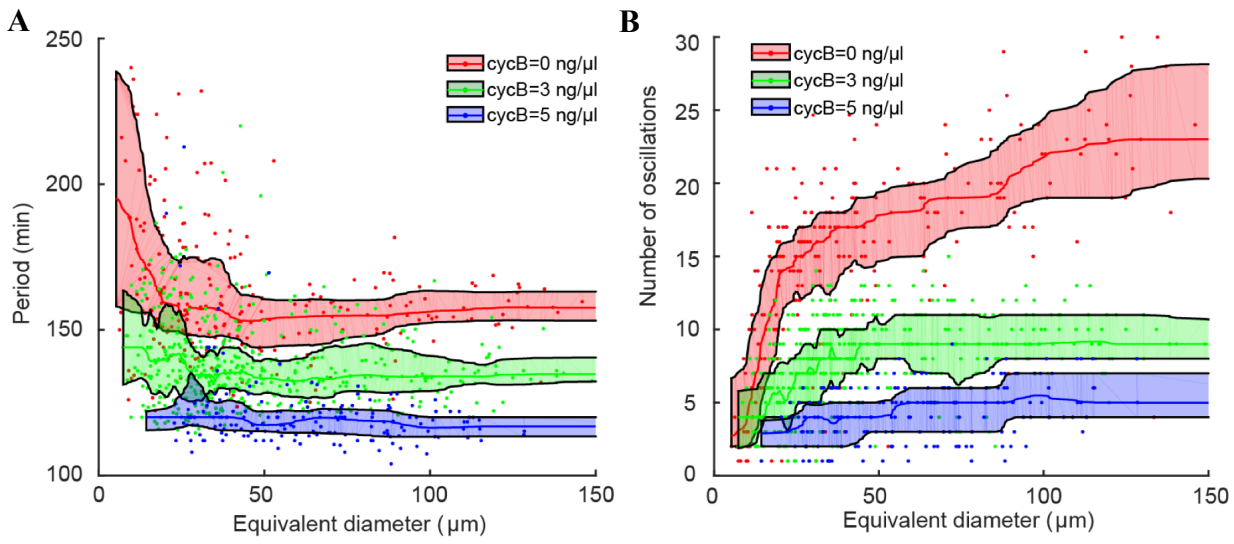

Figure 3.4 Droplet size effect on cell cycle clocks. A. Size effect on cell cycle period. B. Size effect on the number of oscillations.

3.3.2.2 The oscillator is effectively tunable in frequency with cyclin B1 mRNAs

As the concentration of cyclin B1-YFP mRNAs added to the system increased, we observed a decrease in the average period (Figure 3.5A), which demonstrates that a higher concentration of input cyclin B1 mRNA speeds up the oscillations. Meanwhile, the average number of cycles (Figure 3.5B) reduces as cyclin B1 concentration increases. Similar experimental phenomena were observed in three replicates. The extracts are eventually arrested at a mitotic phase in the presence of high concentrations of cyclin B1. Here, droplets of various sizes were collected for the analysis shown in Figure 3.5. To validate the effect of cyclin B1 mRNA on cell cycle behavior, more analysis will be shown later in Section 3.3.3.

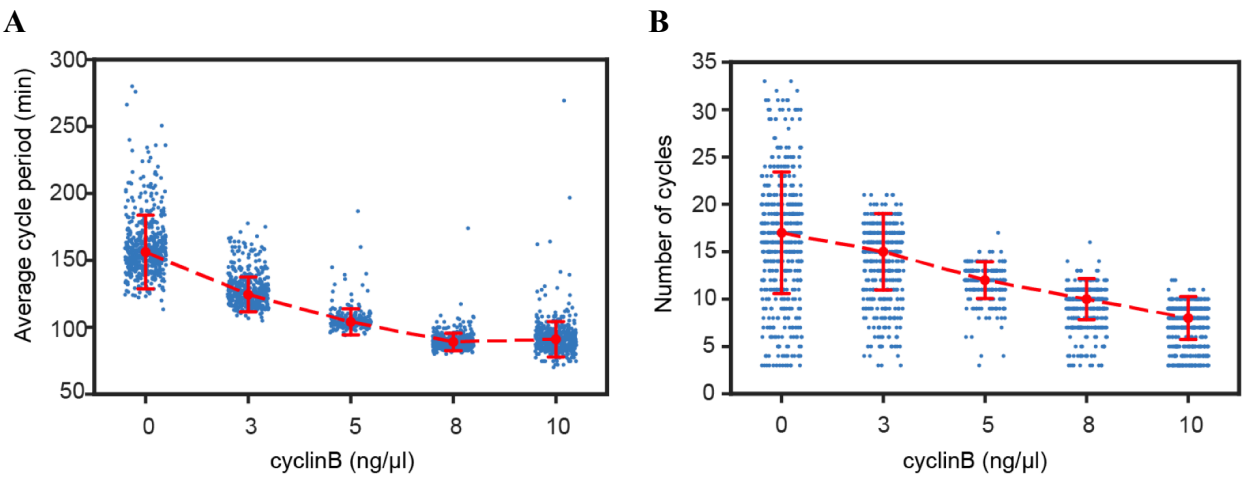

Figure 3.5 The oscillator is tunable in frequency (A) and number of cycles (B) as a function of the concentration of cyclin B1 mRNAs. Cyclin B1 not only functions as a substrate of APC/C but also binds to Cdk1 for its activation, functioning as an input of the cell cycle clock. The red dashed line connects medians at different conditions. The error bars indicate median absolute deviations (MAD).

3.3.3 Hypothesis test on droplet size effect

3.3.3.1 Normality test

To further investigate the size effect on cell cycle clock behaviors, we analyzed droplets of various sizes without any *Xenopus* sperm DNA and external cyclin B1 mRNA using Matlab. The cell cycle periods were calculated based on the oscillation periods from securin-mCherry fluorescence signal and we used the average period of all cycles for each droplet. Droplets were grouped into 15 groups based on their sizes, and the distribution of droplet size is shown in Figure 3.6. We can see that droplet radius ranges from 0 to 140 μm.

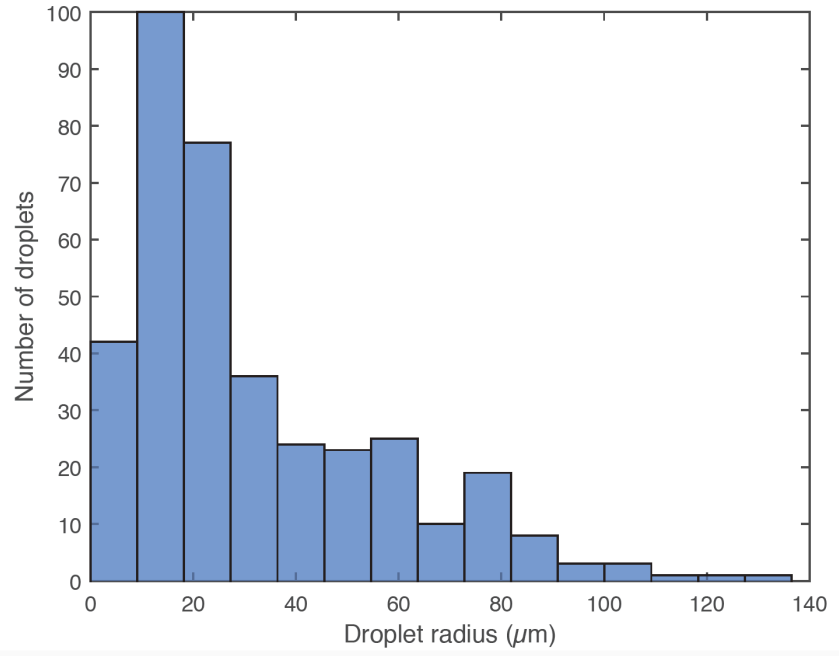

Figure 3.6 Histogram of droplet radius, which shows the distribution of droplet radius across the dataset.

A normality test was performed using the Kolmogorov-Smirnov test[176-178] ("kstest" function in Matlab). Its null hypothesis is that data points come from a standard normal distribution and alternative hypothesis is that data points do not come from such a distribution. Our data did not pass the normality test, suggesting that our data samples probability do not come from a standard normal distribution.

3.3.3.2 Kruskal-Wallis test

Analysis of variance (ANOVA) is a collection of statistical models that are used to analyze the differences among group means and variations. However, ANOVA has an assumption that samples come from a normal distribution. Since our data points are not normally distributed, the chance of a false positive result will increase if data is analyzed with ANOVA. Therefore, we used

the Kruskal-Wallis test[179,180], which is a non-parametric method to test if samples come from the same distribution. The null hypothesis is that the medians of all groups are equal and the alternative hypothesis is that at least one median is different from the others.

Table 3.1 Kruskal-Wallis ANOVA table for all 15 groups

Source	SS	df	MS	Chi-sq	Prob>Chi-sq
Groups	174863.70	14	12490.30	15.71	0.33
Error	3877320.30	350	11078.10	--	--
Total	4052184.00	364	--	--	--

Specifically, we used the Kruskal-Wallis test to compare all the droplets in the 15 different size groups and the p-value is 0.33 (Table 3.1), indicating that droplet size does not affect cell cycle period significantly overall. However, Figure 3.7D shows that the cell cycle period is size dependent when the droplet size is small. To investigate the turning point at which the droplet size no longer affects cell cycle clock significantly, more Kruskal-Wallis tests were performed on droplets from the first six, seven, and eight size groups, where droplets were grouped based on radii from small to large.

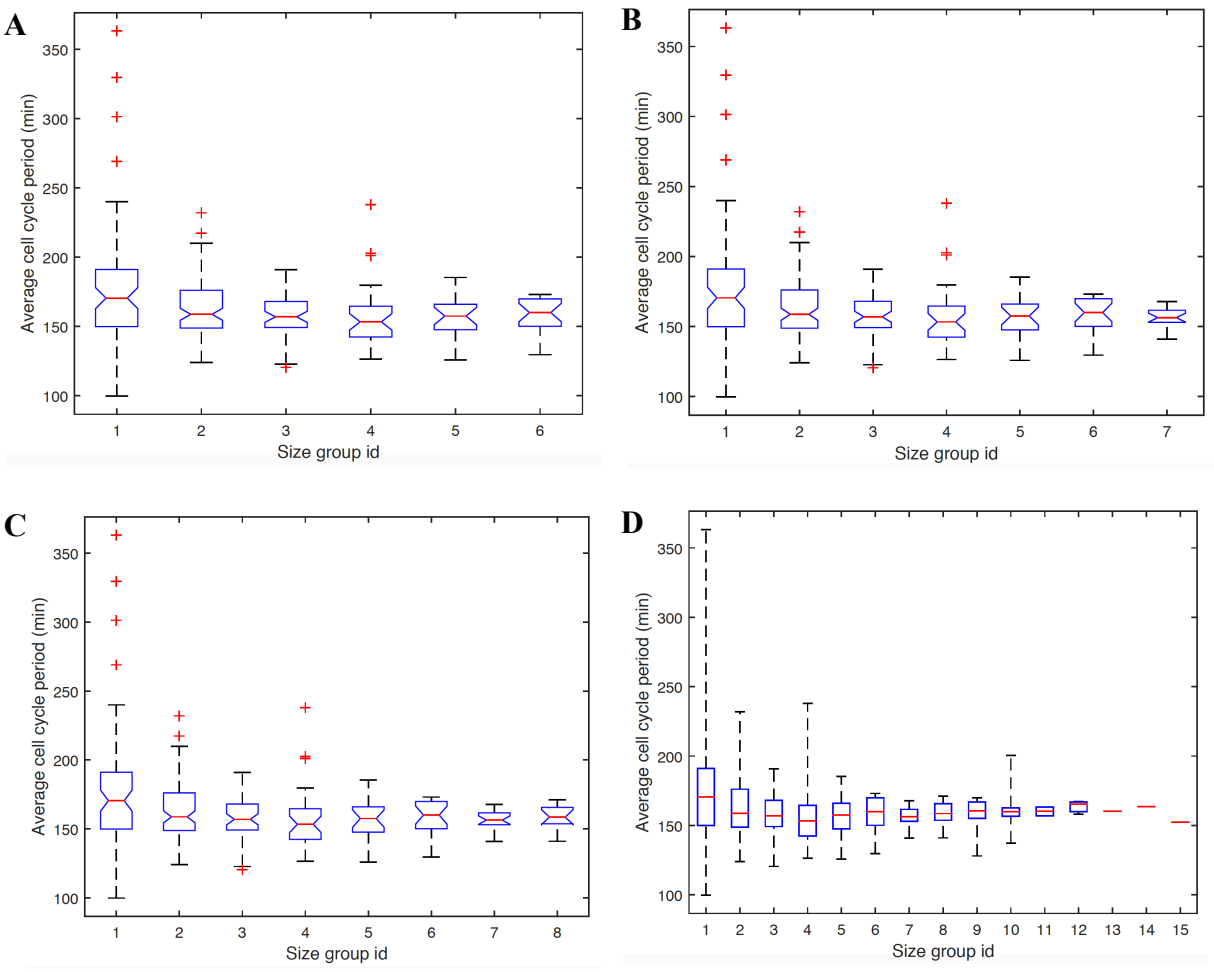

Figure 3.7 Boxplots of the average cell cycle periods for droplets of different size groups. The analysis of the first 6, 7, 8, and all 15 size groups are shown in panel A, B, C, D.

Table 3.2 Kruskal-Wallis ANOVA table for the first six groups

Source	SS	df	MS	Chi-sq	Prob>Chi-sq
Groups	90585.10	5	18117.01	12.04	0.03
Error	2159352.90	294	7344.74	--	--
Total	2249938.00	299	--	--	--

Table 3.3 Kruskal-Wallis ANOVA table for the first seven groups

Source	SS	df	MS	Chi-sq	Prob>Chi-sq
Groups	111122.00	6	18520.30	13.06	0.04
Error	2593958.00	312	8314.00	--	--
Total	2705080.00	318	--	--	--

Table 3.4 Kruskal-Wallis ANOVA table for the first eight groups

Source	SS	df	MS	Chi-sq	Prob>Chi-sq
Groups	122622.50	7	17517.50	13.39	0.06
Error	2899367.00	323	8976.40	--	--
Total	3021989.50	330	--	--	--

As listed in Table 3.2-3.4, the p-values of the first 6, 7, and 8 groups are 0.03, 0.04, and 0.06, respectively. Since the p-value of the first 8 groups is 0.06, which exceeds 0.05, we can conclude that starting from the 8^{th} group, droplet size does not have a significant effect on the cell cycle period. The 8^{th} droplet size group ranges from 65.24 μm to 74.02 μm. Therefore, the cell cycle behavior is significantly size dependent when droplet size is smaller than 65 μm.

3.3.4 Hypothesis test on cyclin B effect

3.3.4.1 Normality test

To study the cyclin B effect on cell cycle clocks, we need to use droplets of similar sizes and different concentrations of external cyclin B1 mRNA. To eliminate the size dependence, we selected droplets that had a radius larger than 65 μm based on the analysis in Section 3.3.3. A normality test was performed on droplets with various concentrations (0, 3, 5, 8, 10 ng/μL) of external cyclin B1 mRNA and the test results are shown in Table 3.5. All groups passed the normality test. Here, we only considered droplets without any sperm DNA. Later, we will test whether adding *Xenopus* sperm DNA or not affects oscillations in Section 3.3.5.

Table 3.5 Normality test for droplets with different cyclin B1 mRNA concentrations

[Cyclin B1] (ng/μL)	0	3	5	8	10
Normality test	0	0	0	0	0
p-value	0.26	0.93	0.73	0.76	0.08
Number of droplets	46	40	14	31	45

3.3.4.2 ANOVA test

Since all groups of droplets passed the normality test, the ANOVA was applied to compare the average cell cycle periods among various groups. From the ANOVA results (Figure 3.8) and the p-value (3.19e-69) shown in Table 3.6, we can conclude that cyclin B1 concentration has a significant effect on cell cycle behaviors.

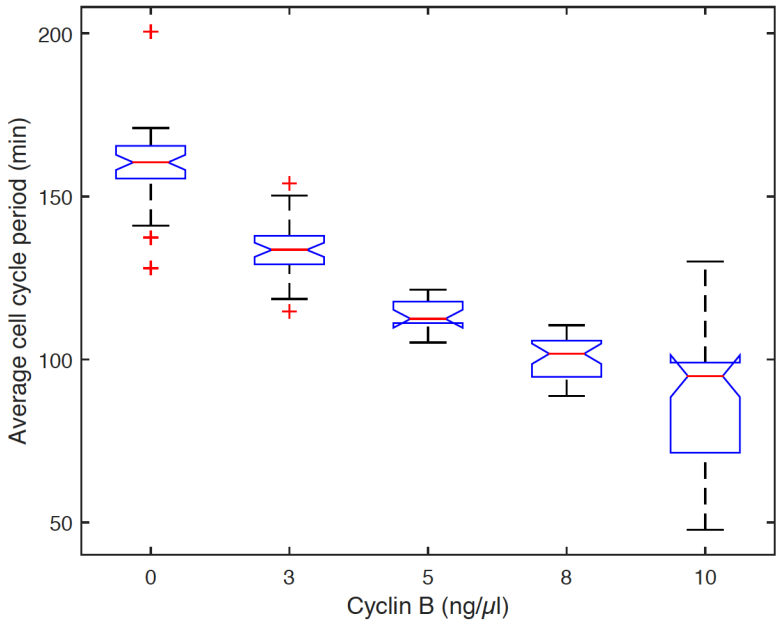

Figure 3.8 Boxplot of the average cell cycle periods for droplets with various concentrations of cyclin B1 mRNAs at 0, 3, 5, 8, 10 ng/μL.

Table 3.6 ANOVA table for the five groups with different cyclin B1 mRNA concentrations

Source	SS	df	MS	F	Prob>F
Groups	137632.70	4	34408.20	241.63	3.19e-69
Error	24350.00	171	142.40	--	--
Total	161982.70	175	--	--	--

3.3.5 Hypothesis test on *Xenopus* sperm DNA effect

When droplets were supplied with sperm DNA, they had different dynamic behaviors in our experiments. As shown in Figure 3.9, the average oscillation periods of droplets with and without sperm DNA vary significantly, and adding sperm DNA can slow down the oscillation

speed. This result is reproduced in three replicates. To perform confirmatory data analysis on the effect of sperm DNA, we applied hypothesis tests. None of the droplets for the test were applied with external cyclin B1 and only droplets with radii greater than 65 μm were considered to avoid size dependence.

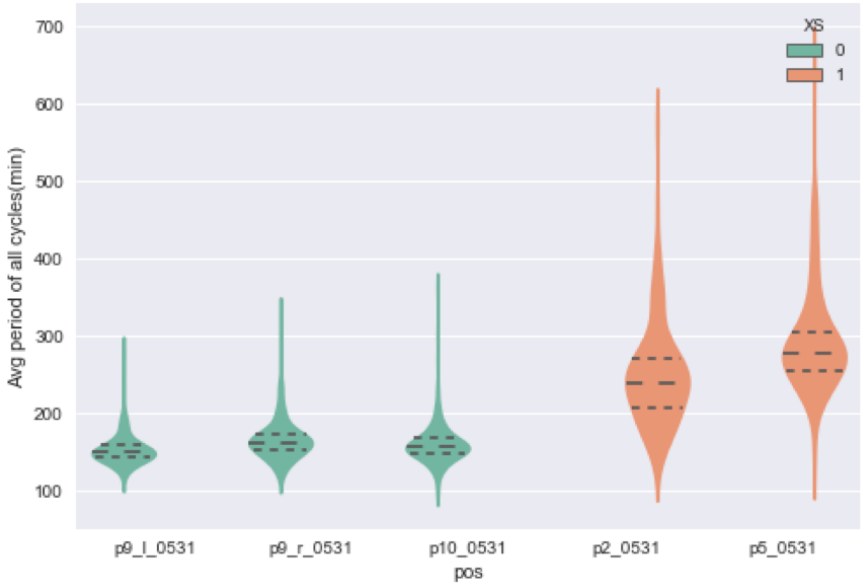

Figure 3.9 Orange and green boxes represent the average cycle periods of the droplets with and without sperm DNA, respectively. Data was collected from three groups of the droplets without sperm DNA and two groups with sperm DNA.

3.3.5.1 Normality test

We applied the normality test for two groups of droplets seprately. As listed in Table 3.7, both groups passed the test, which indicates that they are eligible for the two-sample t-test.

Table 3.7 Normality test for droplets with or without sperm DNA

	Normal test result	p-value	Number of droplets
Without sperm DNA	0	0.26	46
With sperm DNA	0	0.98	21

3.3.5.2 Two-sample t-test

To determine if the means of two droplet groups are equal, one of the most commonly used hypothesis tests is the two-sample t-test. The null hypothesis is that two means are equal and alternative hypothesis is that the means are different.

Table 3.8 Two-sample t-test result

p-value	Confidence interval	T statistic	df	sd
2.18e-24	[-115.55, -90.07]	-16.11	65	24.23

Since the p-value from the t-test is 2.18e-24 as shown in Table 3.8, we can conclude that the means of two droplet groups with or without sperm DNA are significantly different. The influence of applying sperm DNA to extract is statistically significant on the period of cell cycle oscillations.

3.3.6 Linear regression to predict cell cycle period

3.3.6.1 Understanding data and variables graphically

Linear regression is widely used to predict the value of a response using the information of one or multiple predictors and build a linear relationship between predictors and the response. To reveal the relationship between cell cycle clock behaviors and multiple potential predictors such as number of cycles, droplet radius, adding sperm DNA or not, and external cyclin B1 mRNA concentration, 2254 droplets were used for analysis. First, graphical analysis and correlation study were performed to analyze and understand variables. Boxplots (Figure 3.10) were used to check

for outliers. Droplets that exceeded the 1.5 times interquartile range (IQR) were considered as outliers.

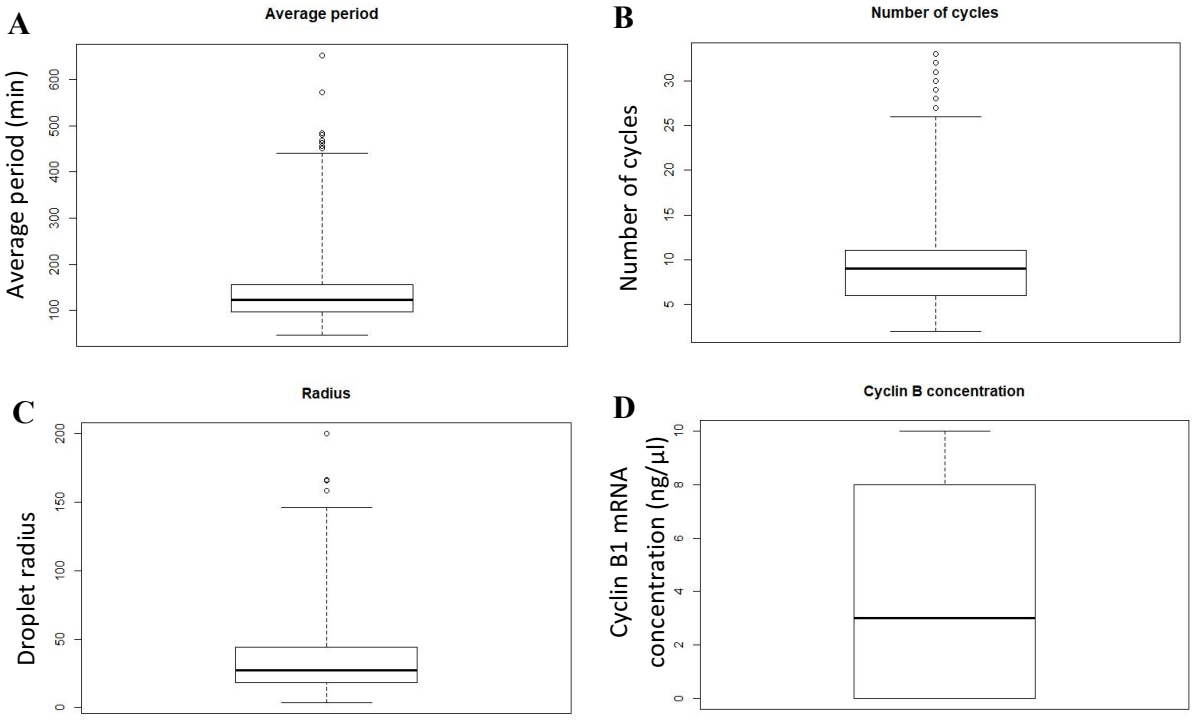

Figure 3.10 Outlier detection for multiple variables. A. Average period. B. Number of cycles. C. Radii of droplets. D. Concentration of cyclin B1 mRNAs.

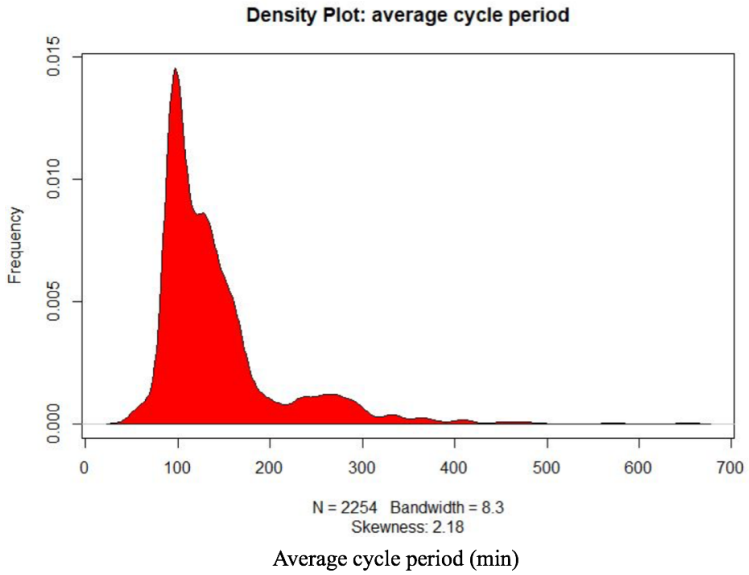

Figure 3.11 Density plot of average cell cycle periods

Density plot of the response (Figure 3.11) was used to check if the distribution is close to normality. We can see that the distribution of the response variable (average cell cycle period) is skewed. Moreover, the normality test indicates that the outcome is not normally distributed.

Correlation between predicators was applied to statistically measure the level of collinearity between every pairs of predicators. A high positive correlation close to 1 means that the two predictors are highly correlated. If the correlation between two variables is close to -1, then the variables have a strong negative correlation. A value close to 0 suggests that the variables have a relatively weak relationship between each other.

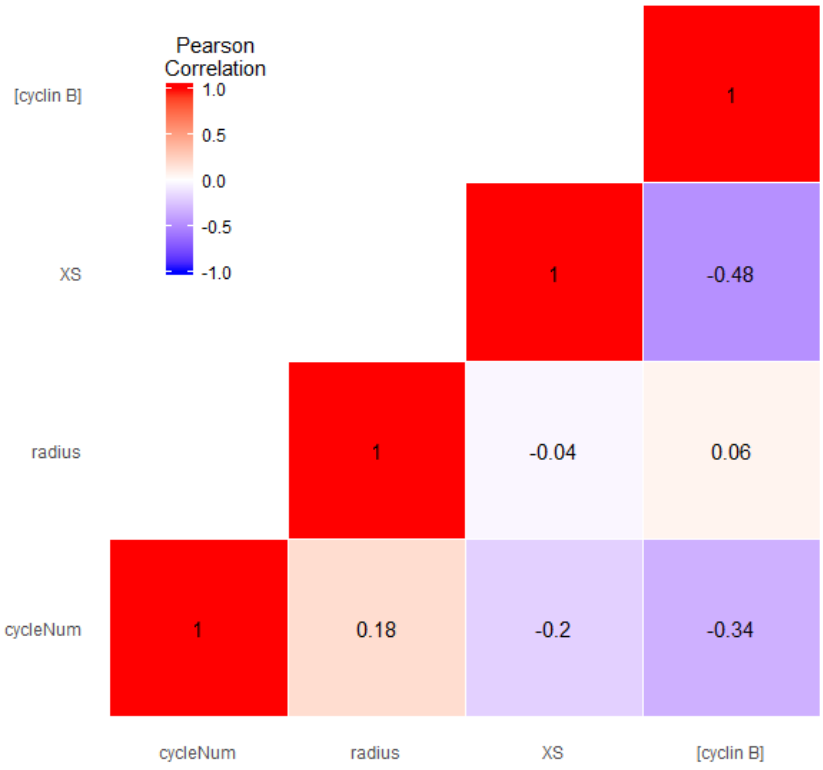

Figure 3.12 Correlation matrix between multiple variables including number of cycle, droplet radius, sperm DNA and concentration of cyclin B1 mRNAs.

The correlation matrix (Figure 3.12) shows that sperm DNA (XS) and cyclin B1 mRNA concentration are negatively correlated, which is mainly induced by manual factor since sperm DNA was only added to extract without any external cyclin B1 mRNA. The concentration of externally added cyclin B1 mRNAs and number of cell cycles also have a strong negative correlation which is corresponded to the results shown in Figure 3.5B.

3.3.6.2 Building a linear regression model

In this section, we built a linear regression model to analyze how the factors affect the cell cycle period quantitatively from a statistical perspective. To simplify the complexity of modeling, we only took measurable variables into consideration including droplet radius, adding sperm DNA or not, and the concentration of cyclin B1 mRNA. The number of cycles was not involved here because it was not statistically significant for the prediction of cycle period in our initial model (p-value=0.91). The summary of our proposed model is listed in the Table 3.9. We can see that all the variables have small p-values which indicate that they are highly related to the cell cycle period.

Table 3.9 Coefficient table for linear regression model

	Estimate	Std. error	t value	Pr (>|t|)	R^2
(Intercept)	125.43	0.72	173.20	<2e-16	0.80
Radius	-1.07	0.66	-1.61	0.11	
Sperm DNA	111.69	2.18	51.17	<2e-16	
[CyclinB1 mRNA]	-27.05	0.75	-35.94	<2e-16	

Specifically, the equation of our model is:

Average cell cycle period

=125.43-1.07 * Radius+111.70* I (sperm DNA is applied)-27.05 * [cyclin B1 mRNA],

where I (sperm DNA is applied) is an indicator function. If sperm DNA is added, I (sperm DNA is applied) equals 1, and 0 otherwise.

The R squared value is 0.80 which is higher than 0.70, indicating that the linear regression model was well fitted. This model indicates that larger droplet radius leads to longer cycle period, adding sperm DNA increases cycle period, and higher concentration of external cyclin B1 mRNA speeds up the oscillations. These conclusions are prospective and consistent with our experimental observations.

3.4 Conclusion

The cell cycle clock oscillations were quantitatively measured by fluorescence intensity changes of various reporters including securin-mCherry and cyclin B1 mRNAs. Droplets were successfully segmented and tracked using Imaris. We normalized the fluorescence intensity in droplets with the intensity time trace of background, and the signal to noise of the oscillations of cell cycle clocks was greatly improved. Our initial statistical analysis indicates that the oscillators may be tunable in frequency with cyclin B1-YFP mRNAs and the behavior of single droplet oscillators is size dependent.

To further investigate the tunabililty of cell cycle clock, we performed several hypothesis tests on size of droplets, concentration of external cyclin B1 mRNAs, and sperm DNA effects on

cycle periods. The test results suggest that the behavior of single droplet oscillators with a radius smaller than 65 μm is significantly size dependent and smaller droplets have longer cycle periods. Moreover, inducing more cyclin B1 mRNAs into our droplet system can accelerate oscillations while adding sperm DNA can slow down oscillations. We also fitted a linear regression model to predict average oscillation period using predictors including droplet radius, adding sperm DNA or not and concentration of cyclin B1 mRNAs. The R squared value exceeds 0.70, indicating our model was well fitted. To summarize, the artificial single cell oscillators are tunable by changing the level of input cyclin B1 mRNAs, size of droplets, and inducing sperm DNA.

This chapter shows that the mitotic oscillators created by our artificial cell system are tunable, demonstrating that this system is amenable to study the dynamic behaviors of cell cycle oscillators. The proposed system can be used for high-throughput, quantitative manipulation and analysis of both cytoplasmic and nuclear processes. Given cell cycles share common topologies with many biological oscillators, the system may be valuable to investigate fundamental principles of oscillator theory.

CHAPTER IV Applying the Artificial Cell System to the Study of Energy Dependence of Cell Cycles

4.1 Introduction

Mathematical modeling has been used to reveal the principles underlying cell cycle behaviors[82,159]. The first ordinary differential equation (ODE) models for *Xenopus laevis* embryonic cell cycles were established in previous studies[49,181,182]. More complicated models have been proposed to describe the embryonic cell cycle oscillations[31,34,183,184], but some parameters of these complex models[47,48,96] are not measurable in the experiments. Recently, Yang et al[46] and Tsai et al[91] proposed simple two-ODE models with fewer parameters, while still capturing the general property of the feedback loops. As discussed in Chapter III, we observed increasing amplitude, baseline, and period over time indicated by both securin-mCherry and cyclin B1-YFP reporters. However, existing cell cycle models cannot explain the above experimental observations.

Energy supply is important for cell cycle oscillations because cell cycle keeps consuming energy[185-187]. Unlike intact embryos, cell-free extracts lack yolk as an energy source and sufficient mitochondria for energy regeneration. Thus, the effect of energy consumption on the dynamic behaviors of mitotic oscillators is significant[188,189] and worth discussion. We postulated that energy is an important regulator for a droplet system with limited amount of energy source. To gain insight into our experimental observations and better understand the *in vitro* oscillator system, we built a stochastic model to simulate how energy consumption plays a role in the oscillation behaviors.

The positive circuits regulating cyclin B-Cdk1 activation through Wee1 and Cdc25 play an important role in the bistability transition of mitotic oscillators. Therefore, we mainly considered energy effect in three key reactions: Wee1 inactivation, Cdc25 activation and cyclin B-Cdk1 complex inactivation[190]. The energy depletion model was based on a well-established cell-cycle model[46,191] modified by introducing ATP into all phosphorylation reactions. This modeling work was in collaboration with Zhengda Li and Xuwen Liu.

The energy dependence of cell cycle clocks suggested by our stochastic two-ODE model can be validated by varying energy level for different groups of droplets generated by our artificial cell system. To monitor energy changes, real-time ATP measurement assay needs to be applied to our cell-free system. The relationship between energy and cell cycle clock behaviors can be characterized by performing quantitative analysis of droplets encapsulated with different concentrations of energy solution.

4.2 Materials and methods

Matlab R2016b (Mathworks Inc.) was used to solve the ODE models numerically. Model parameters are listed in Table 4.1. A stochastic two-ODE model from Yang and Ferrell's work[46] was adapted and our two-ODE model was converted to the corresponding chemical master equations (Kampen's work[192]). Gillespie algorithm[193] was applied to carry out numerical stochastic simulations.

4.3 Computational modeling

4.3.1 A two-ODE model of the embryonic cell cycle

Here we first constructed a simple two-ODE model. The first ODE equation describes the synthesis and degradation of total cyclin B [46,191]:

$$\frac{d}{dt}[CyclinB] = k_{sy} - k^*_{\deg}[CyclinB] = k_{sy} - \left(a_{deg} + \frac{b_{deg}[Cdk1_a]^{n_{deg}}}{[Cdk1_a]^{n_{deg}} + EC50_{deg}^{n_{deg}}}\right)[CyclinB] \qquad Eq.1$$

In Eq. 1, $[Cdk1_a]$ refers to the concentration of active cyclin B-Cdk1 complex. Here, we assumed that cyclin B is synthesized at a constant rate. $EC50_{deg}^{n_{deg}}$ is a bifurcation parameter for various assumed Hill exponents n_H. The degradation rate is in the form of Hill Function[96] with exponent of 17. Since the concentration of Cdk1 is much higher than the maximum concentration of cyclin B[194] and the binding affinity of cyclin B to Cdk1 is high[195], we assumed that cyclin B binds to Cdk1 as soon as cyclin B is translated by mRNAs.

To further simplify the model, we assumed that the cyclin B-Cdk1 complex is activated by CAK (Cdk1-activating Kinase) as soon as it forms, thus the synthesis of cyclin B leads to active Cdk1. Through double-positive and double-negative feedbacks, active cyclin B-Cdk1 can be inactivated by Wee1 and reactivated by Cdc25. The overall ODE equation for Cdk1 is:

$$\begin{aligned}\frac{d}{dt}[Cdk1_a] &= k_{sy} + k^*_{\text{Cdc25}}[Cdc25 - Pi]([CyclinB] - [Cdk1_a]) - k^*_{\text{Wee1}}[Wee1][Cdk1_a] - k_{deg}[Cdk1_a] \\ &= k_{sy} + \left(a_{Cdc25} + \frac{b_{Cdc25}[Cdk1_a]^{n_{Cdc25}}}{[Cdk1_a]^{n_{Cdc25}} + EC50_{Cdc25}^{n_{Cdc25}}}\right)([CyclinB] - [Cdk1_a]) - (a_{Wee1} \\ &+ \frac{b_{Wee1}EC50_{Wee1}^{n_{Wee1}}}{[Cdk1_a]^{n_{Wee1}} + EC50_{Wee1}^{n_{Wee1}}})[Cdk1_a] - (a_{deg} \\ &+ \frac{b_{deg}[Cdk1_a]^{n_{deg}}}{[Cdk1_a]^{n_{deg}} + EC50_{deg}^{n_{deg}}})[Cdk1_a] \end{aligned} \qquad Eq.2$$

In Eq. 2, $[Wee1]$ stands for the concentration of active Wee1, while $[Cdc25 - Pi]$ stands for the concentration of active Cdc25-Pi. The Hill exponent of n_{Wee1} is 3.5 and n_{Cdc25} is 11, tested by previous studies[48,96]. The nullclines of Cyclin B and Cdk1 satisfy the following equations:

$$\frac{d}{dt}[CyclinB] = 0, \frac{d}{dt}[Cdk1_a] = 0$$

Here, $[CyclinB]$ and $[Cdk1_a]$ refer to the concentrations of cyclin B and active cyclin B1-Cdk1 complex. It should be noticed that when using Hill function to describe the regulation effect, the

assumption of fast reaction and steady state approximation are applied. In the cell cycle networks, the activation of Cdk1 is co-regulated by a double-positive feedback through a phosphatase Cdc25 and a double-negative feedback though a kinase Wee1. The balance between Wee1 and Cdc25 activity is crucial for the transition of cell cycle status during early embryo development[91]. We defined the balance between Wee1 and Cdc25 by the ratio $R = \frac{k_{Wee1}[Wee1]}{k_{Cdc25}[Cdc25]}$. Oscillation behaviors vary as the ratio R changes. To simply describe the changes of R, another parameter r was introduced[91]. The second ODE equation is shown as below:

$$\begin{aligned}\frac{d}{dt}[Cdk1_a] = k_{sy} + \frac{1}{\sqrt{r}}\left(a_{Cdc25} + \frac{b_{Cdc25}[Cdk1_a]^{n_{Cdc25}}}{[Cdk1_a]^{n_{Cdc25}} + EC50_{Cdc25}^{n_{Cdc25}}}\right)([CyclinB] - [Cdk1_a]) \\ - \sqrt{r}\left(a_{Wee1} + \frac{b_{Wee1}EC50_{Wee1}^{n_{Wee1}}}{[Cdk1_a]^{n_{Wee1}} + EC50_{Wee1}^{n_{Wee1}}}\right)[Cdk1_a] \\ - \left(a_{deg} + \frac{b_{deg}[Cdk1_a]^{n_{deg}}}{[Cdk1_a]^{n_{deg}} + EC50_{deg}^{n_{deg}}}\right)[Cdk1_a]\end{aligned} \qquad Eq.3$$

The parameter values for the model are listed in Table 4.1.

Table 4.1 List of the values for model parameters

k_{sy}	1 nM/min
a_{wee1}	0.08 nM/min
b_{wee1}	0.40 nM/min
n_{wee1}	3.50
$EC50_{wee1}$	35 nM
a_{cdc25}	0.16 nM/min
b_{cdc25}	0.80 nM/min
n_{cdc25}	11
$EC50_{cdc25}$	30 nM
a_{deg}	0.01 nM/min
b_{deg}	0.04 nM/min
n_{deg}	17
$EC50_{deg}$	32 nM

4.3.2 A stochastic two-ODE model of the embryonic cell cycles

In droplets that have small volumes and contain small numbers of molecules, the stochastic nature of the underlying biochemical reactions must be considered. We adapted a stochastic two-ODE model[46], and converted our two-ODE model to the corresponding chemical master equations[192] and carried out numerical simulations using the Gillespie algorithm[193]. The reaction rates and molecular stoichiometry are shown in Table 4.2. $< Cdk1_a >$ means the molecule number of active cyclin B-Cdk1 and $< Cdk1_i >$ refers to the molecule number of inactive cyclin B-Cdk1. We followed the parameters in Yang and Ferrell's work[46], transforming the unit from concentration to molecular number.

Table 4.2 Reaction rates and stoichiometry of the stochastic two-ODE model

Reaction	Rate	Stoichiometry
Active Cdk1 Synthesis	$\rho_1 = k_{sy}$	$< Cdk1_a >=< Cdk1_a > +1$
Active Cdk1 to Inactive Cdk1	$\rho_2 = \sqrt{r}\left(a_{Wee1} + \frac{b_{Wee1} EC50_{Wee1}^{n_{Wee1}}}{<Cdk1_a>^{n_{Wee1}} + EC50_{Wee1}^{n_{Wee1}}}\right) < Cdk1_a >$	$< Cdk1_a >=< Cdk1_a > -1$ $< Cdk1_i >=< Cdk1_i > +1$
Inactive Cdk1 to Active Cdk1	$\rho_3 = \frac{1}{\sqrt{r}}\left(a_{Cdc25} + \frac{b_{Cdc25} <Cdk1_a>^{n_{Cdc25}}}{<Cdk1_a>^{n_{Cdc25}} + EC50_{Cdc25}^{n_{Cdc25}}}\right) < Cdk1_i >$	$< Cdk1_a >=< Cdk1_a > +1$ $< Cdk1_i >=< Cdk1_i > -1$
Active Cdk1 Degradation	$\rho_4 = \left(a_{deg} + \frac{b_{deg} <Cdk1_a>^{n_{deg}}}{<Cdk1_a>^{n_{deg}} + EC50_{deg}^{n_{deg}}}\right) < Cdk1_a >$	$< Cdk1_a >=< Cdk1_a > -1$
Inactive Cdk1 Degradation	$\rho_5 = \left(a_{deg} + \frac{b_{deg} <Cdk1_a>^{n_{deg}}}{<Cdk1_a>^{n_{deg}} + EC50_{deg}^{n_{deg}}}\right) < Cdk1_i >$	$< Cdk1_i >=< Cdk1_i > -1$

4.3.3 A stochastic two-ODE model of the embryonic cell cycles including energy effect

In our *in vitro* cell-free system, the energy supplying system is not as efficient as in embryonic cells, which makes energy critical for our mitotic oscillators. To improve the model's prediction ability, energy dependence was considered in our optimized model. In mitotic oscillators, energy plays a key role in three important reactions including Wee1 inactivation, Cdc25 activation, and cyclin B-Cdk1 complex inactivation (Figure 4.1). To further investigate the tunability of cell cycle oscillators and explain our observations of increased baseline, amplitude, and period, we built a stochastic two-ODE model of the embryonic cell cycles including energy dependence.

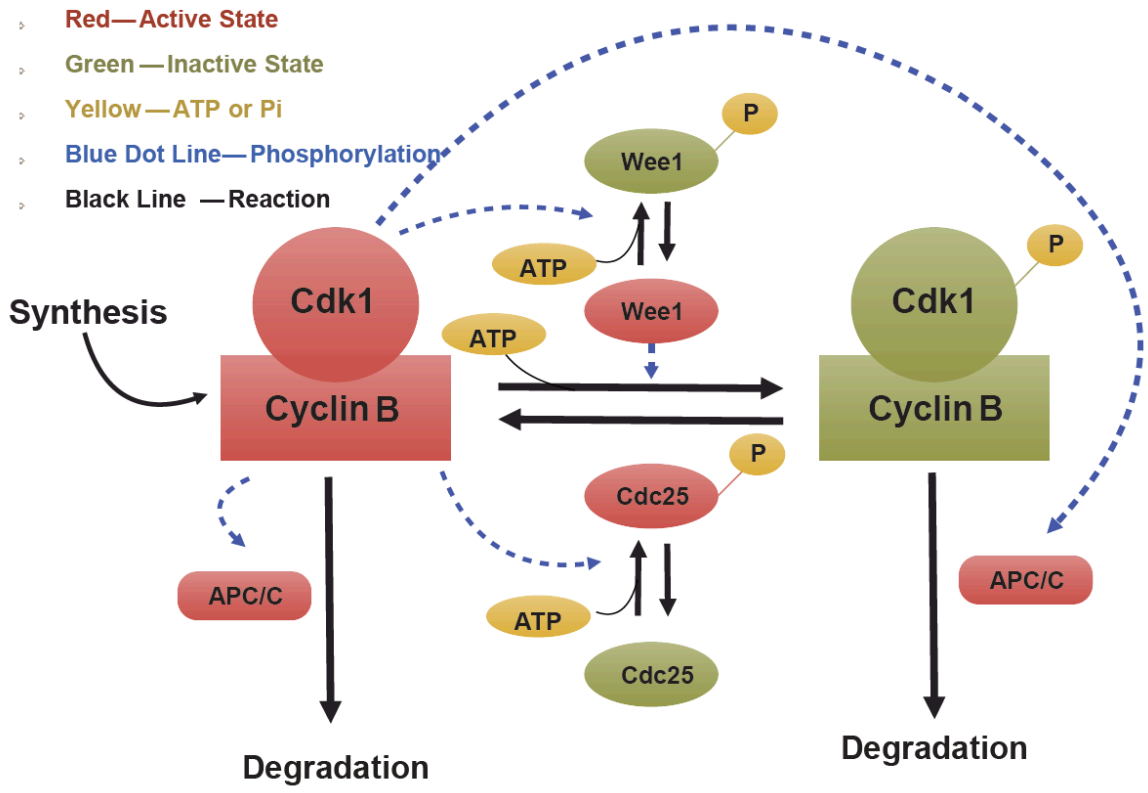

Figure 4.1 Schematic view of the cyclin B-Cdk1 oscillation system. Note that ATP is taken into consideration. Activated molecules are marked in red, inactivated molecules in green and ATP or Pi in yellow. Black lines indicate reactions and blue dotted lines phosphorylations.

In this model, we focused on three reactions that involve ATP: Wee1 inactivation, Cdc25 activation, and cyclin B-Cdk1 inactivation[190]. To explore how energy consumption could affect the oscillations, we took ATP into account for phosphorylation and dephosphorylation of Wee1 [190], such that:

$$Wee1 + ATP \leftrightarrow Wee1 - Pi + ADP \qquad Eq.4$$

We assumed that Wee1 is in equilibrium with the activity of Cdk1 due to fast reactions between Cdk1 and Wee1. Let's denote the reaction coefficients for Wee1 phosphorylation as k_{1Wee1} and that for Wee1-Pi dephosphorylation as k_{2Wee1}, along with the steady-state approximation, we have:

$$k_{1Wee1}[Wee1][ATP] = k_{2Wee1}[Wee1 - Pi][ADP] = k_{2Wee1}([Wee1_{tot}] - [Wee1])(1 - [ATP]) \qquad Eq.5$$

Notice when writing the equation above, we normalized $[ATP] + [ADP]$, and we did not consider AMP in this system. $[ATP]$ refers to the ratio of $\frac{[ATP]}{[ATP]+[ADP]}$. For the initial model not including ATP, we have the equation:

$$K_{Wee1}[Wee1_0] = a_{Wee1} + b_{Wee1}\left(\frac{EC50_{Wee1}^{nWee1}}{EC50_{Wee1}^{nWee1} + < Cdk1_a >^{nWee1}}\right) \qquad Eq.6$$

$[Wee1_0]$ refers to the Wee1 concentration in the original model, and $[Wee1_{tot}]$ refers to the total Wee1 concentration. Whether considering ATP or not, we assumed that K_{Wee1} and $[Wee1_{tot}]$ remain the same. Thus, from Eq.5-6, we can deduce that:

$$K_{Wee1}[Wee1] = \left(a_{Wee1} + \frac{b_{Wee1} EC50_{Wee1}^{nWee1}}{< Cdk1_a >^{nWee1} + EC50_{Cdc25}^{nCdc25}}\right)\left(\frac{1 - [ATP]}{[ATP]\left(1 - \frac{2[Wee1_0]}{[Wee1_{tot}]}\right) + \frac{[Wee1_0]}{[Wee1_{tot}]}}\right) \qquad Eq.7$$

Then, considering ATP as a substrate for the cyclinB-Cdk1 inactivation reaction, we can deduce the reaction rate ρ_2:

$$\rho_2 = 2[ATP] < Cdk1_a > k^*_{Wee1}[Wee1]$$
$$= 2[ATP] < Cdk1_a > \left(a_{Wee1} + \frac{b_{Wee1} EC50_{Wee1}^{n_{Wee1}}}{< Cdk1_a >^{n_{Wee1}} + EC50_{Wee1}^{n_{Wee1}}}\right)\left(\frac{1 - [ATP]}{[ATP]\left(1 - \frac{2[Wee1_0]}{[Wee1_{tot}]}\right) + \frac{[Wee1_0]}{[Wee1_{tot}]}}\right) \qquad Eq.8$$

When $[ATP_{intial}] = 0.5$, our model with energy dependence switches back to the original model. When deducing the new reaction rate, we need to multiply a coefficient of $\frac{[ATP]}{0.5}$. Similarly, we can deduce the reaction rate for the cyclinB-Cdk1 activation:

$$\rho_3 = < Cdk1_i > k^*_{Cdc25}[Cdc25 - Pi]$$
$$=$$
$$< Cdk1_i > \left(a_{Cdc25} + \frac{b_{Cdc25} < Cdk1_a >^{n_{Cdc25}}}{< Cdk1_a >^{n_{Cdc25}} + EC50_{Cdc25}^{n_{Cdc25}}}\right)\left(\frac{[ATP]}{1 - \frac{[Cdc25 - Pi_0]}{[Cdc25_{tot}]} + \left(2\frac{[Cdc25 - Pi_0]}{[Cdc25_{tot}]} - 1\right)[ATP]}\right) \qquad Eq.9$$

Note that the Wee1 activation form is dephosphorylation form and the Cdc25 activation form is phosphorylation form. Given our new reaction rates for cyclin B-Cdk1 activation and inactivation, we need to obtain the function $\frac{[Wee1_0]}{[Wee1_{tot}]}$ and $\frac{[Cdc25-Pi_0]}{[Cdc25_{tot}]}$, which is, the ratio of activated Wee1 and the ratio of activated Cdc25-Pi in the initial model. According to the previous work[196], and combining the steady state approximation, we have:

$$0 = \frac{d}{dt}[Wee1 - Pi] = \frac{k_e[Cdk1_a]([Wee1_{tot}] - [Wee1 - Pi])}{K_e + [Wee1_{tot}] - [Wee1 - Pi]} - \frac{k_f[PPase]([Wee1 - Pi])}{K_f + [Wee1 - Pi]} \quad Eq.10$$

$$0 = \frac{d}{dt}[Wee1 - Pi] = \frac{k_a[Cdk1_a]([Cdc25_{tot}] - [Cdc25 - Pi])}{K_a + [Cdc25_{tot}] - [Cdc25 - Pi]} - \frac{k_b[PPase]([Cdc25 - Pi])}{K_b + [Cdc25 - Pi]} \quad Eq.11$$

We extracted the explicit expressions of $\frac{[Wee1_0]}{[Wee1_{tot}]}$ and $\frac{[Cdc25-Pi_0]}{[Cdc25_{tot}]}$ as a function of $\frac{[Cdk1_a]}{[CyclinB-Cdk1_{tot}]} = \frac{[Cdk1_a]}{[Cdk1_a]+[Cdk1_i]}$. By substituting these two explicit expressions into Eq.8 and Eq.9, we obtained the final reaction rates including the effect of ATP.

Eq.9 shows that as [ATP] decreases, ρ_2 gets larger, indicating that the activity of [Wee1] increases and it becomes easier for active cyclin B-Cdk1 to be inactivated. In contrast, as more [ATP] is consumed, ρ_3 becomes smaller, meaning that the decreasing activity of [Cdc25-P] and that it gets more difficult for inactive cyclin B-Cdk1 to be activated. Considering all above, we can conclude that as [ATP] decreases, the ratio of double-negative and double-positive feedbacks $R = \frac{k_{Wee1}[Wee1]}{k_{Cdc25}[Cdc25]}$ increases.

We have the updated reaction rates summarized in Table 4.3. Here the $[wee1]_0$ and $[cdc25\text{-}Pi]_0$ represent the steady-state concentration of active Wee1 and Cdc25 when ATP is not considered in reaction. The ratios of the steady-state to total concentrations of Wee1 and Cdc25 can be calculated as a function of active Cdk1 using the parameters of Yang and Ferrell's work[49].

Table 4.3 Reaction rates in the model considering ATP

Reaction	Rate
Active Cdk1 Synthesis	$\rho_1 = k_{sy}$
Active Cdk1 to Inactive Cdk1	$\rho_2 = 2[ATP] < Cdk1_a > \left(a_{Wee1} + \frac{b_{Wee1} EC50_{Wee1}^{n_{Wee1}}}{<Cdk1_a>^{n_{Wee1}} + EC50_{Wee1}^{n_{Wee1}}}\right) \left(\frac{1-[ATP]}{[ATP]\left(1-\frac{2[Wee1_0]}{[Wee1_{tot}]}\right)+\frac{[Wee1_0]}{[Wee1_{tot}]}}\right)$
Inactive Cdk1 to Active Cdk1	$\rho_3 =< Cdk1_i > \left(a_{Cdc25} + \frac{b_{Cdc25} <Cdk1_a>^{n_{Cdc25}}}{<Cdk1_a>^{n_{Cdc25}} + EC50_{Cdc25}^{n_{Cdc25}}}\right) \left(\frac{[ATP]}{1-\frac{[Cdc25-Pi_0]}{[Cdc25_{tot}]}+(2\frac{[Cdc25-Pi_0]}{[Cdc25_{tot}]}-1)[ATP]}\right)$
Active Cdk1 Degradation	$\rho_4 = \left(a_{deg} + \frac{b_{deg} <Cdk1_a>^{n_{deg}}}{<Cdk1_a>^{n_{deg}} + EC50_{deg}^{n_{deg}}}\right) < Cdk1_a >$
Inactive Cdk1 Degradation	$\rho_5 = \left(a_{deg} + \frac{b_{deg} <Cdk1_a>^{n_{deg}}}{<Cdk1_a>^{n_{deg}} + EC50_{deg}^{n_{deg}}}\right) < Cdk1_i >$

4.4 Results and discussion

4.4.1 Simulation modeling

In our proposed model, as oscillation happened, we assumed that if [ATP] decreases, it leads to the increasing of the double-negative and double-positive feedbacks ratio $R = \frac{k_{Wee1}[Wee1]}{k_{Cdc25}[Cdc25]}$, and then results in the climbing baseline and the rising amplitude. Assuming [ATP] linearly decreases, we can simulate the time trace shown in Figure 4.2. ATP-dependent phosphorylation of Cdc25 and Wee1 can decrease R by activating Cdc25 and inhibiting Wee1 simultaneously, resulting in a high dependence of R on the ATP concentration (Figure 4.3).

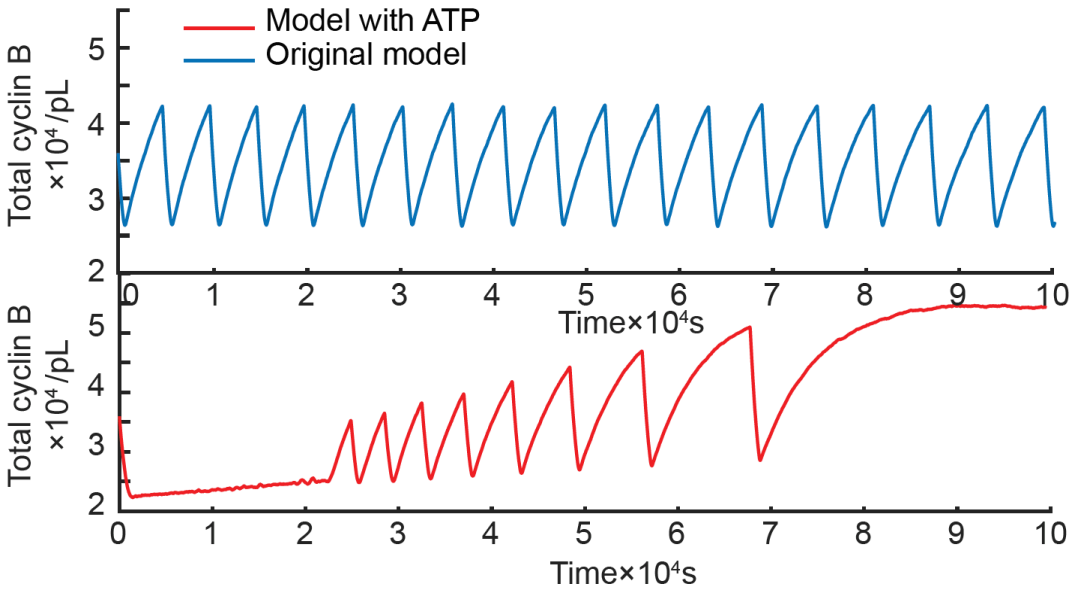

Figure 4.2 Time series of total cyclin B molecules from the model without ATP (top panel, blue line) and with ATP (bottom panel, red line).

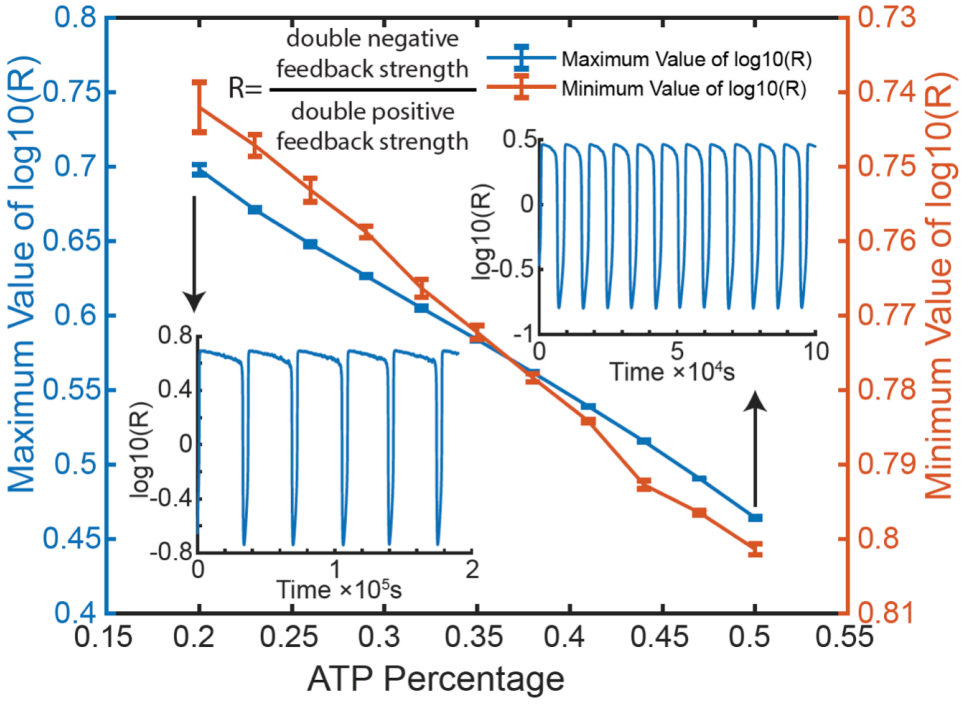

Figure 4.3 Relationship between ATP percentage and R value (ratio of Wee1 activity to Cdc25 activity), showing that decrease of ATP concentration leads to a higher R value. Two inserts represent the dynamics of R value over time when the ATP percentage [ATP]/([ATP]+[ADP]) is set as 0.2 (left) and 0.5 (right).

Using this model, we further investigated the relationship between ATP and the oscillation behaviors. In Figure 4.4, the phase plot of the two-ODE model shows that at a low r (e.g. 0.5), the system stays in a stable steady-state with low cyclin B concentration; and at a high r (e.g. 2.5), the oscillation is arrested in a stable steady-state with high cyclin B concentration. At an intermediate value, increasing R produces oscillations of increasing amplitude, baseline, and period (Figure 4.4 and 4.5). Assuming the available ATP concentration decreases over time, we can reproduce the experimentally observed increment of amplitude, baseline, and period of the cyclin B time courses (Figure 4.5).

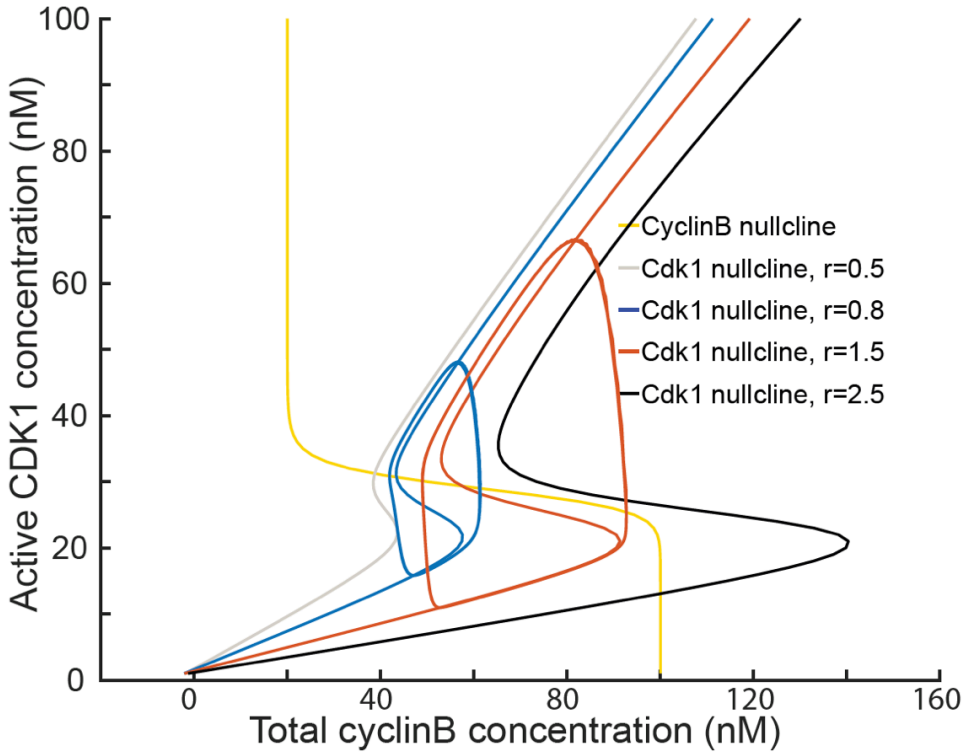

Figure 4.4 Phase plots of the two-ODE model. Parameters for the cyclin B nullcline (yellow) and the Cdk1 nullclines with a variety of values of r were chosen based on previous works[33,161]. Two sample traces of cycle oscillations were plotted for r=0.8 (blue) and r=1.5 (red), showing that a larger r value leads to a higher amplitude and baseline. In addition, r=0.5 (gray) generated a low stable steady-state of cyclin B, while r=2.5 (black) a high stable steady-state of cyclin B. These stable steady-states were indicated by the intersections of the nullclines.

Figure 4.5 shows that when r increases, the baseline, amplitude, and period increase. The reason is that changing the ratio of positive to negative feedback affects the shape of Cdk1 nullcline, and thus affects the crossing points of Cdk1 nullcline and cyclin B nullcline. Our experimental data also shows that the amplitudes and baselines significantly increase, which indicates a rising ratio r over time.

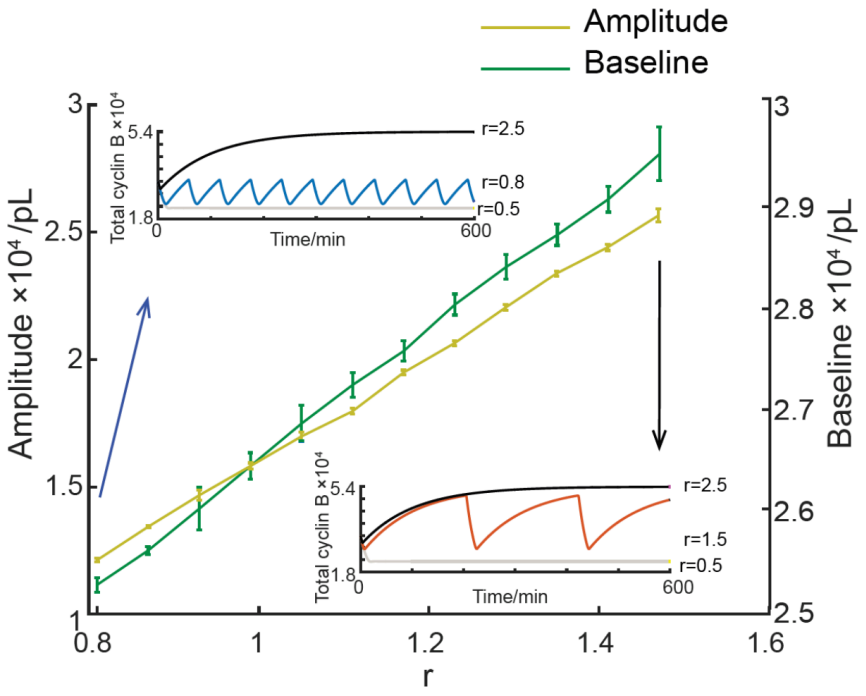

Figure 4.5 Relationship between the oscillation baseline and amplitude values and ATP concentration (positively correlated with r). Error bars indicate the ranges of three replicates. Inserts show two example time courses of total cyclin B with different r values.

The cell cycle period and number of cycles follow the same trend when modulated by cyclin B1 mRNAs, resulting in a lifespan of the oscillatory system sensitive to cyclin B1 mRNA concentration. It suggests that the synthesis rate of cyclin B increases as more cyclin B1 mRNAs are added into our system. Thus, the ATP consumption rate increases. Simulated results of this modified model are shown in Figure 4.6. Assuming ATP consumption rate increases linearly with cyclin B synthesis rate, the number of oscillations and average periods of oscillations decrease as

the synthesis rate of cyclin B increases. This model can also predict the trend that as droplet diameter increases, the average period decreases while the number of oscillations increases (Figure 4.7).

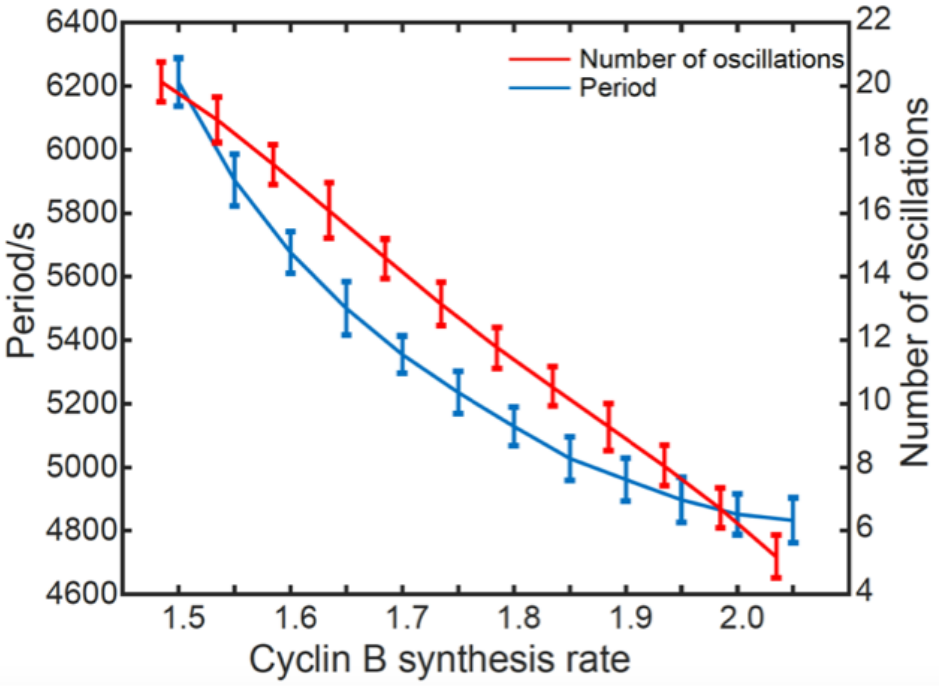

Figure 4.6 The period and number of oscillations decrease with an increasing cyclin B synthesis rate. Error bars indicate the ranges of 50 replicates.

The results in Figure 4.6 and 4.7 show the similar tunability of cell cycle clocks by cyclin B1 mRNAs and droplet radius as in our experimental observations. Both experiments and mathematical modeling suggest that droplets with smaller radii tend to have slower oscillations and fewer number of cycles. Furthermore, increasing the concentration of input cyclin B1 mRNA accelerates oscillations but has fewer number of cycles.

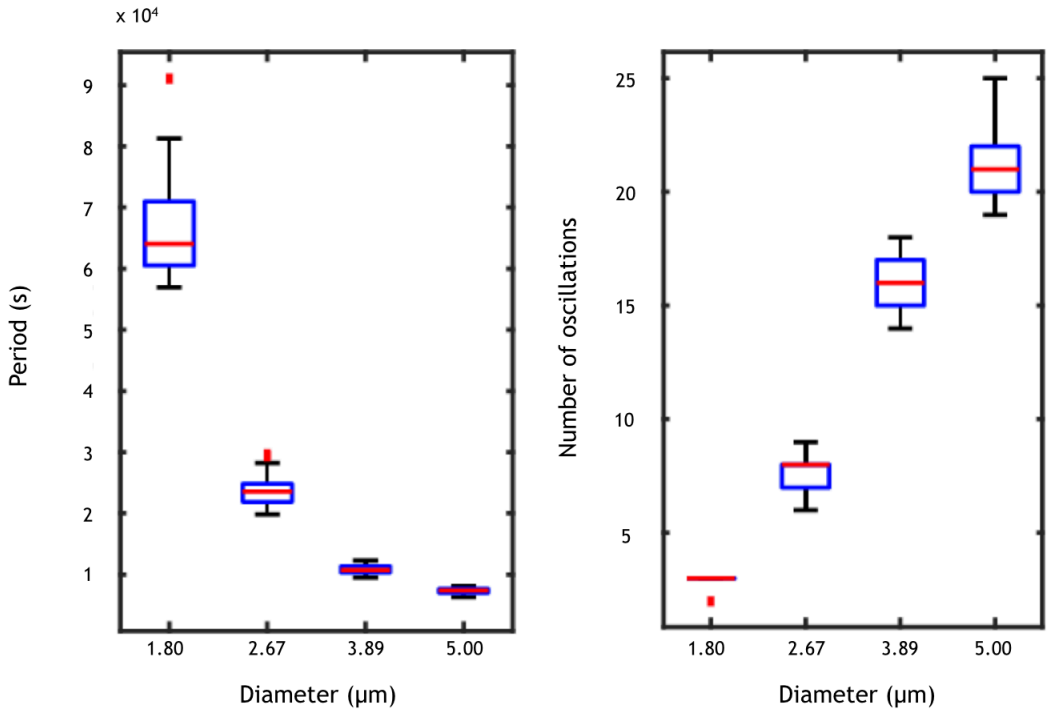

Figure 4.7 Effects of reaction volume on number of oscillations and period, showing that the average number of oscillations increases with droplet diameter while the average oscillation period decreases. The error bars indicate the ranges of 50 replicates.

4.4.2 Future experiments

From the above results and discussion, our proposed energy depletion model indicates that energy plays a key role in the regulation of mitotic oscillations. This is reasonable since energy supply is crucial for reactions in cell-free systems. Unstable energy source may result in short reaction duration. Therefore, energy in our cell-free system is one of the biggest challenges to sustain long-term and undamped mitotic oscillations. For future research study of validating the interesting findings regarding energy dependence of cell cycles from our established stochastic model, it is necessary to introduce an energy regeneration system to our artificial cells.

Mitochondria generate most of the ATP, the source of energy[197] in *Xenopus* eggs and they can be spun down at 10,000 x g for ten minutes. As mentioned in Section 2.2.1.1, *Xenopus* eggs are crushed at the speed of 15,000 x g to obtain cycling cytoplasmic extracts. Thus, most of the mitochondria are removed from our extracts during the preparation step. As a result, the artificial cells generated using our proposed system does not have enough energy supply. For Murray's protocol[38], cycling extracts are supplied with energy mix solution (7.5 mM creatine phosphate, 1mM pH=7.4 ATP, 0.1 mM pH=7.7 EGTA, 1mM $MgCl_2$), which cannot reproduce ATP as an energy supply for mitotic oscillations. As shown in Figure 4.8, creatine kinase catalyzes the conversion of creatine which is a reversible reaction, to produce creatine phosphate and ADP[198]. Creatine phosphate, in the presence of ADP, also creates creatine and ATP. Inspired by these, we can adapt this reaction to the energy mix solution proposed by Murray. In addition to chemicals in the Murray's energy mix solution, 50 μg/mL creatine kinase can be added to create a reaction system, which can generate ATP.

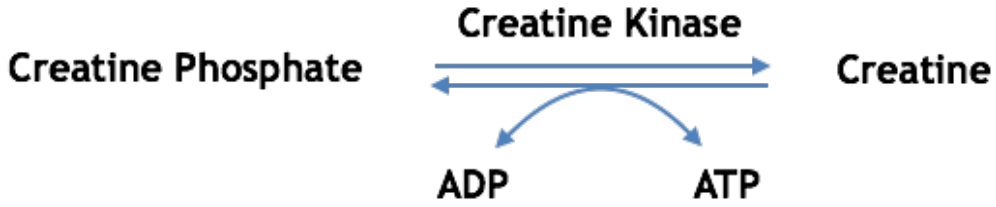

Figure 4.8. Enzyme reaction catalyzed by creatine kinase that convert creatine phosphate to creatine, while generating ATP.

For future research to further investigate how energy regulates cell cycles empirically, we can apply ATP measurement assay to our artificial cell system. Dynamics of mitotic oscillators can be monitored while tuning energy level for the characterization of relationship between cell cycles and energy. The parameters involved in our stochastic model such as the initial energy level

and energy consumption rate can be obtained from experiments. We expect that droplets with higher energy level display faster and more oscillations that last for longer period compared to the droplets with less energy supply. Moreover, it is highly likely that less energy supply accelerates the increase of baseline, amplitude and period.

4.5 Conclusion

Our energy depletion model suggests an interesting mechanism to modulate oscillations with a single control parameter R that depends on the energy-tunable balance of double-negative and double-positive feedback loops. Our modeling results simulated the increasing baseline and amplitude, and increasing oscillation period as shown in our experimental observations. The simulation results also indicate the tunability of cell cycle clocks by tuning radii of droplets and concentration of cyclin B1 mRNA. Similar to the experimental results, increasing the concentration of cyclin B1 mRNAs speeds up oscillations and decreases the number of oscillations. Considering that the rapid, non-stopping cell divisions of an early embryo requires a large amount of energy, this energy-dependent control may function as a “checkpoint” to arrest cell cycles if R becomes too large. For future research study, we can control and monitor the concentration of ATP to validate our findings on the energy depletion model.

Chapter V Conclusion and Outlook

5.1 Conclusion

This dissertation proposed an artificial mitotic oscillation system, which is an *in vitro* system that can create cell-scale micro-emulsions with various sizes containing *Xenopus laevis* egg cytoplasm. These droplet-based cells are stable for days and keep oscillating for dozens of cycles, offering large gains in high-throughput and long-term tracking of dynamical activities in individual droplets. In this system, we successfully reconstituted a series of mitotic events including chromosome condensation, nuclear envelope breakdown and destruction of anaphase substrates such as the securin and cyclin B1 proteins. The oscillation profiles of the system such as period and number of cycles can be reliably regulated by the amount of cyclin B1 mRNAs or droplet sizes. Additionally, we found that energy may be a critical factor for cell cycle behaviors. The knowledge presented in this dissertation demonstrates that this high-throughput single-cell approach is simple and powerful to study complex clock functions.

In Chapter II, we described how to develop the cell-scale artificial cell system and multiple fluorescent reporters. To create a cell-scale mitotic cycle system, we used a simple vortexing method to encapsulate *Xenopus* cytoplasm into micro-droplets with radii ranging from 20 μm to 500 μm. Compared to previous studies, the oscillation activity of cycling extracts is significantly improved by increasing experimental time efficiency of extract preparation and optimizing sample loading method. To test if our *in vitro* mitotic oscillation system is functional or not,

demembranated sperm chromatin, GFP-NLS proteins, and Hoechst 33342 were prepared and applied to the extracts. The results demonstrate that the artificial cells are capable of reconstructing mitotic events and oscillating between interphase and mitosis. To quantitatively characterize cell cycle clock dynamic behaviors, we designed and obtained fluorescent reporters including cyclin B1-YFP and securin-mCherry mRNAs. The fluorescence time courses of these reporters were analyzed and the results show that our system successfully reconstitutes mitotic oscillators of Cdk1 and APC/C, which can drive the periodic mitotic oscillations and a series of downstream events including nuclear envelope breakdown and reformation, and chromosome morphology change.

In Chapter III, we demonstrated that our droplet-based artificial cell system has a potential to study cell cycle clock, especially the tunability of mitotic oscillators. The dynamic behaviors of cell cycle clock were quantitatively measured by fluorescent reporter we discussed in Chapter II. The initial statistical analysis shows that the mitotic oscillators are tunable by varying input cyclin B1 mRNAs and droplet radius. Hypothesis tests were performed to further investigate the tunability of mitotic clock. The results indicate that the behavior of a droplet is highly size dependent if it has a radius smaller than 65 μm, and the smaller droplets tend to have longer oscillation periods, which may be caused by partition noise. When droplet radius is too small, there is a higher probability that the droplet may not encapsulate some essential biological molecules for mitotic oscillations. Therefore, smaller droplets tend to have longer oscillation periods. Moreover, our study suggests that increasing input cyclin B1 mRNA concentration can accelerate oscillations, while adding demembranated sperm chromatin can slow down oscillations. We speculate that higher cyclin B1 mRNA concentration can activate Cdk1 more efficiently, thus the cell cycle oscillators are capable to drive faster periodic progression of multiple mitotic events. Nuclear envelope can reform after adding demembranated sperm chromatin to cycling extracts,

which will consume energy. Therefore, cell cycle is slowed down after applying demembranated sperm chromatin according to the study in Chapter IV.

In Chapter IV, we highlighted the energy dependence of cell cycle clock. The oscillator in our system has an increasing amplitude and period over time, which cannot be explained using existing models. We hypothesized that the oscillations eventually stop likely because of energy depletion. A stochastic two-ODE model concerning the ratio of negative feedback and positive feedback was built to explain our observations of oscillations including increasing baseline, amplitude, and energy consumption rate effect on number of cycles. By modifying current models with energy dependence, the simulation results show similar predictions on dynamic behaviors as experimental observations.

One major limitation for most *in vitro* reconstitutions up to date is that oscillations are generated in well-mixed bulk solutions, which tend to produce quickly damped oscillations. Additionally, these bulk reactions lack the similarity to the actual cell dimensions and the ability of mimicking spatial organization achieved by functional compartmentalization in real cells. These limitations make it impossible to retrieve the cellular heterogeneity to investigate important and challenging questions, such as stochasticity and tunability of an oscillator. Our artificial cell system has overcome these limitations and enables tunable mitotic oscillations, which has a potential for the study of clock functions.

However, the system still has several drawbacks that can be improved in future research. First, the *in vitro* system lacks real-time measurements of ATP, thus we cannot quantify the effect of ATP on the dynamic behavior of cell cycle clock. Therefore, the parameters involved in the model such as initial ATP level, ATP consumption rate, cannot be determined or estimated by experimental measurements. To optimize our model and increase the predictability of oscillator

behaviors, we can develop a new assay to monitor ATP/ADP levels and fit model using experimental data to better forecast cell cycle clock behaviors. For future research, ATP/ADP ratio assay[199,200] can be combined with our artificial cell system to have a better understanding on energy effect. Another limitation is that the concentration of mRNAs in each droplet cannot be detected. The measurement of cell cycle clock activity relies on the fluorescence signal of expressed proteins from securin-mCherry and cyclin B1-YFP mRNAs. This problem can be solved by developing MS2 protein[201] and use it for detection of mRNA, such as cyclin B1 mRNA in artificial cells. The technique has been used to detect appearance of RNAs at the transcription site and observe the changes in RNA number in cytoplasm[202,203]. Finally, one more limitation is that the droplet radius is not uniformly controlled. We used a simple vortexing method to generate droplets with various sizes because we are interested in the study of the size dependence.

For future research on the study of the tunability of cell cycle clock excluding the droplet size effect, it will be more efficient if we use microfluidic device to generate artificial cells with similar sizes because image analysis on sorting droplets by size is less efficient and more complicated. We tested a microfluidic device to study how well it controls droplet size. The top view of the design of the microfluidic device is shown in Figure 5.1A. *Xenopus* cycling extracts was flowed at speed of 1 μL/min and surfactant oil (2% PFPE-PEG) was flowed at speed of 15 μL/min (Figure 5.1B). Surfactant oil and *Xenopus* cycling extracts went through oil inlet and aqueous inlet, respectively. The generated artificial cells were collected from the outlet. The junction width of microfluidic device is 80 μm and thus the diameter of generated droplets is about 80 μm (Figure 5.1C).

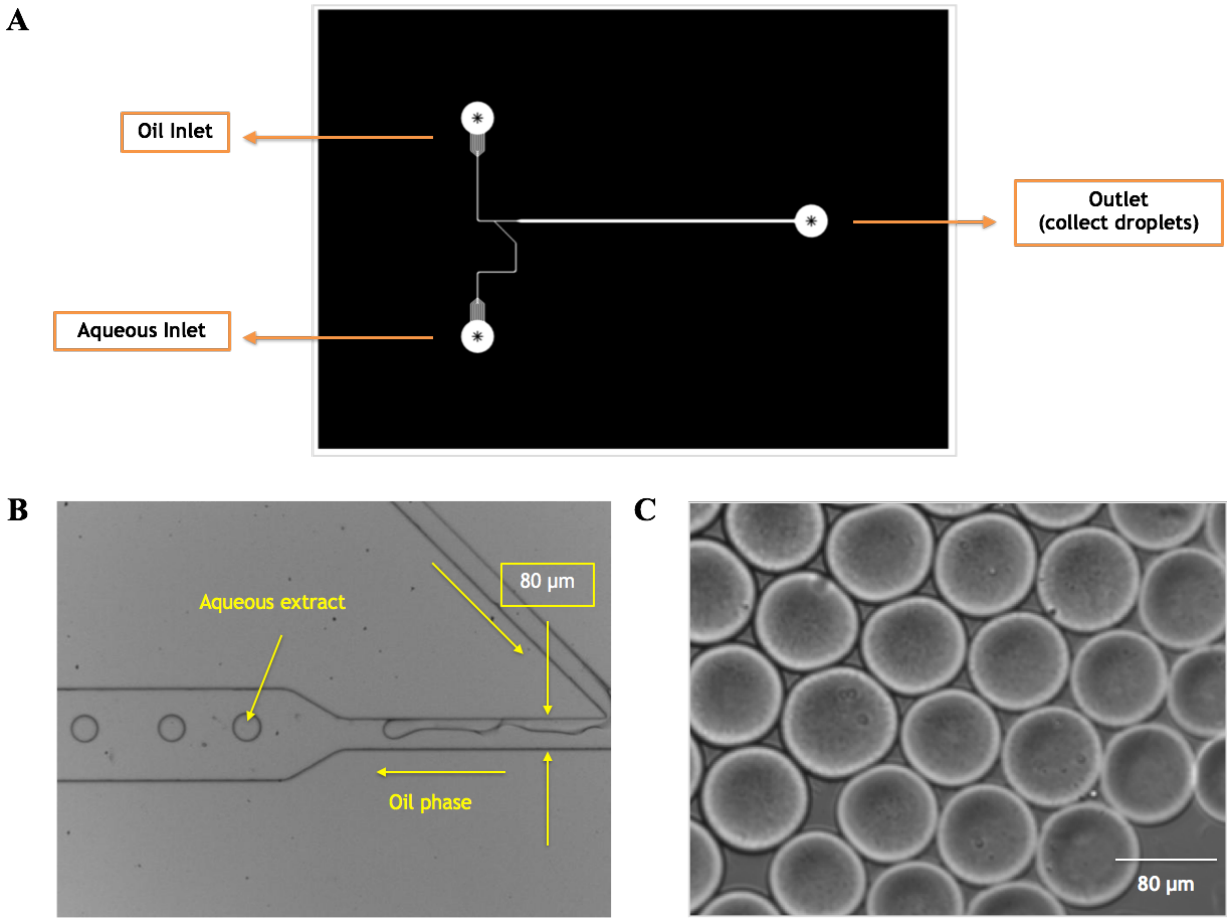

Figure 5.1 A. Top view of the design of microfluidic device B. Cell cycle oscillator components were encapsulated within micro-emulsion droplets. C. Droplets with uniform size were generated.

As shown in Figure 5.1C, we know that microfluidic device can be used for making uniform-sized artificial cells, which help exclude the size effect on cell cycle oscillation behaviors for the study of dynamic events. However, using microfluidic device to generate droplet can take one to two hours, which is not time efficient. Therefore, the first few cycles happening within droplets cannot be detected due to the complicated experimental process of microfluidic chamber. For future research that need to eliminate size effect, the microfluidic device method can be

optimized including preserving extract activity by coating microfluidic chamber and inlet tubing with Teflon, and improving time efficiency.

5.2 Outlook

The research study proposed in this dissertation can be extended further in broader applications. Some ideas for possible future research directions are:

1. In Chapter III, we've demonstrated that our system is a powerful for the study of tunability of cell cycles. Our results indicate that cell cycle is tunable by varying input cyclin B1 mRNA and droplet size. In the future, further investigation on cell cycle functions such as tunability and robustness can be carried out using our artificial cell system. Tunability and robustness are two common properties for many existing biological oscillators such as heartbeats and cell cycles, which are crucial for constructing stable oscillations that are resistant to external noise. Nevertheless, previous studies were carried out through computational studies and there is no reported experimental system to conduct direct manipulations and measurement on tunability and robustness of an oscillator. Using our droplet-based artificial cell system, we can further investigate the tunability and robustness of cell cycle clock. For instance, tunability can be studied by varying the concentrations of key components of mitotic oscillators and artificial cell incubation temperatures. To further understand robustness of cell cycle, we can dissect the double-negative feedback loop of Wee1 by applying Wee1 inhibitors.

2. The temporal relationship between the activation of cyclin B-Cdk1 complex and its nuclear import remains not well understood. It is important to learn when and how the cyclin B-Cdk1 is activated because it is the center of cell cycle oscillators which drives the substantial mitotic events.

The high-throughput artificial cell system proposed in this dissertation can be applied to address this problem. As we discussed in Chapter II, the cell cycle clock activity was quantitatively measured by cyclin B1-YFP and securin-mCherry reporters in our system. These are indirect detection of Cdk1 and APC/C activity, thus we lack the information regarding the time delay between the activation of Cdk1 inactivation and cyclin B protein degradation. Moreover, the localization of cyclin B and Cdk1 are still unknown because we measured the bulk intensity from various reporter. For a further study in understanding the role of cyclin B-Cdk1 kinase, when and how rapidly the complex is activated, the time and spatial information can be provided by integrating our droplet-based artificial cell system with the Förster Resonance Energy Transfer (FRET) sensor for the activity of Cdk1[204], where the donor and acceptor fluorescent proteins are connected by a phosphorylation site that is specific for cyclin B and Cdk1.

3. There is increasing interest in the regulation of cell cycle clocks on spindle assembly procedure. However, there is no effective *in vitro* oscillating platforms to study the dynamics of mitotic spindles. To study whether mitotic spindle assembly procedure is flexible and scalable by tuning frequency of cell cycle clocks, we can encapsulate tubulin protein with rhodamine fluorescence signal to monitor microtubule dynamics in our artificial cells using our cell-like droplet system. To investigate if downstream events can regulate cell cycle clock, we can use laser ablation to cut spindles or apply mechanical force to interrupt the assembly of spindles.

4. Cell sorting and separation become a critical step for biotechnology, cellular biology, and clinical applications. Microfluidics is one of the commonly used techniques to isolate multiple cell types from a mixed biological sample due to its advantages including the ability to process samples

with minor sample volume required, faster reaction time and easy temperature control, etc. By combining our cycling *Xenopus* extract artificial cells with microfluidic chambers to sort and separate cells by size and protein expression level[205,206], this new platform has numerous advantages such as reducing the required amount of sample, and simplifying the complicated manipulations and image analysis commonly associated with cell sorting. Therefore, we can enhance the capability of experimental processing and offer a platform that is easy for simultaneous manipulations of multiple experimental conditions and stochastic analysis.

5. Our system is applicable to construct gene-regulatory networks and study the dynamics of synthetic gene oscillators. Using the high-throughput platform, we can create single artificial cells encapsulated with the designed circuit and our sample loading method should well preserve the oscillating activity. To develop deeper understanding of design principles of synthetic gene oscillators, the oscillators can be tuned by varying levels of inducers, temperature and media source.

5.3 Summary

In summary, the research reported in this dissertation made important contributions in the following two aspects. First, this dissertation proposes a powerful and simple method to reconstitute a cytoplasmic-only biochemical oscillator that contains only essential clock components centering on cyclin B-Cdk1 and its repressor the E3 ubiquitin ligase APC/C. This minimal oscillator, independent of any nuclear components, performs undamped and self-sustained oscillations, significantly better than many existing synthetic oscillators. We designed multiple fluorescent reporters to measure cell cycle clock quantitatively and studied the tunability

of cell cycle clock. This droplet system provides a platform to manipulate artificial cells in a rapid fashion. Second, our system provides an experimental platform to study clock properties of tunability and stochasticity. The generalizable system provides important insights for the future *in vitro* system design for quantitative characterization of clock functions and the study of clock design principles underlying regulatory mechanisms.

Bibliography

1 Elowitz, M. B. & Leibler, S. A synthetic oscillatory network of transcriptional regulators. *Nature* **403**, 335-338.

2 Atkinson, M. R., Savageau, M. A., Myers, J. T. & Ninfa, A. J. Development of genetic circuitry exhibiting toggle switch or oscillatory behavior in Escherichia coli. *Cell* **113**, 597-607.

3 Sprinzak, D. & Elowitz, M. B. Reconstruction of genetic circuits. *Nature* **438**, 443-448.

4 Stricker, J. *et al.* A fast, robust and tunable synthetic gene oscillator. *Nature* **456**, 516-519.

5 Tigges, M., Marquez-Lago, T. T., Stelling, J. & Fussenegger, M. A tunable synthetic mammalian oscillator. *Nature* **457**, 309-312.

6 Danino, T., Mondragon-Palomino, O., Tsimring, L. & Hasty, J. A synchronized quorum of genetic clocks. *Nature* **463**, 326-330.

7 Toettcher, J. E., Mock, C., Batchelor, E., Loewer, A. & Lahav, G. A synthetic-natural hybrid oscillator in human cells. *Proceedings of the National Academy of Sciences of the United States of America* **107**, 17047-17052.

8 Nakajima, M. *et al.* Reconstitution of Circadian Oscillation of Cyanobacterial KaiC Phosphorylation in Vitro. *Science (New York, N.Y.)* **308**, 414.

9 Franco, E. *et al.* Timing molecular motion and production with a synthetic transcriptional clock. *Proceedings of the National Academy of Sciences of the United States of America* **108**, E784-793.

10 Niederholtmeyer, H. *et al.* Rapid cell-free forward engineering of novel genetic ring oscillators. *eLife* **4**, e09771.

11 Semenov, S. N. *et al.* Autocatalytic, bistable, oscillatory networks of biologically relevant organic reactions. *Nature* **537**, 656-660.

12 Rust, M. J., Markson, J. S., Lane, W. S., Fisher, D. S. & O'Shea, E. K. Ordered phosphorylation governs oscillation of a three-protein circadian clock. *Science (New York, N.Y.)* **318**, 809-812.

13 Hasty, J., Dolnik, M., Rottschafer, V. & Collins, J. J. Synthetic gene network for entraining and amplifying cellular oscillations. *Physical review letters* **88**, 148101.

14 Hasty, J., McMillen, D. & Collins, J. J. Engineered gene circuits. *Nature* **420**, 224.

15 Tyson, J. J., Chen, K. C. & Novak, B. Sniffers, buzzers, toggles and blinkers: dynamics of regulatory and signaling pathways in the cell. *Current opinion in cell biology* **15**, 221-231.

16 Endy, D. Foundations for engineering biology. *Nature* **438**, 449.

17 Andrianantoandro, E., Basu, S., Karig, D. K. & Weiss, R. Synthetic biology: new engineering rules for an emerging discipline. *Mol Syst Biol* **2**, 2006.0028.

18 Bray, D. Protein molecules as computational elements in living cells. *Nature* **376**, 307.

19 Stricker, J. *et al.* A fast, robust and tunable synthetic gene oscillator. *Nature* **456**, 516-519.

20 Rosier, B. J. H. M. & de Greef, T. F. A. How to make an oscillator. *eLife* **4**, e12260.

21 van Roekel, H. W. *et al.* Programmable chemical reaction networks: emulating regulatory functions in living cells using a bottom-up approach. *Chemical Society reviews* **44**, 7465-7483.

22 Malumbres, M. & Barbacid, M. Cell cycle, CDKs and cancer: a changing paradigm. *Nature reviews. Cancer* **9**, 153-166.

23 Malumbres, M. & Barbacid, M. To cycle or not to cycle: a critical decision in cancer. *Nature reviews. Cancer* **1**, 222-231.

24 Jackson, S. P. & Bartek, J. The DNA-damage response in human biology and disease. *Nature* **461**, 1071-1078.

25 Jordan, M. A. & Wilson, L. Microtubules as a target for anticancer drugs. *Nature reviews. Cancer* **4**, 253-265.

26 Malumbres, M. & Barbacid, M. Cell cycle kinases in cancer. *Current opinion in genetics & development* **17**, 60-65.

27 Ito, M. Factors controlling cyclin B expression. *Plant molecular biology* **43**, 677-690.

28 Crosby, M. E. Cell Cycle: Principles of Control. *The Yale Journal of Biology and Medicine* **80**, 141-142.

29 Den Haese, G. J., Walworth, N., Carr, A. M. & Gould, K. L. The Wee1 protein kinase regulates T14 phosphorylation of fission yeast Cdc2. *Molecular biology of the cell* **6**, 371-385.

30 Strausfeld, U. *et al.* Dephosphorylation and activation of a p34cdc2/cyclin B complex in vitro by human CDC25 protein. *Nature* **351**, 242-245.

31 Tsai, T. Y. *et al.* Robust, tunable biological oscillations from interlinked positive and negative feedback loops. *Science (New York, N.Y.)* **321**, 126-129.

32 Sha, W. *et al.* Hysteresis drives cell-cycle transitions in Xenopus laevis egg extracts. *Proceedings of the National Academy of Sciences of the United States of America* **100**, 975-980.

33 Pomerening, J. R., Sontag, E. D. & Ferrell, J. E., Jr. Building a cell cycle oscillator: hysteresis and bistability in the activation of Cdc2. *Nature cell biology* **5**, 346-351.

34 Pomerening, J. R., Kim, S. Y. & Ferrell, J. E., Jr. Systems-level dissection of the cell-cycle oscillator: bypassing positive feedback produces damped oscillations. *Cell* **122**, 565-578.

35 Pines, J. Cubism and the cell cycle: the many faces of the APC/C. *Nature reviews. Molecular cell biology* **12**, 427-438.

36 Ferrell, J. E., Jr., Tsai, T. Y. & Yang, Q. Modeling the cell cycle: why do certain circuits oscillate? *Cell* **144**, 874-885.

37 Chang, J. B. & Ferrell, J. E., Jr. Mitotic trigger waves and the spatial coordination of the Xenopus cell cycle. *Nature* **500**, 603-607.

38 Murray, A. W. Cell cycle extracts. *Methods in cell biology* **36**, 581-605.

39 Murray, A. W., Solomon, M. J. & Kirschner, M. W. The role of cyclin synthesis and degradation in the control of maturation promoting factor activity. *Nature* **339**, 280-286.

40 Lohka, M. J. & Maller, J. L. Induction of nuclear envelope breakdown, chromosome condensation, and spindle formation in cell-free extracts. *The Journal of cell biology* **101**, 518-523.

41 Lohka, M. J., Hayes, M. K. & Maller, J. L. Purification of maturation-promoting factor, an intracellular regulator of early mitotic events. *Proc Natl Acad Sci U S A* **85**, 3009-3013.

42 Sudakin, V. *et al.* The cyclosome, a large complex containing cyclin-selective ubiquitin ligase activity, targets cyclins for destruction at the end of mitosis. *Mol Biol Cell* **6**, 185-197.

43 Hannak, E. & Heald, R. Investigating mitotic spindle assembly and function in vitro using Xenopus laevis egg extracts. *Nature protocols* **1**, 2305-2314.

44 Kumagai, A. & Dunphy, W. G. Regulation of the cdc25 protein during the cell cycle in Xenopus extracts. *Cell* **70**, 139-151.

45 Mueller, P. R., Coleman, T. R. & Dunphy, W. G. Cell cycle regulation of a Xenopus Wee1-like kinase. *Mol Biol Cell* **6**, 119-134.

46 Yang, Q. & Ferrell, J. E., Jr. The Cdk1-APC/C cell cycle oscillator circuit functions as a time-delayed, ultrasensitive switch. *Nature cell biology* **15**, 519-525.

47 Trunnell, N. B., Poon, A. C., Kim, S. Y. & Ferrell, J. E., Jr. Ultrasensitivity in the Regulation of Cdc25C by Cdk1. *Molecular cell* **41**, 263-274.

48 Kim, S. Y. & Ferrell, J. E., Jr. Substrate competition as a source of ultrasensitivity in the inactivation of Wee1. *Cell* **128**, 1133-1145.

49 Novak, B. & Tyson, J. J. Numerical analysis of a comprehensive model of M-phase control in Xenopus oocyte extracts and intact embryos. *Journal of cell science* **106 (Pt 4)**, 1153-1168.

50 Thron, C. D. A model for a bistable biochemical trigger of mitosis. *Biophys Chem* **57**, 239-251.

51 Hoffmann, A., Levchenko, A., Scott, M. L. & Baltimore, D. The IkappaB-NF-kappaB signaling module: temporal control and selective gene activation. *Science* **298**, 1241-1245.

52 Cross, F. R. Two redundant oscillatory mechanisms in the yeast cell cycle. *Developmental cell* **4**, 741-752.

53 Lee, K., Loros, J. J. & Dunlap, J. C. Interconnected feedback loops in the Neurospora circadian system. *Science* **289**, 107-110.

54 Swartz, J. Developing cell-free biology for industrial applications. *Journal of industrial microbiology & biotechnology* **33**, 476-485.

55 Anderson, N. G. & Wilbur, K. M. STUDIES ON ISOLATED CELL COMPONENTS : IV. THE EFFECT OF VARIOUS SOLUTIONS ON THE ISOLATED RAT LIVER NUCLEUS. *The Journal of General Physiology* **35**, 781-796.

56 Zemella, A., Thoring, L., Hoffmeister, C. & Kubick, S. Cell-Free Protein Synthesis: Pros and Cons of Prokaryotic and Eukaryotic Systems. *Chembiochem* **16**, 2420-2431.

57 Matthaei, H. & Nirenberg, M. W. The dependence of cell-free protein synthesis in E.coli upon RNA prepared from ribosomes. *Biochemical and Biophysical Research Communications* **4**, 404-408.

58 Braun, P. & LaBaer, J. High throughput protein production for functional proteomics. *Trends in Biotechnology* **21**, 383-388.

59 Spirin, A. S., Baranov, V. I., Ryabova, L. A., Ovodov, S. Y. & Alakhov, Y. B. A continuous cell-free translation system capable of producing polypeptides in high yield. *Science (New York, N.Y.)* **242**, 1162-1164.

60 Carlson, E. D., Gan, R., Hodgman, C. E. & Jewett, M. C. Cell-free protein synthesis: Applications come of age. *Biotechnology Advances* **30**, 1185-1194.

61 Cho, H. *et al.* Optimized clinical performance of growth hormone with an expanded genetic code. *Proceedings of the National Academy of Sciences* **108**, 9060-9065.

62 Londei, P., Altamura, S., Cammarano, P. & Petrucci, L. Differential features of ribosomes and of poly(U)-programmed cell-free systems derived from sulphur-dependent archaebacterial species. *European journal of biochemistry* **157**, 455-462.

63 Elhardt, D. & Böck, A. An in vitro polypeptide synthesizing system from methanogenic bacteria: Sensitivity to antibiotics. *Molecular and General Genetics MGG* **188**, 128-134.

64 Endoh, T. *et al.* Cell-free protein synthesis at high temperatures using the lysate of a hyperthermophile. *Journal of Biotechnology* **126**, 186-195.

65 Kovtun, O. *et al.* Leishmania cell-free protein expression system. *Methods (San Diego, Calif.)* **55**, 58-64.

66 Mureev, S., Kovtun, O., Nguyen, U. T. T. & Alexandrov, K. Species-independent translational leaders facilitate cell-free expression. *Nature Biotechnology* **27**, 747.

67 Spirin, A. S. How Does a Scanning Ribosomal Particle Move along the 5′-Untranslated Region of Eukaryotic mRNA? Brownian Ratchet Model. *Biochemistry* **48**, 10688-10692.

68 LeBowitz, J. H., Smith, H. Q., Rusche, L. & Beverley, S. M. Coupling of poly(A) site selection and trans-splicing in Leishmania. *Genes & development* **7**, 996-1007.

69 Rothblatt, J. A. & Meyer, D. I. Secretion in yeast: Reconstitution of the translocation and glycosylation of α-factor and invertase in a homologous cell-free system. *Cell* **44**, 619-628.

70 Hodgman, C. E. & Jewett, M. C. Optimized extract preparation methods and reaction conditions for improved yeast cell-free protein synthesis. *Biotechnology and bioengineering* **110**, 2643-2654.

71 Choudhury, A., Hodgman, C. E., Anderson, M. J. & Jewett, M. C. Evaluating fermentation effects on cell growth and crude extract metabolic activity for improved yeast cell-free protein synthesis. *Biochemical Engineering Journal* **91**, 140-148.

72 Hodgman, C. E. & Jewett, M. C. Characterizing IGR IRES-mediated translation initiation for use in yeast cell-free protein synthesis. *New Biotechnology* **31**, 499-505.

73 Ullah, M. W., Khattak, W. A., Ul-Islam, M., Khan, S. & Park, J. K. Bio-ethanol production through simultaneous saccharification and fermentation using an encapsulated reconstituted cell-free enzyme system. *Biochemical Engineering Journal* **91**, 110-119.

74 Sawasaki, T., Ogasawara, T., Morishita, R. & Endo, Y. A cell-free protein synthesis system for high-throughput proteomics. *Proceedings of the National Academy of Sciences of the United States of America* **99**, 14652-14657.

75 Harbers, M. Wheat germ systems for cell-free protein expression. *FEBS letters* **588**, 2762-2773.

76 Madin, K., Sawasaki, T., Ogasawara, T. & Endo, Y. A highly efficient and robust cell-free protein synthesis system prepared from wheat embryos: plants apparently contain a suicide system directed at ribosomes. *Proceedings of the National Academy of Sciences of the United States of America* **97**, 559-564.

77 Stech, M. *et al.* Production of functional antibody fragments in a vesicle-based eukaryotic cell-free translation system. *Journal of Biotechnology* **164**, 220-231.

78 Quast, R. B. *et al.* Automated production of functional membrane proteins using eukaryotic cell-free translation systems. *Journal of Biotechnology* **203**, 45-53.

79 Shaklee, P. M. *et al.* Protein incorporation in giant lipid vesicles under physiological conditions. *Chembiochem* **11**, 175-179.

80 Kornbluth, S., Yang, J. & Powers, M. Analysis of the cell cycle using Xenopus egg extracts. *Current protocols in cell biology* **Chapter 11**, Unit 11.11.

81 Good, M. C., Vahey, M. D., Skandarajah, A., Fletcher, D. A. & Heald, R. Cytoplasmic volume modulates spindle size during embryogenesis. *Science (New York, N.Y.)* **342**, 856-860.

82 Lorca, T. *et al.* Fizzy is required for activation of the APC/cyclosome in Xenopus egg extracts. *The EMBO Journal* **17**, 3565-3575.

83 Brödel, A. K., Raymond, J. A., Duman, J. G., Bier, F. F. & Kubick, S. Functional evaluation of candidate ice structuring proteins using cell-free expression systems. *Journal of Biotechnology* **163**, 301-310.

84 Zhu, J. Mammalian cell protein expression for biopharmaceutical production. *Biotechnology Advances* **30**, 1158-1170.

85 Anastasina, M., Terenin, I., Butcher, S. J. & Kainov, D. E. A technique to increase protein yield in a rabbit reticulocyte lysate translation system. *BioTechniques* **56**, 36-39.

86 Endo, Y. & Sawasaki, T. Cell-free expression systems for eukaryotic protein production. *Current opinion in biotechnology* **17**, 373-380.

87 Saul, J. *et al.* Development of a full-length human protein production pipeline. *Protein Science* **23**, 1123-1135.

88 Roberts, R. W. & Szostak, J. W. RNA-peptide fusions for the in vitro selection of peptides and proteins. *Proceedings of the National Academy of Sciences of the United States of America* **94**, 12297-12302.

89 Qiu, J. & LaBaer, J. Nucleic acid programmable protein array a just-in-time multiplexed protein expression and purification platform. *Methods in enzymology* **500**, 151-163.

90 He, M., He, Y., Luo, Q. & Wang, M. From DNA to protein: No living cells required. *Process Biochemistry* **46**, 615-620.

91 Tsai, T. Y. C., Theriot, J. A. & Ferrell, J. E., Jr. Changes in Oscillatory Dynamics in the Cell Cycle of Early <italic>Xenopus laevis</italic> Embryos. *PLoS Biol* **12**, e1001788.

92 Theurkauf, W. E. & Hawley, R. S. Meiotic spindle assembly in Drosophila females: behavior of nonexchange chromosomes and the effects of mutations in the nod kinesin-like protein. *The Journal of cell biology* **116**, 1167-1180.

93 Telley, I. A., Gaspar, I., Ephrussi, A. & Surrey, T. Aster migration determines the length scale of nuclear separation in the Drosophila syncytial embryo. *The Journal of cell biology* **197**, 887-895.

94 Telley, I. A., Gaspar, I., Ephrussi, A. & Surrey, T. A single Drosophila embryo extract for the study of mitosis ex vivo. *Nature protocols* **8**, 310-324.

95 Pfeiffer, B. D. *et al.* Refinement of tools for targeted gene expression in Drosophila. *Genetics* **186**, 735-755.

96 Yang, Q. & Ferrell, J. E. The Cdk1–APC/C cell cycle oscillator circuit functions as a time-delayed, ultrasensitive switch. *Nat Cell Biol* **15**, 519-525.

97 Chang, J. B. & Ferrell Jr, J. E. Mitotic trigger waves and the spatial coordination of the Xenopus cell cycle. *Nature* **500**, 603-607.

98 Cahu, J. *et al.* Phosphorylation by Cdk1 Increases the Binding of Eg5 to Microtubules In Vitro and in Xenopus Egg Extract Spindles. *PLoS ONE* **3**, e3936.

99 Good, M. C., Vahey, M. D., Skandarajah, A., Fletcher, D. A. & Heald, R. Cytoplasmic Volume Modulates Spindle Size During Embryogenesis. *Science (New York, N.Y.)* **342**, 856-860.

100 Liu, J., Grimison, B. & Maller, J. L. New insight into metaphase arrest by cytostatic factor: from establishment to release. *Oncogene* **26**, 1286-1289.

101 Suri, S. *et al.* Microfluidic-based patterning of embryonic stem cells for in vitro development studies. *Lab Chip* **13**, 4617-4624.

102 Saeidnia, S., Manayi, A. & Abdollahi, M. From in vitro Experiments to in vivo and Clinical Studies; Pros and Cons. *Current drug discovery technologies* **12**, 218-224.

103 Stratton, C. W. In vitro susceptibility testing versus in vivo effectiveness. *The Medical clinics of North America* **90**, 1077-1088.

104 Kieserman, E. K., Lee, C., Gray, R. S., Park, T. J. & Wallingford, J. B. High-magnification in vivo imaging of Xenopus embryos for cell and developmental biology. *Cold Spring Harb Protoc* **2010**, pdb.prot5427.

105 Toh, Y.-C., Blagovic, K., Yu, H. & Voldman, J. Spatially organized in vitro models instruct asymmetric stem cell differentiation. *Integrative Biology* **3**, 1179-1187.

106 Bratt-Leal, A. M., Kepple, K. L., Carpenedo, R. L., Cooke, M. T. & McDevitt, T. C. Magnetic manipulation and spatial patterning of multi-cellular stem cell aggregates. *Integrative Biology* **3**, 1224-1232.

107 Murray, A. W. & Kirschner, M. W. Cyclin synthesis drives the early embryonic cell cycle. *Nature* **339**, 275-280.

108 Hutchison, C. J., Cox, R. & Ford, C. C. The control of DNA replication in a cell-free extract that recapitulates a basic cell cycle in vitro. *Development* **103**, 553-566.

109 Blow, J. J. & Laskey, R. A. Initiation of DNA replication in nuclei and purified DNA by a cell-free extract of Xenopus eggs. *Cell* **47**, 577-587.

110 Hutchison, C. J., Cox, R., Drepaul, R. S., Gomperts, M. & Ford, C. C. Periodic DNA synthesis in cell-free extracts of Xenopus eggs. *The EMBO Journal* **6**, 2003-2010.

111 Belmont, L. D., Hyman, A. A., Sawin, K. E. & Mitchison, T. J. Real-time visualization of cell cycle-dependent changes in microtubule dynamics in cytoplasmic extracts. *Cell* **62**, 579-589.

112 Verde, F., Labbé, J.-C., Dorée, M. & Karsenti, E. Regulation of microtubule dynamics by cdc2 protein kinase in cell-free extracts of Xenopus eggs. *Nature* **343**, 233.

113 Tuomikoski, T., Felix, M. A., Doree, M. & Gruenberg, J. Inhibition of endocytic vesicle fusion in vitro by the cell-cycle control protein kinase cdc2. *Nature* **342**, 942-945.

114 Murray, A. W. & Kirschner, M. W. Cyclin synthesis drives the early embryonic cell cycle. *Nature* **339**, 275-280.

115 Torbensen, K., Rossi, F., Ristori, S. & Abou-Hassan, A. Chemical communication and dynamics of droplet emulsions in networks of Belousov-Zhabotinsky micro-oscillators produced by microfluidics. *Lab on a Chip* **17**, 1179-1189.

116 Shang, L., Cheng, Y. & Zhao, Y. Emerging Droplet Microfluidics. *Chemical Reviews* **117**, 7964-8040.

117 Weitz, M. *et al.* Diversity in the dynamical behaviour of a compartmentalized programmable biochemical oscillator. *Nat Chem* **6**, 295-302.

118 Baccouche, A. *et al.* Massively parallel and multiparameter titration of biochemical assays with droplet microfluidics. *Nat. Protocols* **12**, 1912-1932.

119 Gulati, S. *et al.* Opportunities for microfluidic technologies in synthetic biology. *Journal of The Royal Society Interface*.

120 Dressler, O. J., Casadevall i Solvas, X. & deMello, A. J. Chemical and Biological Dynamics Using Droplet-Based Microfluidics. *Annual Review of Analytical Chemistry* **10**, 1-24.

121 Marx, V. Cell biology: tracking a cell's cycle. *Nature Methods* **14**, 233.

122 Matsu-Ura, T. *et al.* Intercellular Coupling of the Cell Cycle and Circadian Clock in Adult Stem Cell Culture. *Molecular cell* **64**, 900-912.

123 Hazel, J. *et al.* Changes in cytoplasmic volume are sufficient to drive spindle scaling. *Science (New York, N.Y.)* **342**, 853-856.

124 Takinoue, M. & Takeuchi, S. Droplet microfluidics for the study of artificial cells. *Analytical and bioanalytical chemistry* **400**, 1705-1716.

125 Kintses, B., van Vliet, L. D., Devenish, S. R. & Hollfelder, F. Microfluidic droplets: new integrated workflows for biological experiments. *Current opinion in chemical biology* **14**, 548-555.

126 Gillespie, P. J. & Blow, J. J. Nucleoplasmin-mediated chromatin remodelling is required for Xenopus sperm nuclei to become licensed for DNA replication. *Nucleic Acids Research* **28**, 472-480.

127 Gillespie, P. J., Gambus, A. & Blow, J. J. Preparation and use of Xenopus egg extracts to study DNA replication and chromatin associated proteins. *Methods (San Diego, Calif.)* **57**, 203-213.

128 Debbasch, C., Pisella, P. J., Rat, P., Warnet, J. M. & Baudouin, C. [Antioxidant effects of mast cell inhibitors in a human conjunctival cell line]. *Journal francais d'ophtalmologie* **24**, 121-128.

129 Smolewski, P., Bedner, E., Gorczyca, W. & Darzynkiewicz, Z. "Liquidless" cell staining by dye diffusion from gels and analysis by laser scanning cytometry: potential application at microgravity conditions in space. *Cytometry* **44**, 355-360.

130 Purschke, M., Rubio, N., Held, K. D. & Redmond, R. W. Phototoxicity of Hoechst 33342 in time-lapse fluorescence microscopy. *Photochemical & photobiological sciences : Official journal of the European Photochemistry Association and the European Society for Photobiology* **9**, 1634-1639.

131 Gilbert, D. F. *et al.* A novel multiplex cell viability assay for high-throughput RNAi screening. *PLoS One* **6**, e28338.

132 Zhang, X. & Kiechle, F. Hoechst 33342-induced apoptosis is associated with decreased immunoreactive topoisomerase I and topoisomerase I-DNA complex formation. *Annals of clinical and laboratory science* **31**, 187-198.

133 Sivakumar, S. & Gorbsky, G. J. Spatiotemporal regulation of the anaphase-promoting complex in mitosis. *Nature Reviews Molecular Cell Biology* **16**, 82.

134 Izawa, D. & Pines, J. How APC/C–Cdc20 changes its substrate specificity in mitosis. *Nature cell biology* **13**, 223.

135 Lu, D. *et al.* Multiple mechanisms determine the order of APC/C substrate degradation in mitosis. *The Journal of Cell Biology* **207**, 23-39.

136 Gibson, D. G. *et al.* Enzymatic assembly of DNA molecules up to several hundred kilobases. *Nat Meth* **6**, 343-345.

137 Kok, S. d. *et al.* Rapid and Reliable DNA Assembly via Ligase Cycling Reaction. *ACS Synthetic Biology* **3**, 97-106.

138 Wang, J. W. *et al.* CRISPR/Cas9 nuclease cleavage combined with Gibson assembly for seamless cloning. *BioTechniques* **58**, 161-170.

139 Blawid, R. & Nagata, T. Construction of an infectious clone of a plant RNA virus in a binary vector using one-step Gibson Assembly. *Journal of virological methods* **222**, 11-15.

140 Garibyan, L. & Avashia, N. Research Techniques Made Simple: Polymerase Chain Reaction (PCR). *The Journal of investigative dermatology* **133**, e6-e6.

141 Hecker, K. H. & Roux, K. H. High and low annealing temperatures increase both specificity and yield in touchdown and stepdown PCR. *BioTechniques* **20**, 478-485.

142 Froger, A. & Hall, J. E. Transformation of Plasmid DNA into E. coli Using the Heat Shock Method. *Journal of Visualized Experiments : JoVE*, 253.

143 Sive, H. L., Grainger, R. M. & Harland, R. M. Isolating Xenopus laevis Testes. *Cold Spring Harbor Protocols* **2007**, pdb.prot4735.

144 Showell, C. & Conlon, F. L. Egg Collection and In Vitro Fertilization of the Western Clawed Frog Xenopus tropicalis. *Cold Spring Harbor protocols* **2009**, pdb.prot5293-pdb.prot5293.

145 Lohka, M. J. & Masui, Y. Formation in vitro of sperm pronuclei and mitotic chromosomes induced by amphibian ooplasmic components. *Science (New York, N.Y.)* **220**, 719-721.

146 Seibel, N. M., Eljouni, J., Nalaskowski, M. M. & Hampe, W. Nuclear localization of enhanced green fluorescent protein homomultimers. *Analytical biochemistry* **368**, 95-99.

147 Hodel, A. E. *et al.* Nuclear localization signal receptor affinity correlates with in vivo localization in Saccharomyces cerevisiae. *The Journal of biological chemistry* **281**, 23545-23556.

148 Stallings, C. L. & Silverstein, S. Dissection of a Novel Nuclear Localization Signal in Open Reading Frame 29 of Varicella-Zoster Virus. *Journal of Virology* **79**, 13070-13081.

149 Hodel, M. R., Corbett, A. H. & Hodel, A. E. Dissection of a Nuclear Localization Signal. *Journal of Biological Chemistry* **276**, 1317-1325.

150 Fanara, P., Hodel, M. R., Corbett, A. H. & Hodel, A. E. Quantitative Analysis of Nuclear Localization Signal (NLS)-Importin α Interaction through Fluorescence Depolarization: EVIDENCE FOR AUTO-INHIBITORY REGULATION OF NLS BINDING. *Journal of Biological Chemistry* **275**, 21218-21223.

151 Ariotti, N. *et al.* Modular Detection of GFP-Labeled Proteins for Rapid Screening by Electron Microscopy in Cells and Organisms. *Developmental cell* **35**, 513-525.

152 Martin, R. M., Leonhardt, H. & Cardoso, M. C. DNA labeling in living cells. *Cytometry. Part A : the journal of the International Society for Analytical Cytology* **67**, 45-52.

153 Chazotte, B. Labeling nuclear DNA using DAPI. *Cold Spring Harb Protoc* **2011**, pdb.prot5556.

154 Smith, P. J. *et al.* Kinetic analysis of intracellular Hoechst 33342--DNA interactions by flow cytometry: misinterpretation of side population status? *Cytometry. Part A : the journal of the International Society for Analytical Cytology* **83**, 161-169.

155 Dabauvalle, M. C. & Scheer, U. Assembly of nuclear pore complexes in Xenopus egg extract. *Biology of the cell / under the auspices of the European Cell Biology Organization* **72**, 25-29.

156 VanWormer, A. M., Lindquist, R. & Sendelbach, S. E. The effects of acupuncture on cardiac arrhythmias: A literature review. *Heart & Lung: The Journal of Acute and Critical Care* **37**, 425-431.

157 Rahimi Azghadi, M., Iannella, N., Al-Sarawi, S. & Abbott, D. Tunable low energy, compact and high performance neuromorphic circuit for spike-based synaptic plasticity. *PloS one* **9**, e88326.

158 Drion, G., O'Leary, T. & Marder, E. Ion channel degeneracy enables robust and tunable neuronal firing rates. *Proceedings of the National Academy of Sciences* **112**, E5361-E5370.

159 Tsai, T. Y.-C. *et al.* Robust, Tunable Biological Oscillations from Interlinked Positive and Negative Feedback Loops. *Science (New York, N.Y.)* **321**, 126.

160 Bieler, J. *et al.* Robust synchronization of coupled circadian and cell cycle oscillators in single mammalian cells. *Molecular Systems Biology* **10**.

161 Sha, W. *et al.* Hysteresis drives cell-cycle transitions in Xenopus laevis egg extracts. *Proceedings of the National Academy of Sciences* **100**, 975-980.

162 Box, J. F. Guinness, Gosset, Fisher, and Small Samples. *Statist. Sci.* **2**, 45-52.

163 Chen, Z. *et al.* Researching for better instructional methods using AB experiments in MOOCs: results and challenges. *Research and Practice in Technology Enhanced Learning* **11**, 9.

164 Banerjee, A., Chitnis, U. B., Jadhav, S. L., Bhawalkar, J. S. & Chaudhury, S. Hypothesis testing, type I and type II errors. *Industrial Psychiatry Journal* **18**, 127-131.

165 Greenland, S. *et al.* Statistical tests, P values, confidence intervals, and power: a guide to misinterpretations. *European Journal of Epidemiology* **31**, 337-350.

166 Silva-Ayçaguer, L. C., Suárez-Gil, P. & Fernández-Somoano, A. The null hypothesis significance test in health sciences research (1995-2006): statistical analysis and interpretation. *BMC Medical Research Methodology* **10**, 44.

167 Biau, D. J., Jolles, B. M. & Porcher, R. P Value and the Theory of Hypothesis Testing: An Explanation for New Researchers. *Clinical Orthopaedics and Related Research* **468**, 885-892.

168 Farrugia, P., Petrisor, B. A., Farrokhyar, F. & Bhandari, M. Research questions, hypotheses and objectives. *Canadian Journal of Surgery* **53**, 278-281.

169 Whitley, E. & Ball, J. Statistics review 3: Hypothesis testing and P values. *Critical Care* **6**, 222-225.

170 Dorey, F. In Brief: The P Value: What Is It and What Does It Tell You? *Clinical Orthopaedics and Related Research* **468**, 2297-2298.

171 Bailey, T. L. & Gribskov, M. Combining evidence using p-values: application to sequence homology searches. *Bioinformatics (Oxford, England)* **14**, 48-54.

172 Zou, K. H., Tuncali, K. & Silverman, S. G. Correlation and simple linear regression. *Radiology* **227**, 617-622.

173 Tripepi, G., Jager, K. J., Dekker, F. W. & Zoccali, C. Linear and logistic regression analysis. *Kidney international* **73**, 806-810.

174 Chang, D., Xu, N. & Q Luo, K. *Chang DC, Xu N, Luo KQ.. Degradation of cyclin B is required for the onset of anaphase in Mammalian cells. J Biol Chem 278: 37865-37873*. Vol. 278 (2003).

175 Thornton, B. R. & Toczyski, D. P. Securin and B-cyclin/CDK are the only essential targets of the APC. *Nature cell biology* **5**, 1090-1094.

176 B Arnold, T. & W Emerson, J. *Nonparametric Goodness-of-Fit Tests for Discrete Null Distributions*. Vol. 3 (2011).

177 Yap, B. W. & Sim, C. H. Comparisons of various types of normality tests. *Journal of Statistical Computation and Simulation* **81**, 2141-2155.

178 Mohd Razali, N. & Yap, B. *Power Comparisons of Shapiro-Wilk, Kolmogorov-Smirnov, Lilliefors and Anderson-Darling Tests*. Vol. 2 (2011).

179 Nahm, F. S. Nonparametric statistical tests for the continuous data: the basic concept and the practical use. *Korean Journal of Anesthesiology* **69**, 8-14.

180 Vargha, A. & Delaney, H. *The Kruskal-Wallis Test and Stochastic Homogeneity*. Vol. 23 (1998).

181 Goldbeter, A. A minimal cascade model for the mitotic oscillator involving cyclin and cdc2 kinase. *Proceedings of the National Academy of Sciences of the United States of America* **88**, 9107-9111.

182 Tyson, J. J. Modeling the cell division cycle: cdc2 and cyclin interactions. *Proceedings of the National Academy of Sciences of the United States of America* **88**, 7328-7332.

183 Novak, B. & Tyson, J. J. Modeling the Cell-Division Cycle - M-Phase Trigger, Oscillations, and Size Control. *Journal of theoretical biology* **165**, 101-134.

184 Ciliberto, A., Novak, B. & Tyson, J. J. Mathematical model of the morphogenesis checkpoint in budding yeast. *The Journal of cell biology* **163**, 1243-1254.

185 Zinser, E. R. *et al.* Choreography of the transcriptome, photophysiology, and cell cycle of a minimal photoautotroph, prochlorococcus. *PloS one* **4**, e5135.

186 Ortmann, B., Druker, J. & Rocha, S. Cell cycle progression in response to oxygen levels. *Cellular and molecular life sciences : CMLS* **71**, 3569-3582.

187 Bi, M. *et al.* ER stress-regulated translation increases tolerance to extreme hypoxia and promotes tumor growth. *The EMBO journal* **24**, 3470-3481.

188 Liu, L. *et al.* Hypoxia-induced energy stress regulates mRNA translation and cell growth. *Molecular cell* **21**, 521-531.

189 Moniz, S., Biddlestone, J. & Rocha, S. Grow(2): the HIF system, energy homeostasis and the cell cycle. *Histology and histopathology* **29**, 589-600.

190 Tuck, C., Zhang, T., Potapova, T., Malumbres, M. & Novak, B. Robust mitotic entry is ensured by a latching switch. *Biology open* **2**, 924-931.

191 Tsai, T. Y., Theriot, J. A. & Ferrell, J. E., Jr. Changes in oscillatory dynamics in the cell cycle of early Xenopus laevis embryos. *PLoS Biol* **12**, e1001788.

192 Kampen, N. G. v. *Stochastic processes in physics and chemistry*. Rev. and enl. edn, (North-Holland, 1992).

193 Gillespie, D. T. Exact Stochastic Simulation of Coupled Chemical-Reactions. *Journal of Physical Chemistry* **81**, 2340-2361.

194 Hochegger, H. *et al.* New B-type cyclin synthesis is required between meiosis I and II during Xenopus oocyte maturation. *Development* **128**, 3795.

195 Kobayashi, H., Stewart, E., Poon, R. Y. & Hunt, T. Cyclin A and cyclin B dissociate from p34cdc2 with half-times of 4 and 15 h, respectively, regardless of the phase of the cell cycle. *The Journal of biological chemistry* **269**, 29153-29160.

196 Novak, B. & Tyson, J. J. Numerical analysis of a comprehensive model of M-phase control in Xenopus oocyte extracts and intact embryos. *Journal of cell science* **106 (Pt 4)**, 1153-1168.

197 Henze, K. & Martin, W. Essence of mitochondria. *Nature* **426**, 127.

198 Wallimann, T. & Hemmer, W. Creatine kinase in non-muscle tissues and cells. *Molecular and cellular biochemistry* **133-134**, 193-220.

199 Xue, M., Wei, W., Su, Y., Johnson, D. & Heath, J. R. Supramolecular Probes for Assessing Glutamine Uptake Enable Semi-Quantitative Metabolic Models in Single Cells. *Journal of the American Chemical Society* **138**, 3085-3093.

200 Julien, S. G. *et al.* Narciclasine attenuates diet-induced obesity by promoting oxidative metabolism in skeletal muscle. *PLoS Biol* **15**, e1002597.

201 Bertrand, E. *et al.* Localization of ASH1 mRNA Particles in Living Yeast. *Molecular cell* **2**, 437-445.

202 Golding, I., Paulsson, J., Zawilski, S. M. & Cox, E. C. Real-Time Kinetics of Gene Activity in Individual Bacteria. *Cell* **123**, 1025-1036.

203 Chubb, J. R., Trcek, T., Shenoy, S. M. & Singer, R. H. Transcriptional Pulsing of a Developmental Gene. *Current Biology* **16**, 1018-1025.

204 Gavet, O. & Pines, J. Progressive activation of CyclinB1-Cdk1 coordinates entry to mitosis. *Developmental cell* **18**, 533-543.

205 Voldman, J. Electrical forces for microscale cell manipulation. *Annual review of biomedical engineering* **8**, 425-454.

206 Shields, C. W., Reyes, C. D. & López, G. P. Microfluidic Cell Sorting: A Review of the Advances in the Separation of Cells from Debulking to Rare Cell Isolation. *Lab Chip* **15**, 1230-1249.